Doctoral Dissertation
博士論文

Non-equilibrium dynamics of periodically driven active colloids

（周期的に駆動されるアクティブコロイドの非平衡ダイナミクス）

A Dissertation Submitted
for the Degree of Doctor of Philosophy
December 2019

令和 1 年 12 月 博士（理学）申請

Department of Physics, Graduate School of Science,
The University of Tokyo

東京大学大学院 理学系研究科物理学専攻

Airi N. Kato

中本（加藤）愛理

Ph.D. Dissertation

Non-equilibrium dynamics of periodically driven active colloids

Airi N. Kato

Department of Physics, Graduate School of Science,
The University of Tokyo

Abstract

In this dissertation, nonequilibrium dynamics of periodically driven self-propelled colloids was studied experimentally and numerically. In the last two decades, studies on self-propelled particles have been intensively conducted including numerical simulations and experiments of collective motion as a nonequilibrium physics. Many studies dealt with self-propelled particles moving unidirectionally by constant propulsion forces. In contrast, time-dependent propulsions and various ways of self-propulsions such as apolar, reciprocating, run-and-tumble, and helical motions have been experimentally realised. Especially in these cases, not only the collective dynamics but the single-particle dynamics has been of interest. In this study, reciprocating motions were focused on. For example, *Myxococcus xanthus* are known to reciprocate in nature. Self-propelling droplets reciprocate spontaneously at their natural frequencies. In these systems, the frequency and phase of the reciprocation cannot be controlled. In the systems driven by global external fields, the time-dependent propulsions were mostly on-off signals. To investigate sinusoidally driven self-propelled particles which are expected to reciprocate, Quincke rollers, which are dielectric particles driven by electrorotation induced in conducting liquid, were selected and studied experimentally with an AC field.

First, the single-particle dynamics of a Quincke roller under an AC field was investigated. The periodicity in the velocity at the frequency of the external field below the Maxwell-Wagner frequency was confirmed. Then, the reciprocation of the particle was numerically explained by a generalisation of the theory on the Quincke roller under the DC field to that under the AC field. It was found that the peak at the external frequency and its odd higher harmonic peaks appeared in the velocity power spectrum both experimentally and numerically. The periodic motion was confirmed to be a limit cycle in a wide range of frequency values. Also, the existence of peaks at frequency lower than the external frequency and anomalous MSD behaviour were discovered experimentally, which were considered to be due to a DC component of the velocity.

Secondly, the locomotion of a doublet and a triplet which appeared spontaneously as a part of dynamic clustering in the AC experiment was studied. Not only the periodicities in the velocities at the frequency of the external field and the odd higher harmonics but also even harmonics were found, which is considered to be a result of the dipolar-dipolar interaction. Furthermore, periodic changes of configuration within typical interparticle distances were observed in the doublet and the triplet. Also, heterogeneity of the mean propulsion angle around a particle was revealed. This research can be an experimental example of periodic self-propelled particles and highlight characteristics of multi-particle dynamics made of a small number of interacting particles.

Acknowledgement

I would like to express my deepest appreciation to Prof. Masaki Sano and Prof. Kazumasa A. Takeuchi, who are my previous and current supervisors. I could meet the world of Active matter and start the experiment thanks to Prof. Sano. I was inspired by his suggestions from his broad perspectives and also helped by his patience. Prof. Takeuchi took much time to discuss with me, which greatly helped me to finalise my thesis. I was affected by his passionate attitude to understand phenomena deeper and precisely. During I has been in both lab, it is my pleasure that I frequently had the chances to take many seminars around various topics by the lab members and various visitors, and the opportunity to discuss my research with them.

I owe Dr. Daiki Nishiguchi a lot who was an ex-member of Sano lab and is the assistant professor of Takeuchi lab who taught me to fabricate the Quincke cell and give me many useful suggestions. I also learn a lot from his master and Ph.D. thesis. I feel gratitude towards Prof. Tetsuya Hiraiwa who was the assistant professor who advised and encouraged me. I thank all the present and former lab members for their advice and helps.

I would like to express my gratitude to Prof. Hirofumi Wada for accepting me to stay in his lab and discuss a lot. Also, I would like to offer my thanks to Prof. Hiroyuki Kitahata who gave me the chance to do a seminar in his lab and gave many suggestions from his theoretical background. I also appreciate the fruitful discussions with Prof. Fernando Peruani, Prof. Kazue Kudo, Prof. Natsuhiko Yoshinaga respectively.

Last but not least, I sincerely thank my family for supporting and believing me.

Contents

Chapter 1

General introduction

1.1 Active matter physics

In nature, there are plenty of motile objects, such as animals, bacteria, cars and so on. They move by consuming "food" or their internal energy. In the last two decades, physicists have been fascinated and studied such a nonequilibrium system which is so called "active matter". We call such moving particles as "self-propelled particles" (SPPs).

Let us briefly explain what are the self-propelled particles. First, the moving directions are not determined by only the directions of external fields. Their propelling direction are typically determined by their internal degrees of freedom such as their polarity or shape. Secondly, they need to consume some kinds of energy to convert their motilities. Thus, it is remarkable that the examples in the following are **not** SPPs. Objects rolling on an inclined plane from the horizon, which just move homogeneously, are not SPPs. Another example of non-SPPs is charged particles by electrophoresis. The situation that all particles just moves to the parallel/antiparallel direction of the external field is not usually considered as SPPs. However, SPPs are not necessarily living. Some kinds of SPPs are driven by consuming a chemical energy or external energy sources which will be explained in the next chapter.

Why we study active matter? Active matter is one of the fields of nonequilibrium physics. As is well known, equilibrium thermodynamics and statistical mechanics succeed in describing equilibrium systems which is called "passive particles" in contradistinction to active particles. Then, some of nonequilibrium systems have been studied and understood somewhat such as the perturbation from equilibrium, nonequilibrium steady states, and fluctuation in small systems. Unlike the nonequilibrium steady states like heat or electric conductions, self-propelled particles are driven not by the boundary but the bulk. Thus, self-propelled particles are nonequilibrium systems, which should be studied as a new kind of nonequilibrium states.

To seek universalities in active matter, many efforts have been intensively conducted theoretically, numerically and experimentally. One of the main topics on SPPs is collective properties such as phase transitions and order or pattern formations as we can see in flocks of birds, schools of fish, lanes of humans in a crowded passage, and so on.

Inspired from the nature, the coarse-grained models for interacting SPPs were intro-

duced. For example, there is the Vicsek model [1]:

$$\theta_j(t+1) = \arg \sum_{x_{kj}<R} e^{\mathrm{i}\theta_k(t)} + \eta_j(t) \tag{1.1}$$

$$\boldsymbol{x}_j(t+1) = \boldsymbol{x}_j(t) + v_0 \hat{\boldsymbol{n}}_{\theta_j(t+1)}, \tag{1.2}$$

where $\theta_j(t)$, $\boldsymbol{x}_j(t)$ represent the propulsion angle and the position of the j-th particle at time t. The unit vector $\hat{\boldsymbol{n}}_{\theta_j(t+1)}$ means the direction as $\hat{\boldsymbol{n}}_{\theta_j(t+1)} = (\cos\theta_j(t+1), \sin\theta_j(t+1))$. $\eta_j(t)$ is a white noise uniformly distributed on $[-\eta/2, +\eta/2]$ ($\eta > 0$). The interaction is represented by the first term of Eq. (1.1), which gives the average direction of the particles at the smaller interparticle distances than R between particle j and k. This model gives ordered phase when the number density is large or the noise is small, and the disorder-order transition is first-order as confirmed by Grégoire *et al.* [2]. The model did not only bear the phase transition but also predict the existence of Giant Number Fluctuation (GNF) which is $\Delta N \propto \langle N \rangle^{\alpha}$ ($\alpha > 0.5$), while equilibrium systems and random systems give $\alpha = 0.5$ because of the central limit theorem. It was supported by the continuum theory on active matter which is called the Toner-Tu theory [3].

The Vicsek-like models such as active nematics [4, 5] and self-propelled rods [6] were also established. In active nematics, a particle moves to apolar directions, that is, forward or backward at the probability of 1/2 with changing the axis' direction by noise. The interaction of the model is nematic, which ignores π-rotation symmetry in two-dimensional plane. This gives a nematic order phase. Another Vicsek-like model, self-propelled rod moves one direction of the longer axis and interact nematically [6].

Experimentally, the polar order was realised by vibrated bipolar disks [7], Quincke rollers [8], the actomyosin motility assay [9] and so on, though these were inhomogeneous. The nematic order was realised by elongated bacteria [10] experimentally. Not only the order formations but pattern formations such as vortex formations [11–13] and dynamic clustering [14] in experiments was reported and modelled. Also, mesoscale turbulent structures which are also one of the topics on SPPs were realised [15, 16].

These experimental SPPs used above are presented in the next chapter.

Diffusion properties Not only the collective properties, diffusion properties of single particle is one of the interests in active matter. In equilibrium, a brownian particle fluctuates and displaces with the mean square displacement (MSD)

$$\mathrm{MSD}(\tau; t) := \langle (\boldsymbol{x}(t+\tau) - \boldsymbol{x}(t))^2 \rangle = 4D\tau, \tag{1.3}$$

in two-dimensional case. Here $\boldsymbol{x}(t)$ represents the position of a particle at time t. As is well known, it is diffusive ($\mathrm{MSD}(\tau)$ is proportional to τ) except for the extremely short time interval $\tau_M = m/\gamma \sim \mu$s, where m and γ are the mass of the pariticle and the damping coefficient. The more precise MSD follows [17, 18]

$$\mathrm{MSD}(\tau) = 4D\tau + \frac{4k_{\mathrm{B}}T}{m}\tau_M^2(e^{-\tau/\tau_M} - 1), \tag{1.4}$$

where k_{B} and T are the Boltzmann constant and temperature. In equilibrium, the (translational) diffusion coefficient D is

$$D = \frac{k_{\mathrm{B}}T}{6\pi a\eta}, \tag{1.5}$$

which is determined by the fluctuation dissipation theorem. Here a and η are the radius of the particle and the viscosity of the fluid.

In contrast, an active brownian particle which is propelled with constant speed v_0 and displaced by a white gaussian translational noise (expressed by a translational diffusion coefficient D) and a white gaussian rotational noise (expressed by a rotational diffusion coefficient D_θ) [18, 19] yields

$$\mathrm{MSD}(\tau) = 4D\tau + \frac{2v_0^2}{D_\theta^2}(e^{-D_\theta\tau} - 1 + D_\theta\tau). \tag{1.6}$$

In the very short-time range $\tau \ll 1/D_\theta$, it is diffusive due to the translational diffusion. In intermediate time scales, it is ballistic ($\mathrm{MSD}(\tau) \propto \tau^2$) while it is diffusive in the long-time range $\tau \geq 1/D_\theta$. This diffusion property: "diffusive $\rightarrow$ ballistic $\rightarrow$ diffusive" is typical in many models of active brownian particles [18, 19], because many models assumed constant unidirectional propulsion with noises. In fact, the typical behaviour was experimentally confirmed, though the diffusion coefficients were dependent on parameters such as propulsion speeds [19, 20].

However, the diffusion property was changed if the way of single-particle self-propulsion were changed like apolar or reciprocating, run-and-tumble and helical. Großmann *et al.* considered a model of reciprocating self-propulsion with a probabilistic directional reversal [21]. To model the motion of bacteria *Myxococcus xanthus* which reverse their direction probabilistically, they used a clock model that the reversal occurs after M-times occurrence of Poissonian events. Fig. 1.1 shows the MSD of their model. If $M = 1$, which means that the directional reversal happens simply by a Poisson process, it gives the typical diffusion properties of active brownian particles like the above as depicted in Fig. 1.1. No oscillatory behaviour appeared in the MSD. In contrast, in the cases of large M, the reciprocating feature appears in the MSD. Although they do not mention directly, the plot of $M = 100$ in Fig. 1.1 shows that the exponent of $\mathrm{MSD}(\tau) \propto \tau^\beta$ becomes both larger than 2 (superballistic) and less than 0 according to the time length. However, the oscillatory behaviour of MSD has not been measured in *Myxococcus xanthus* [21] as they remarked that this oscillation can be overlooked when the time resolution was not fine enough.

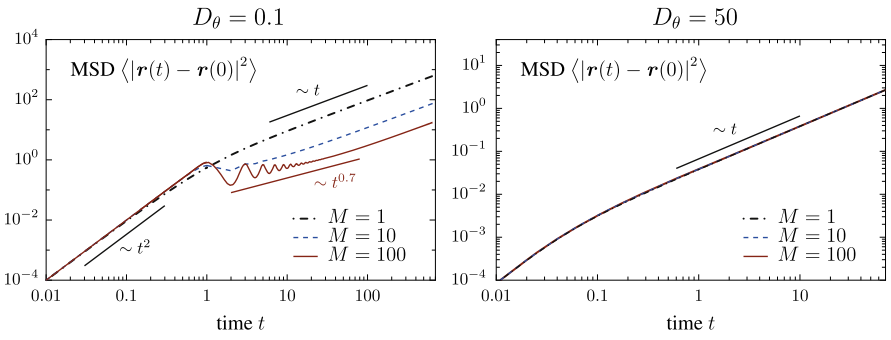

Figure 1.1: MSD of the probabilistic reciprocating model by Großmann *et al.* [21] (The mean frequency of the Poisson process was set to 1.)

In another model by Babel *et al.* [22], they considered several kinds of time-dependent self-propulsion particles with rotational and translational noises. They also did not men-

tion the exponent β of MSD(τ)$\propto \tau^{\beta}$ explicitly, but the exponent oscillated in the sinusoidal self-propulsion case and includes the time scales which are superballistic.

In this way, changing of the ways of single-particle self-propulsion alters their diffusion properties greatly, which means that MSD is worth calculating for an unknown behaviour of SPPs.

1.2 Experimental realisation of self-propelled particles

In this section, various experimental systems of SPPs are introduced which include systems using biological materials and non-biological systems. Let us focus on two points of view. The first one is the ways of self-propulsion. Many of the SPPs in the following move persistently in their polarity direction with constant propulsions, though the actual velocities were varied by translational/rotational diffusion-like noises and their interactions. Some of the SPPs below propel in apolar or reciprocating, run-and-tumble and helical ways, in which case their single-particle properties were also of interests.

The second point of view is diffusion property. Not all the experiments measured the diffusion properties of the single particle especially for polar motions with constant speeds, which gives the typical diffusion properties of Eq. (1.6).

1.3 Biological self-propelled particles

Let us start from the most intuitive one: living things whose propelling mechanisms are mechanical motions consuming their energy. One example is the fish which were confined in a shallow water tank to observe two-dimensional motions of the SPPs [12]. However, the majority of biological SPPs experimentally used were not the m-size objects but μm-size objects such as bacteria and cells for many reasons such as the easiness of preparing macroscopic systems and controllability.

Bacteria *Bacillus subtilis* [13,15,23] and *E. coli* [10,24,25] have been often used in many researches on SPPs. By choosing strains and appropriate processes, the single bacterium move in polar direction with a constant speed and with a noise. For example, Fig. 1.2 shows trajectories of *E. coli* which did run-and-tumble motion (left) and polar motion (right). The run-and-tumble motion means that a single body moves straight for a time interval and then reorientates suddenly, which appears in wild type *E. coli*. Another example is elongated *E. coli* which do not tumble and move with a constant speed made nematic order phase which was realised by Nishiguchi *et al.* [10].

Moreover, there are the bacteria *Myxococcus xanthus* which reciprocate by changing of their gliding directions as a single-cell level with a certain waiting time distribution [26].

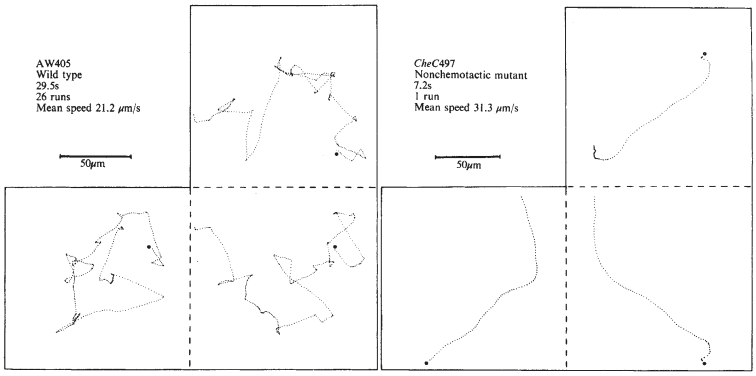

Figure 1.2: Run-and-tumble motion and polar motion [24] (These were three-dimensionally captured, and the projections were shown.)

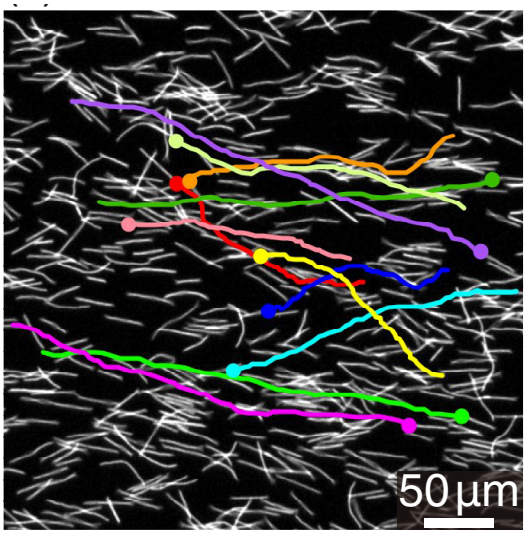

Figure 1.3: Nematic order of elongated bacteria [10]

Motility assay Another type of biological SPPs are motility assay. Motility assay is originally a technique to investigate the motility of single molecular motor. By attaching molecular motors to a substrate, it is regarded that filaments move on the substrate as shown in (a) of Fig. 1.4. Schaller *et al.* used the assay system with kinesin motors and actin filaments [9], which realised the polar density wave by the single motion straight and the local alignment interaction as presented in (b) of Fig. 1.4. Sumino *et al.* used the assay system with dynein motors and microtubules [11], which realised the vortex lattice formation by the single motion with constant speed and a typical finite curvature and the local alignment interaction as shown in Fig. 1.5. In these experiments, the speed of self-propulsion can be controlled by the density of motors in certain ranges.

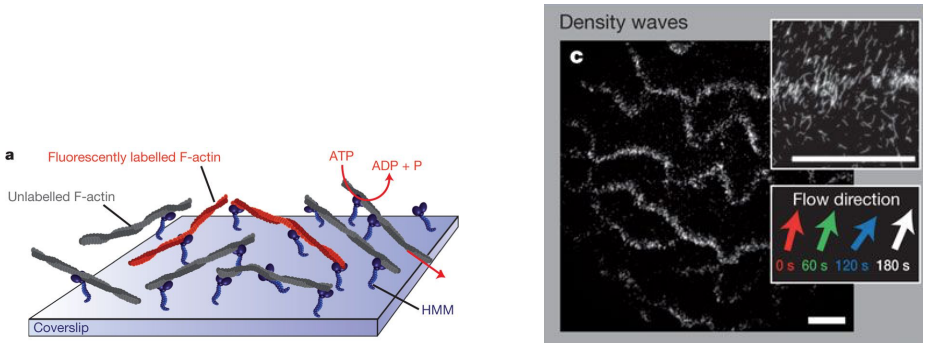

(a) Schematic of a motility assay system

(b) Density wave of polar filaments in high density

Figure 1.4: Self-propelling polar filaments in the motility assay system [9]

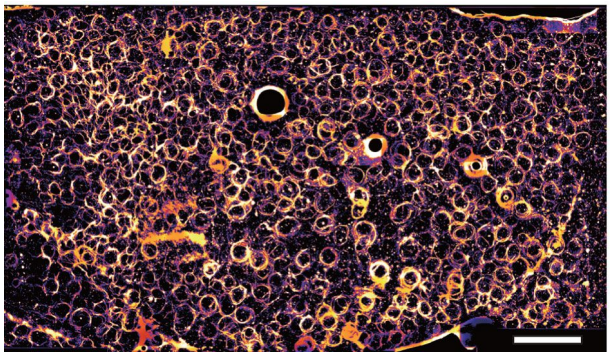

Figure 1.5: Vortex lattice formation by polar filaments moving with constant a speed and a typical finite curvature [11]

1.4 Artificial self-propelled particles

Let us move on the experimental realisations of artificial SPPs. Generally, the propulsion mechanisms of artificial SPPs are not obvious except for robots which have motors and batteries inside, so particles need to be given energy externally to propel.

Shaken disks, rods and droplets One of the most intuitive artificial SPPs is the object driven by vibration such as the polar disk [7] in Fig. 1.6. The disks on a plate are vibrated vertically so that they propel their polar direction which are inherent to the individuals. Note that the directions of propulsions are not relevant to the external global force.

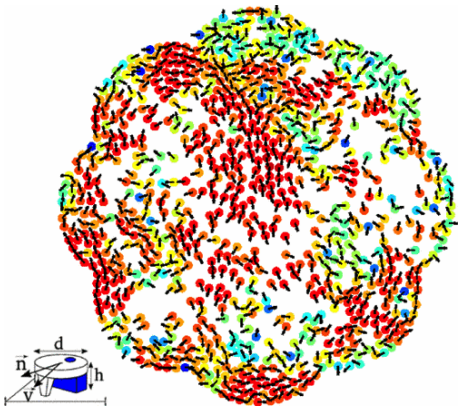

Figure 1.6: Polar disk propelling one direction (left below) and its collective motion [7].

Rods on a plate vibrating are also SPPs, but the motion is apolar: The particle moves forward or backward with changing the axis' direction by noise, which was realised by Narayan *et al.* [27]. It was modelled by active nematics [4, 5] which was mentioned in Section 1.1.

Another type of SPPs by vibrations is the swimming droplet floating on a liquid bath and driven by a surface wave of the bath [28]. Various kinds of motions such as zig-zag, reciprocation and irregular polygonal turning motion in Fig. 1.7 were observed by changing the acceleration and frequency.

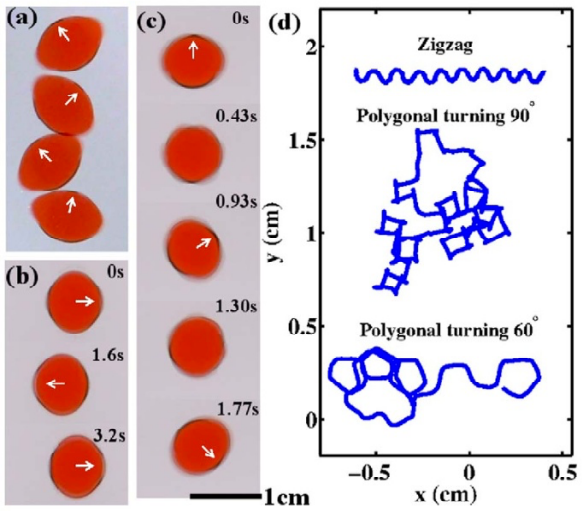

Figure 1.7: Zig-zag, reciprocation and irregular polygonal turning motion of the swimming droplet [28]

Janus particles The Janus particles hold asymmetries in the physical property of the single particle. The energy sources of Janus particles are various such as chemical compounds [14, 29–32], light (heat) [33–37] and electric field [16]. Let us see them one by one in the following.

The bimetallic Au − Pt nanorod immersed in H_2O_2 propels to the Pt side due to the osmotic pressure accompanying with the local chemical gradient around the particle which is caused by the asymmetric chemical reaction as depicted in (a) of Fig. 1.8.

The Janus particle with the asymmetry in the heat conductivities is driven by the diffusion's asymmetry around the individual particle by a homogeneous light exposure [33, 34, 37]. An example of the particle is shown in (b) of Fig. 1.8.

The Janus particle with the asymmetry in the permittivities is driven by the asymmetric flow induced by the electric field [16, 38] as shown in (c) of Fig. 1.8. The flow is called the induced charge electro osmotic flow.

In the Janus particles above, the external field or energy source are given globally. The propulsion direction is determined *a priori* by the polarity of the particle which is not relevant to the direction of the external field. For example, in the case of (c) of Fig. 1.8, the propulsion direction is perpendicular to the electric field applied, which is totally different from electrophoresis. This enables us to consider the Janus particles as SPPs.

The diffusion properties of the Janus particles with polar motions in the above were the typical one: "ballistic to diffusive" [19, 20].

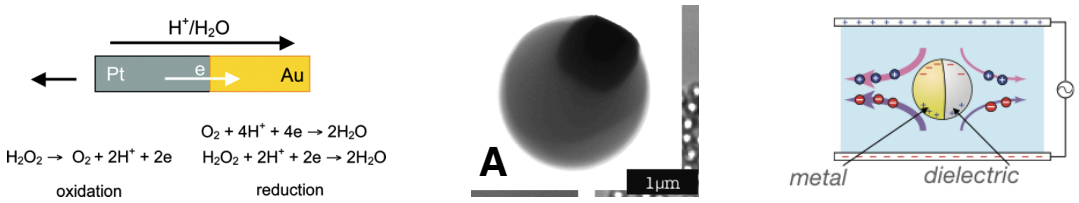

(a) Chemical energy driven particle [30]

(b) Light (heat) driven particle [34]

(c) Electric field driven particle [16](The figure was provided by Dr. Nishiguchi.)

Figure 1.8: Examples of Janus particles

The run-and-tumble motion like *E. coli* were also realised using Janus particles [36, 39]. Lozano *et al.* used time-dependent light energy input of on/off-sequences so that a particle "tumble" by thermal rotation diffusion [36], in which they obtained oscillatory MSDs. Mano *et al.* used chirally coated Janus particles which were rotated by an electric field deterministically, which is similar to tumbling [39].

Marangoni droplets Droplets with the asymmetry of its surface tension are known to move in/on fluid by the Marangoni flow [40], which have been intensively investigated. In some experiments like [41–44], droplets propelled to their polar direction, back-and-forth, or circularly, which were spontaneously occurred. Also, helical motions were reported using liquid crystal droplets [45, 46].

Quincke rollers The Quincke rollers [8, 47–49] are dielectric colloids rolling on a lower electrode by electrorotation due to the Quincke effect under a DC electric field as shown in Fig. 1.9. The individual particle moves straight with constant speed and with a rotational noise. All particles move perpendicular to the electric fields. The speed is controlled by the magnitude of the applied electric field. Though the typical velocity is large $\sim$ 1mm/s, the inertia of particles can be neglected (See Appendix B). In this thesis, the Quincke rollers were used and investigated, so detail mechanism and explanation are done in Chapter 2.

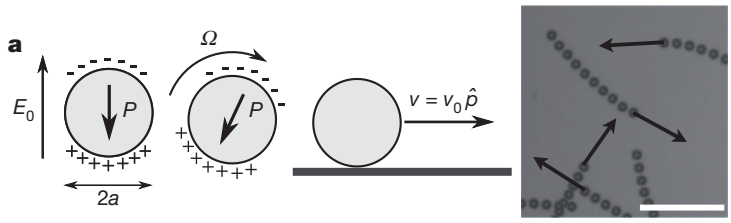

Figure 1.9: Quincke roller under a DC field [8]

By changing the simple DC field to a DC square pulse sequence in (a) of Fig. 1.10, not only a straight motion (shown in the most right figure of (b) of Fig. 1.10) but run-and-tumble motion (shown in the most left figure of (b) of Fig. 1.10) was realised [50]. Here is the memory time τ_{MW} of the particle's polarisation which determines the propulsion direction. When a DC field applied, the steady polarisation is made in the time τ_{MW}. Thus, if the rest time τ_T with no field is larger than the memory time τ_{MW}, the propelling direction is not conserved, which realise a run-and-tumble motion. In contrast, the direction is conserved when the rest is small enough. In the left two in (b) of Fig. 1.10, the diffusive property is typical: "ballistic to diffusive", which was also theoretically supported.

By changing the distribution of the rest times τ_T from an exponential to power-law, they produced run-and-tumble motion and then Lévy walk as shown in Fig. 1.11. The figure shows that the run-and-tumble particle shows typical diffusive property: "ballistic to diffusive". In contrast, the Lévy-walk particle shows superdiffusive in the long-time range, which was also supported in theory.

In this section, various experimental realisation of SPPs are explained, which includes not only the straight motion but various motions such as apolar, reciprocating, helical, run-and-tumble motion, and so on. Also, theoretical models exist which give a reciprocating motion [51] and a circular/helical motion [52–54] by active deformation of the particle. In this way, Not only collective motions but even single-particle motions are of interests and have been investigated.

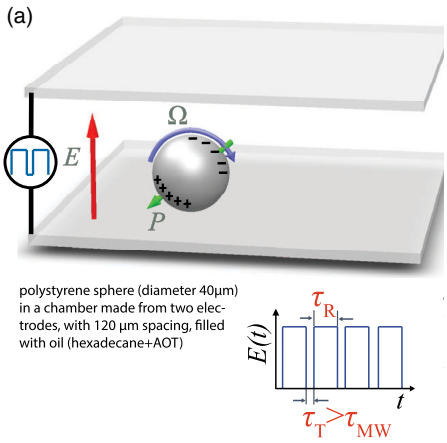

(a) Setup and the DC square pulse sequence

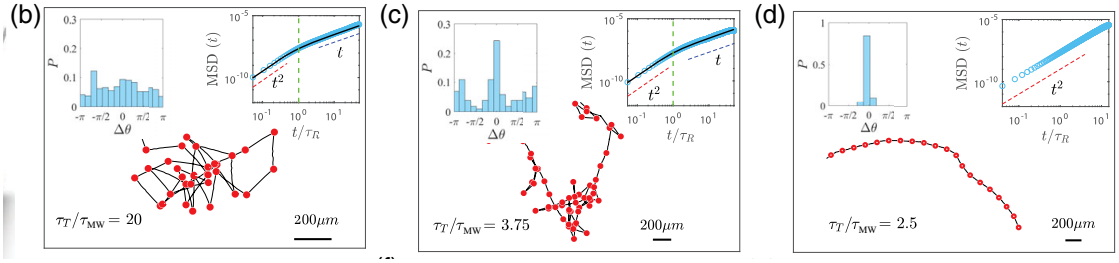

(b) Single-particle motions depending on the rest time τ_T and the memory time τ_{MW}

Figure 1.10: The Quincke rollers driven by the DC pulse sequence [50]

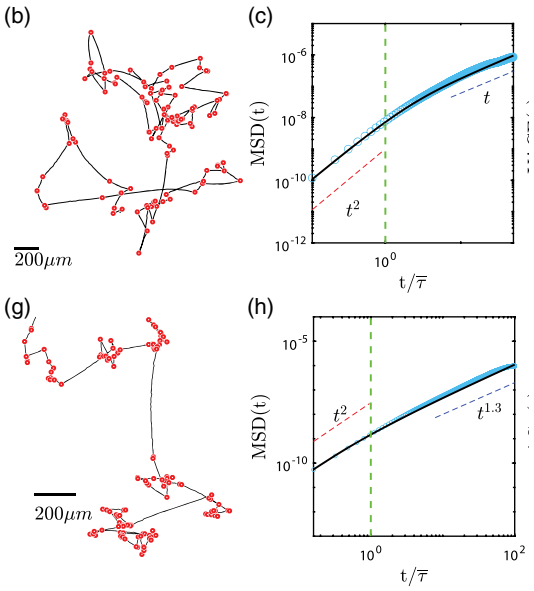

Figure 1.11: Run-and-tumble (top) and Lévy walk (bottom) realised by a Quincke roller [50]

1.5 Motivation

Many experimental systems reviewed in the above section such as non-tumbling bacteria [10,13,15,23], motility assay systems [9,11], vibrated polar disks [7], swimming droplets by a surface wave [28], Janus particles [14, 16, 29–35], Marangoni droplets [41, 42, 44] mainly dealt with the polar motions with constant speeds and with noises. In the case, the speeds were controlled in some range by globally changing parameters.

In contrast, various ways of self-propulsion such as apolar, reciprocating, helical, run-and-tumble motion have been realised experimentally as mentioned in the previous section. Some of them have the time-dependent properties except noises in nature (e.g. tumbling *E. coli* [24], reciprocating *Myxococcus xanthus* [26]), and others express the properties spontaneously (e.g. Swimming droplets by a surface wave [28], Marangoni droplets [40–42, 44–46]). The rests of them were realised by applying time-dependent external fields such as the on/off switching of a light [36] and an electric field [39, 50]. These time-dependent propulsive systems produced run-and-tumble motions and or a Lévy walk. Here the question that how the system of SPPs with reciprocating motions by a time-dependent global external field is realised arises. The above on/off switching did not give a reversal of the propulsion direction. Although Janus particles can reverse the propelling direction without a physical rotation in a high frequency region for an electric field driven system [38, 55] or in a high intensity region for a light driven system [33, 35], switchings of the propulsion direction with periods comparable to the running time seems to be difficult.

In this viewpoints, the Quincke roller whose propelling direction is not *a priori* determined, because the particle is just a spheric dielectric particle. The polarisation can be changed without a physical rotation. Therefore, the propelling direction of a Quincke roller is expected to be reversible by changing the external field. This is the reason to use Quincke rollers for the research on this thesis. Also, time-dependent self-propulsions by a global external field has been limited to the on/off [36, 39, 50] experimentally, so a sinusoidal self-propulsion is worth investigating. Therefore, the experiments of the Quincke rollers under a AC field were conducted in this thesis. Is the reciprocate motion expected experimentally realised? What is the properties of the reciprocating motion? Especially, what is the diffusion property? In what extent can the experimental results be explained in theory? How is the collective motion?

1.6 Organisation of the thesis

In the following of this thesis is divided into two parts. The first part Chapter 2 is the review on the Quincke roller which is usually driven by a DC electric field. Some experiments using the roller are also reviewed in Chapter 2. From the Chapter 3 to 5, the main results of this thesis is written. In Chapter 3, the experimental setup of the Quincke roller is explained mainly. In Chapter 4, the results on a single-particle dynamics experimentally and theoretically are presented and compared with each other. In Chapter 5, the experimental results on dynamic clustering are presented. Lastly, in Chapter 6, this thesis is concluded with the possible future perspective.

Chapter 2

An artificial self-propelled particle: the Quincke roller

In this chapter, researches on and around the Quincke roller are reviewed in detail. First, the Quincke effect which is the mechanism of the self-propulsion of the Quincke roller is described in Section 2.1. Secondly, other researches related to the Quincke effect are briefly mentioned in Section 2.2. Finally, the results of the Quincke roller under a DC field are reviewed in Section 2.3 which include collective motions of the Quincke rollers in experiments.

2.1 The Quincke effect

The Quincke effect is a rotating mechanism of particles which was discovered by G. Quincke in 1896 as an electrohydrodynamic effect [56]. Let us assume that a dielectric particle with dielectric permittivity ϵ_p is in the liquid with permittivity ϵ_l and electric conductivity σ_l. Consider the situation that the relaxation time of ions in liquid $\tau_l := \epsilon_l/\sigma_l$ is smaller than that on the surface of particle τ_p. When an electric field applied, the charges accumulate on the surface of the particle which makes the effective polarisation antiparallel to the field (Fig. 2.1 b)). This configuration is unstable because a small parallel perturbation of the polarisation is enlarged by the electric torque $\boldsymbol{P} \times \boldsymbol{E}$ (Fig. 2.1 c)). Therefore, if the torque surpasses the viscous torque, it starts to rotate spontaneously, which is the Quincke effect.

Before the quantitative derivation of the rotation, it is notable that the polarisation is not molecular polarisation but Maxwell-Wagner-Sillars polarisation (often abbreviated Maxwell-Wagner polarisation) [58] which is resulted from interfacial charges accumulation under the existence of the electric field.

Another remark is that the relaxation time for charges is generally determined as $\tau = \frac{\epsilon}{\sigma}$, where ϵ and σ are dielectric permittivity and electric conductivity. This relaxation is easily understood by the equation

$$\frac{\partial \rho}{\partial t} = -\frac{\rho}{\tau}, \tag{2.1}$$

which is derived by the combination of the Gauss' law, Ohm's law and conservation of

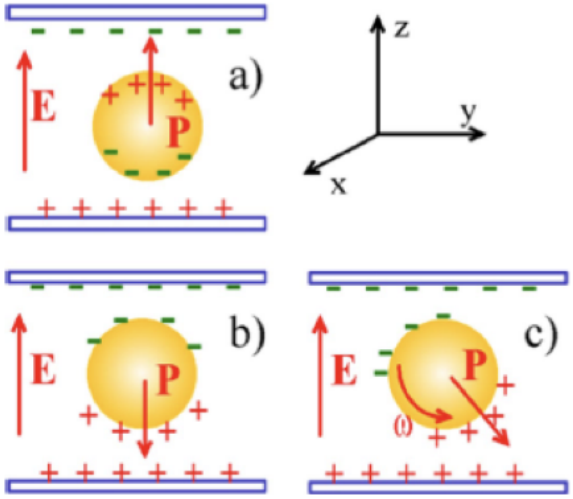

Figure 2.1: The Quincke effect [57] In a), no motion occurs. In b), it starts to rotate by a small perturbation that is illustrated in c).

charges:

$$\mathrm{div}\boldsymbol{E} = \frac{\rho}{\epsilon} \tag{2.2}$$

$$\boldsymbol{J} = \sigma \boldsymbol{E} \tag{2.3}$$

$$\frac{\partial \rho}{\partial t} + \mathrm{div}\boldsymbol{J} = 0. \tag{2.4}$$

2.2 Researches around the Quincke effect

Although the Quincke effect was discovered many years ago, related researches around the effect are still performed [57, 59–62]. One example is that the effective conductivity of a suspension increased by the Quincke rotation [57]. Another example is the chaotic rotation of the cylinder with a negligible inertia driven by the Quincke effect [59], which was experimentally realised and theoretically explained by Lorenz equation-like model.

2.3 The Quincke roller driven by the DC field

The Quincke roller is a dielectric colloid immersed in a conducting liquid and driven by a DC electric field as was mentioned in Section 1.2. The electrodes sandwiching the suspension are placed perpendicularly to gravity. The sedimented colloid rolls on the lower electrode by the rotation caused by the Quincke effect in the direction of an initial horizontal nonzero polarisation by fluctuation. Thus, the propulsion direction is not determined *a priori* unlike many other SPPs. The directions are totally random in the two dimension by the symmetry breaking. The important point is that all particles move perpendicular to the vertical electric field. Similarly to the Janus particle driven by a electric field [16], the Quincke roller is considered as one of the SPPs.

In this section, the quantitative description of the Quincke effect and the Quincke roller are reviewed. What is to be derived is the differential equation for the (Maxwell-Wagner)

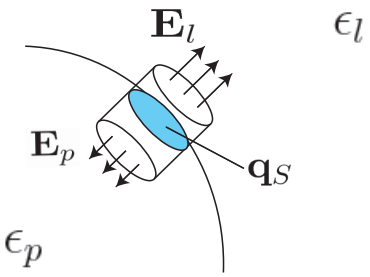

Figure 2.2: Gauss' law at the interface between particle and liquid

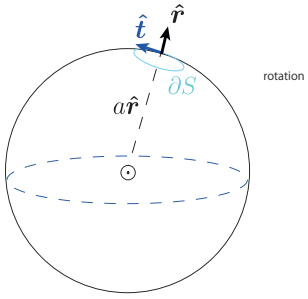

Figure 2.3: $\hat{\boldsymbol{t}} \times \hat{\boldsymbol{r}}$ is the direction going out from region ∂S along its surface.

polarisation defined by

$$\boldsymbol{P} = \int_{\text{surface}} dS q_s \hat{\boldsymbol{r}}, \tag{2.5}$$

which is integrated over the surface of a particle. Here, q_s and $\hat{\boldsymbol{r}}$ are the local surface density of charges and the unit vector of $\boldsymbol{r}$.

The polarisation obeys the following equation:

The equation from electrodynamics

$$\frac{\mathrm{d}\boldsymbol{P}}{\mathrm{d}t} + \frac{1}{\tau_{\mathrm{MW}}}\boldsymbol{P} = -\frac{2\pi\epsilon_0 a^3}{\tau_{\mathrm{MW}}}\boldsymbol{E}_0 + \boldsymbol{\Omega} \times (\boldsymbol{P} - 4\pi\epsilon_0 a^3 \chi^{\infty} \boldsymbol{E}_0). \tag{2.6}$$

Here, τ_{MW} is the Maxwell-Wagner time:

$$\tau_{\mathrm{MW}} = \frac{\epsilon_p + 2\epsilon_l}{2\sigma_l}. \tag{2.7}$$

Derivation of the polarisation dynamics Here the derivation of Eq. (2.6) which is basically from the supplementary information of Bricard *et al.*'s [8] was reviewed. First, assume the infinitesimally a small cylinder across a particle and the fluid as illustrated in Fig. 2.2, and apply the Gauss' law:

$$q_s = (\epsilon_l \boldsymbol{E}_l - \epsilon_p \boldsymbol{E}_p) \cdot \hat{\boldsymbol{r}}|_{r=a}, \tag{2.8}$$

where $\boldsymbol{E}_l$ and $\boldsymbol{E}_p$ are the electric field in liquid and particle. Here $\boldsymbol{E}_l(r > a)$ is

$$\boldsymbol{E}_l = \boldsymbol{E}_0 - \nabla\left(\frac{\boldsymbol{P} \cdot \boldsymbol{r}}{4\pi\epsilon_l r^3}\right), \tag{2.9}$$

because $\boldsymbol{P}$ makes the potential $\frac{\boldsymbol{P}\cdot\boldsymbol{r}}{4\pi\epsilon_l r^3}$. On the other hand, $\boldsymbol{E}_p(r < a)$ is

$$\boldsymbol{E}_p = \boldsymbol{E}_0 - \frac{\boldsymbol{P}}{4\pi\epsilon_l a^3} \tag{2.10}$$

By substituting Eq. (2.9) and Eq. (2.10) to Eq. (2.8), Gauss' law is rewritten as

$$q_s = \frac{2\epsilon_l + \epsilon_p}{4\pi\epsilon_l a^3} \boldsymbol{P} \cdot \hat{\boldsymbol{r}}. \tag{2.11}$$

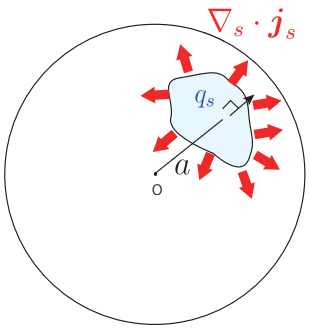

Figure 2.4: Schematic of surface divergence

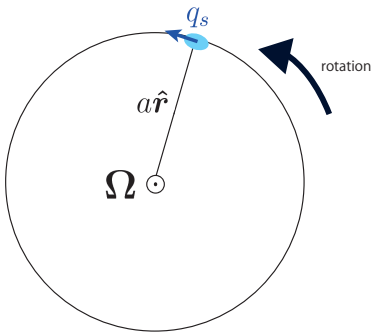

Figure 2.5: Observation in the lab frame

Let us consider the current density determined on a point of the surface $\boldsymbol{j}_s(\hat{\boldsymbol{r}})$ whose direction can be any direction in three-dimension. The charge conservation law on the surface is written as

$$\partial_t q_s + \nabla_s \cdot \boldsymbol{j}_s = 0, \tag{2.12}$$

where $\nabla_s \cdot \boldsymbol{j}_s$ means surface divergence which physically indicates the outgoing element from the area with attaching the surface. Here the surface divergence of $\boldsymbol{F}$ is defined as

$$\nabla_s \cdot \boldsymbol{F} = \hat{\boldsymbol{r}} \cdot \mathrm{rot}(\hat{\boldsymbol{r}} \times \boldsymbol{F}). \tag{2.13}$$

To understand the meaning of it, write the Stokes theorem for $\boldsymbol{G} = \hat{\boldsymbol{r}} \times \boldsymbol{F}$:

$$\int_S (\mathrm{rot}\boldsymbol{G}) \cdot \hat{\boldsymbol{r}} \mathrm{d}S = \oint_{\partial S} \hat{\boldsymbol{t}} \cdot \boldsymbol{G} \mathrm{d}s, \tag{2.14}$$

where $\hat{\boldsymbol{t}}$ is the unit vector along the boundary of area S anticlockwise as shown in Fig. 2.3.

For the equation Eq. (2.14), the right-hand side is transformed as

$$(r.h.s.) = \oint_{\partial S} \hat{\boldsymbol{t}} \cdot (\hat{\boldsymbol{r}} \times \boldsymbol{F}) \mathrm{d}s \tag{2.15}$$

$$= \oint_{\partial S} (\hat{\boldsymbol{t}} \times \hat{\boldsymbol{r}}) \cdot \boldsymbol{F} \mathrm{d}s. \tag{2.16}$$

Hence $\hat{\boldsymbol{t}} \times \hat{\boldsymbol{r}}$ is perpendicular to ∂S and the surface, the (r.h.s.) is the sum of the outgoing vectors (Fig. 2.4). On the other hand, the (l.h.s) of Eq. (2.14) corresponds to

$$(l.h.s.) = \int_S (\mathrm{rot}(\hat{\boldsymbol{r}} \times \boldsymbol{F}) \times \hat{\boldsymbol{r}}) \mathrm{d}S \tag{2.17}$$

$$= \int_S \nabla_s \cdot \boldsymbol{F} \mathrm{d}S. \tag{2.18}$$

Thus the surface divergence is the element of a vector field $\boldsymbol{F}$ outgoing from the closed area on the particle surface.

Now let us consider Ohm's law in the lab frame (See Fig. 2.5): [1]

$$\boldsymbol{j}_s = \sigma_l \boldsymbol{E}_l + q_s(\boldsymbol{\Omega} \times a\hat{\boldsymbol{r}}) \tag{2.19}$$

Finally, by combining Gauss' law (Eq. (2.11)), the charge conservation law (Eq. (2.12)) and Ohm's law (Eq. (2.19)), Eq. (2.6) is obtained.

[1] $\sigma_p = 0$ is assumed for dielectric particles

The dynamics of a roller The equation of motion of a sphere is written by

$$I\dot{\boldsymbol{\Omega}} = \frac{\epsilon_l}{\epsilon_0}(\boldsymbol{P}\times\boldsymbol{E}_0) - \mu_r^{-1}\boldsymbol{\Omega} \tag{2.20}$$

Here the inertia I is small enough to neglect for colloidal particles. (For example, $I = Ma^2 \sim 10^{-27}$ for polystyrene beads of 5μm.) Then the dynamics of $\boldsymbol{P}$ is obtained as follows:

The dynamics of $\boldsymbol{P}$ under the external field $\boldsymbol{E}_0$

$$\begin{aligned}&\frac{\mathrm{d}\boldsymbol{P}}{\mathrm{d}t} + \frac{1}{\tau_{\mathrm{MW}}}\boldsymbol{P}\\ =\ & -\frac{2\pi\epsilon a^3}{\tau_{\mathrm{MW}}}\boldsymbol{E}_0 + \mu_r\frac{\epsilon_l}{\epsilon_0}\Big[|\boldsymbol{P}|^2\boldsymbol{E}_0 - (\boldsymbol{E}_0\cdot\boldsymbol{P})\boldsymbol{P}\\ & -4\pi\epsilon_0 a^3\chi^\infty(\boldsymbol{P}\cdot\boldsymbol{E}_0)\boldsymbol{E}_0 + 4\pi\epsilon_0 a^3\chi^\infty|\boldsymbol{E}_0|^2\boldsymbol{P}\Big]\end{aligned} \tag{2.21}$$

The polarisation is divided into the instantaneous part (dielectric polarisation)$\boldsymbol{P}^\epsilon$ and the polarisation due to charges on the surface of the particle $\boldsymbol{P}^\sigma$:

$$\boldsymbol{P} = \boldsymbol{P}^\epsilon + \boldsymbol{P}^\sigma, \tag{2.22}$$

and only $\boldsymbol{P}^\sigma$ has nontrivial dynamics.

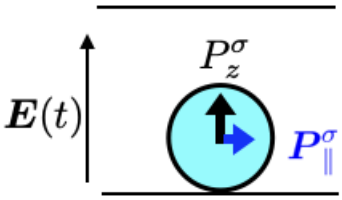

Figure 2.6: P_z^σ is the component parallel to the electric field

Therefore, by decomposing into parallel and z component shown in Fig. 2.6, these two equations:

The equations for polarisation dynamics for the DC field

$$\frac{\mathrm{d}P_\parallel^\sigma}{\mathrm{d}t} + \frac{1}{\tau_{\mathrm{MW}}}P_\parallel^\sigma = -\frac{\epsilon_l}{\epsilon_0}\mu_r E_0 P_z^\sigma P_\parallel^\sigma \tag{2.23}$$

$$\frac{\mathrm{d}P_z^\sigma}{\mathrm{d}t} + \frac{1}{\tau_{\mathrm{MW}}}P_z^\sigma = \frac{\epsilon_l}{\epsilon_0}\mu_r E_0 P_\parallel^{\sigma 2} - \frac{4\pi\epsilon_0 a^3}{\tau_{\mathrm{MW}}}(\chi^\infty + 1/2)E_0. \tag{2.24}$$

are obtained (They are Eqs. (S6) and (S7) in [8]).

A DC roller in unbounded liquid If $E_0 > E_Q$, where the threshold electric field E_Q is

$$E_Q = \frac{1}{\sqrt{4\pi\epsilon_0 a^3(\chi^\infty + 1/2)\mu_r\tau}}, \tag{2.25}$$

the equation for a DC roller Eq. (2.23) and Eq. (2.24) have the unique steady and stable solution:

$$P_{\parallel}^{(\mathrm{DC})}(\mathrm{SS}) = P_{\parallel}^{\sigma\,(\mathrm{DC})}(\mathrm{SS}) = \frac{\epsilon_0}{\epsilon_l} \cdot \frac{1}{\mu_r \tau_{\mathrm{MW}} |\boldsymbol{E}_0|} \sqrt{(\frac{E_0}{E_Q})^2 - 1} \tag{2.26}$$

$$P_z^{\sigma\,(\mathrm{DC})}(\mathrm{SS}) = -\frac{1}{\mu_r \tau_{\mathrm{MW}} E_0} \cdot \frac{\epsilon_0}{\epsilon_l}, \tag{2.27}$$

Here,

$$P_z^{(\mathrm{DC})}(\mathrm{SS}) = P_z^{\epsilon\,(\mathrm{DC})}(\mathrm{SS}) + P_z^{\sigma\,(\mathrm{DC})}(\mathrm{SS}) = 4\pi\epsilon_0 a^3 \chi^{\infty} E_0 - \frac{1}{\mu_r \tau_{\mathrm{MW}} E_0} \cdot \frac{\epsilon_0}{\epsilon_l}, \tag{2.28}$$

including the instantaneous part.

Note on the properties Let us make a deeper understanding of the steady solution above. Suppose the deviation of P_z is much slower than that of $\boldsymbol{P}_{\parallel}$. Because P_z is constant, Eq. (2.24) is deduced as

$$P_z^{\sigma} = -\tau_{\mathrm{MW}} \left[\frac{\epsilon_l}{\epsilon_0} \mu_r E_0 P_{\parallel}^{\sigma 2} - \frac{4\pi\epsilon_0 a^3}{\tau_{\mathrm{MW}}} (\chi^{\infty} + 1/2) E_0 \right]. \tag{2.29}$$

Thus $P_{\parallel}$ obeys

$$\begin{aligned} \frac{\mathrm{d}P_{\parallel}^{\sigma}}{\mathrm{d}t} &= -(\frac{\epsilon_l}{\epsilon_0}\mu_r E_0)^2 \tau_{\mathrm{MW}} P_{\parallel}^{\sigma 3} + \left[4\pi a^3 \mu_r \epsilon_l (\chi^{\infty} + \frac{1}{2}) E_0^2 - \frac{1}{\tau_{\mathrm{MW}}} \right] P_{\parallel}^{\sigma} \\ &= -(\frac{\epsilon_l}{\epsilon_0}\mu_r E_0)^2 \tau_{\mathrm{MW}} P_{\parallel}^{\sigma 3} + 4\pi a^3 \mu_r \epsilon_l (\chi^{\infty} + \frac{1}{2})(E_0^2 - E_Q^2) P_{\parallel}^{\sigma}. \end{aligned} \tag{2.30}$$

The sign of the first order of $P_{\parallel}^{\sigma}$ in the r.h.s. changes its stability (supercritical pitchfork bifurcation). The initial direction of $P_{\parallel}^{\sigma}$ which is chosen arbitrary in $xy-$ space is invariant over time till steady states. Let us consider the three cases as follows:

1. If $E_0 = E_Q$,
   $P_{\parallel}^{\sigma}(\mathrm{SS}) = 0$ is the sole stable point. The relaxation is slow as $t^{-1/2}$. By Eq. (2.29), $P_z^{\mathrm{SS}} = 2\pi\epsilon_0 a^3 E_0$. The angular velocity in steady state vanishes: $\boldsymbol{\Omega}^{\mathrm{SS}} = 0$, which means the particle keep stationary.

2. If $E_0 < E_Q$,
   $P_{\parallel}^{\sigma}(\mathrm{SS}) = 0$ is the stable fixed point. The relaxation is exponential. By Eq. (2.29), $P_z^{\mathrm{SS}} = -2\pi\epsilon_0 a^3 E_0$, and still $\boldsymbol{\Omega}^{\mathrm{SS}} = 0$.

3. If $E_0 > E_Q$,
   $P_{\parallel}^{\sigma}(\mathrm{SS}) = 0$ is the unstable fixed point. The relaxation is exponential. In the stable fixed point, the polarisations are Eqs. (2.26) and (2.27) in the former paragraph. I would like to note that $P_z(\mathrm{SS})$ can alter its sign: Set $E_0 = E_Q'$ when $P_z(\mathrm{SS}) = 0$. Then
   $$E_Q' = \frac{1}{\sqrt{4\pi\epsilon_0 a^3 \chi^{\infty} \mu_r \tau}} > \frac{1}{\sqrt{4\pi\epsilon_0 a^3 (\chi^{\infty} + 1/2) \mu_r \tau}} = E_Q. \tag{2.31}$$
   When $E_Q < E_0 < E_Q'$, $P_z(\mathrm{SS}) < 0$. When $E_0 > E_Q'$, $P_z(\mathrm{SS}) > 0$.

Translation motion by rolling on electrode Torque balance of a roller (Eq. (S4) of [8]):

$$\begin{pmatrix} \boldsymbol{v}/a \\ \boldsymbol{\Omega} \\ \Omega_z \end{pmatrix} = \begin{pmatrix} \mu_t \boldsymbol{I} & \tilde{\mu}_t \boldsymbol{\Lambda} & 0 \\ -\tilde{\mu}_r \boldsymbol{\Lambda} & \mu_r \boldsymbol{I} & 0 \\ 0 & 0 & \mu_\perp \end{pmatrix} \begin{pmatrix} a\boldsymbol{F}^e_\parallel \\ \boldsymbol{T}^e_\parallel \\ T^e_z \end{pmatrix} \tag{2.32}$$

where $\boldsymbol{\Lambda} = \begin{pmatrix} 0 & 1 \\ -1 & 0 \end{pmatrix}$, which means $-\pi/2$ rotation in xy-plane. The electric force $\boldsymbol{F}^e$ and the electric torque $\boldsymbol{T}^e$ are written as

$$\boldsymbol{F}^e_\parallel = \frac{\epsilon_l}{\epsilon_0}(\boldsymbol{P}\cdot\nabla)\boldsymbol{E}_0 \tag{2.33}$$

$$\boldsymbol{T}^e_\parallel = \frac{\epsilon_l}{\epsilon_0}\boldsymbol{P}\times\boldsymbol{E}_0 \tag{2.34}$$

Eq. (2.32) is valid also for non-steady state.

Here the electric force by net charge by the surface of the particle is assumed to be zero ($\boldsymbol{F}^e = 0$), so

$$\boldsymbol{v} = a\tilde{\mu}_t \boldsymbol{\Lambda}\boldsymbol{T}^e_\parallel \tag{2.35}$$

$$= \frac{\epsilon_l}{\epsilon_0} a\tilde{\mu}_t \boldsymbol{\Lambda}\boldsymbol{P}\times\boldsymbol{E}_0 \tag{2.36}$$

$$= \frac{\epsilon_l}{\epsilon_0} a\tilde{\mu}_t \boldsymbol{\Lambda}\boldsymbol{P}^\sigma_\parallel\times\boldsymbol{E}_0 \tag{2.37}$$

$$= -\frac{\epsilon_l}{\epsilon_0} a\tilde{\mu}_t E_0 \boldsymbol{P}^\sigma_\parallel. \tag{2.38}$$

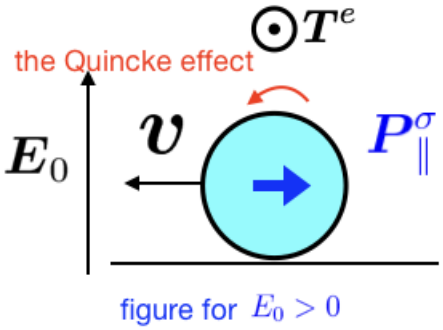

Figure 2.7: The Quincke roller under the DC field in steady states ($E_0 > 0$)

Here, $\tilde{\mu}_t$ effectively includes the effects of the surface roughness' of the electrode and the particle and the lubrication layer. The surface friction $\tilde{\mu}_t$ logarithmically increases as the lubrication layer decreases [8, 63]. In the DC case [8], the lubrication layer was assumed 10-100nm.

Using the steady solution of $P_\parallel$ of Eq. (2.26), the translation speed in steady state v_0 is

$$v_0 = \frac{a\tilde{\mu}_t}{\mu_r \tau_{\mathrm{MW}}}\sqrt{\left(\frac{E_0}{E_Q}\right)^2 - 1}. \tag{2.39}$$

T	L	M	Q
$1/D_\theta$	a	$\frac{1}{\mu_r D_\theta}$	$\varepsilon_0 E_0 a^2$

Table 2.1: Unit for nondimensionalisation

For computing the time evolutions of Eq. (2.23) and Eq. (2.24) numerically, they were nondimensionalised using the unit in Table. 2.1 as follows: (assuming adding rotational noises in 2D cases) Thus,

$$\tilde{t} = D_\theta t \tag{2.40}$$

$$\tilde{P} = \frac{P}{\varepsilon_0 E_0 a^3}, \tag{2.41}$$

The tilde indicates the dimensionless value here. Note that "polarisation" $\boldsymbol{P} = \int \mathrm{d}^2 s q_\mathrm{S} \hat{\boldsymbol{r}_\mathrm{S}}$ with the dimension of QL^3. Therefore, Eq. (2.23) and Eq. (2.24) are nondimensionalised as follows:

$$\frac{\mathrm{d}\tilde{P}_\parallel^\sigma}{\mathrm{d}\tilde{t}} + \frac{1}{\tau_{\tilde{\mathrm{MW}}}} \tilde{P}_\parallel^\sigma = -A \tilde{P}_z^\sigma \tilde{P}_\parallel^\sigma \tag{2.42}$$

$$\frac{\mathrm{d}\tilde{P}_z^\sigma}{\mathrm{d}\tilde{t}} + \frac{1}{\tau_{\tilde{\mathrm{MW}}}} \tilde{P}_z^\sigma = A \tilde{P}_\parallel^{\sigma\,2} - \frac{4\pi}{\tau_{\tilde{\mathrm{MW}}}} (\chi^\infty + 1/2) \tag{2.43}$$

Here A and $\tilde{\tau}_\mathrm{MW}$ are the dimensionless values which are defined as

$$A = \frac{\mu_r \varepsilon_l E_0^2 a^3}{D_\theta} \tag{2.44}$$

$$\tilde{\tau}_\mathrm{MW} = \tau D_\theta. \tag{2.45}$$

Then the dimensionless version of Eq. (2.38) (dimensionless translation velocity) is written as

$$\tilde{\boldsymbol{v}} = -\frac{\tilde{\mu_t}}{\mu_r} A \tilde{\boldsymbol{P}}_\parallel^\sigma. \tag{2.46}$$

Practically, velocity is expressed using dimensionless values as

$$v = -\frac{a\tilde{\mu_t}}{\mu_r \tau_\mathrm{MW}} \cdot \tau_{\tilde{\mathrm{MW}}} A \tilde{P}_\parallel^\sigma, \tag{2.47}$$

including the sign.

Numerical solution of transient dynamics To know the transient dynamics before steady states, the numerical solutions of Eq. (2.23) and Eq. (2.24) (or the dimensionless counterparts: Eq. (2.42) and Eq. (2.43)) appeared in Fig. 2.8.

For our numerical calculation, the parameters were set as follows:

Parameter for numerical calculation

- Electric field: $E_0 = 7.1 \times 10^6$ V/m
- $E_Q \simeq 9.5 \times 10^5$V/m, $V_Q \simeq 28$V
- Channel width: 30μm
- Radius of a particle: $a = 2.5 \times 10^{-6}$ m
- $\epsilon_l \sim 2\epsilon_0$ [8, 57]
- $\chi^\infty = 0.001$[a]
- Viscosity: $\eta = 2\text{mPa} \cdot \text{s}^{-1}$
- Rotational friction is calculated by $\mu_r = \frac{1}{8\pi\eta a^3}$
- $\tau_{\text{MW}} \sim 1$ms [8, 57]
- D_θ is just the unit of time as far as 1D motions are considered.

[a] This is an assumption. $\chi^\infty \ll 1/2$ when $E_0 < 3E_Q$ is supported by [57], though it was assumed for also $E_0 > 3E_Q$.

$\frac{a\tilde{\mu_t}}{\mu_r \tau_{\text{MW}}} = 82.1\mu$m/s was assumed for a reason of consistency to our experiment of AC system discussed later in Section 4.4. In the literature [8, 47], they use 2mm/s in theory assuming the lubrication layer underneath the particle to be the order of 10-100nm or 1.5mm/s for the coefficient $\frac{a\tilde{\mu_t}}{\mu_r \tau_{\text{MW}}}$ of Eq. (2.39) by fitting from their DC experiments. Hence the material of particle, the channel width, and the electric field are different from our experiment, there is no reason to coincide.

For comparison, the parameters set by Bricard *et al.* [8] were the following:

- Electric field: E_0=$1.39E_Q$
- $E_Q \sim 1.0 \times 10^6$ V/m, $V_Q \sim 2 \times 10^2$V
- Channel width: 220μm
- Radius of a particle: $a = 2.4 \times 10^{-6}$ m
- $\epsilon_l \sim 2\epsilon_0$ [8, 57]
- $\chi^\infty << 1/2$
- Viscosity: $\eta = 2\text{mPa} \cdot \text{s}^{-1}$
- $\tau_{\text{MW}} \sim 1$ms [57]

This nondimensionalisation did not appear in these literature [8, 47]. Especially, D_θ appears as just the unit of time in this one-dimensional case.

Polarisations oscillate at $\sim \tau_{\text{MW}}$ and go to the constant values, though this non-steady oscillation was not mentioned in [8, 47]. It is remarkable that this constant value corresponds to the fixed points which only depend on the initial sign of $P_\parallel$, as it is seen in Eq. (2.30). Another remark is that $P_\parallel$ never alters its sign.

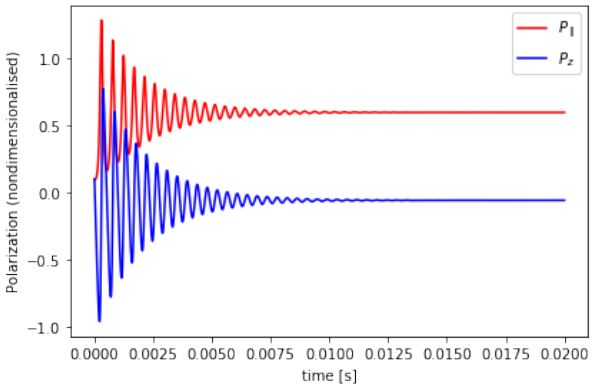

Figure 2.8: Polarisations (only the interfacial part) relax to constant. (initial conditions: $\tilde{P}_\parallel^\sigma(0) = 0.1$, $\tilde{P}_z^\sigma(0) = 0.1$)

The velocity and the position as functions of t are shown in Fig. 2.9. After a short transient time, the velocity reach to a constant value whose sign is inverse of the sign of $P_\parallel^\sigma$ when $E_0 > 0$ (Fig. 2.7), so the position almost grows linear in time. In the transient time, the velocity oscillates at $\sim \tau_{\mathrm{MW}}$ though the velocity do not change its sign. This oscillation is due to the reconfiguration time of the surface charges. Since the displacement during the transient time and time length are small, there is no experimental report to capture this oscillation yet.

In the DC case, there is the rigorous expressions of steady solution Eq. (2.26) and Eq. (2.27), for the electric field $E_0 = 7.07 \times 10^6$, for example, $P_\parallel^\sigma$(SS)=0.6, P_z^σ(SS)=-0.06 (dimensionless values) if the initial $P_\parallel^\sigma$ is positive.

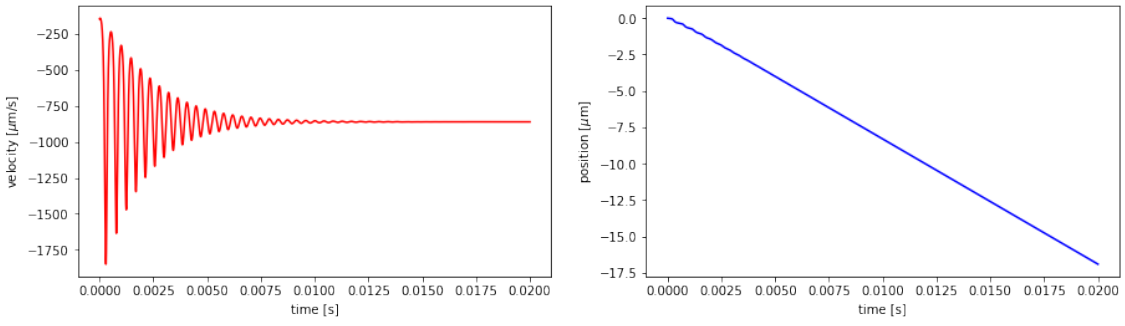

Figure 2.9: Velocity (left), position (right). (initial conditions: $\tilde{P}_\parallel^\sigma(0) = 0.1, \tilde{P}_z^\sigma(0) = 0.1$)

Lastly, it can be checked that the nondimensionalised inertia is also sufficiently small:

$$\tilde{I} = \mu_r I D_\theta \sim 10^{-7}. \tag{2.48}$$

2.3.1 A simple model for a roller on a plane

Because a Quincke roller moves with constant speed in steady states, they simply modelled the motion in a 2D-plane by adding rotational diffusion noise.

$$\dot{\boldsymbol{x}} = v_0 \hat{\boldsymbol{n}}(t) \tag{2.49}$$

$$\dot{\theta} = \sqrt{2D_\theta}\xi(t) \tag{2.50}$$

$\hat{\boldsymbol{n}}(t) = (\cos\theta(t), \sin\theta(t))$ is the propelling direction vector. The noises satisfy $\langle \xi(t) \rangle = 0$ and $\langle \xi(t)\xi(t') \rangle = \delta(t - t')$, which means a white Gaussian noise.

The time autocorrelation of velocity is

$$\langle \boldsymbol{v}(t_1) \cdot \boldsymbol{v}(t_2) \rangle = v_0^2 e^{-D_\theta |t_1 - t_2|} \tag{2.51}$$

The inverse of the rotation diffusion constant measured by dilute experiment [47] was $D_\theta^{(\mathrm{DC})-1} = 0.31 \pm 0.02$s which is apparently smaller than the time scale of thermal rotation diffusion ($\sim 10^2$s)(See appendix Eq. (B.4)).

For this model, the MSD is calculated as follows:

$$\mathrm{MSD}^{\mathrm{DC}}(\tau, t) = \mathrm{MSD}^{\mathrm{DC}}(\tau) = \frac{2v_0^2}{D_\theta^2}(e^{-D_\theta \tau} - 1 + D_\theta \tau). \tag{2.52}$$

2.3.2 Interaction between the Quincke rollers under the DC field

The interactions between the Quincke rollers are two kinds: electrostatic interaction of the polarisation $\boldsymbol{P}$ and hydrodynamic interaction.

Electrostatic interaction First, let us consider electrostatic interaction. The parallel component of the electric disturbance field produced at $\boldsymbol{x}_i$ by the particle j is

$$\delta \boldsymbol{E}_\parallel^{(j)}(\boldsymbol{x}_i, t) = \frac{3}{2\pi\epsilon_0 x_{ij}^3}\left[\frac{a}{x_{ij}} P_z \hat{\boldsymbol{x}}_{ij} - \frac{a^2}{x_{ij}^2} P_\parallel \hat{\boldsymbol{n}}_j \cdot (5\hat{\boldsymbol{x}}_{ij}\hat{\boldsymbol{x}}_{ij} - \boldsymbol{I}) + \mathcal{O}(\frac{a^3}{x_{ij}^3})\right], \tag{2.53}$$

where $\boldsymbol{x}_{ij}$ and $\hat{\boldsymbol{x}}_{ij}$ are the relative vector between particles i and j and its unit vector. $\boldsymbol{I}$ is the identity matrix. The disturbance field is illustrated in Fig. 2.10.

For $E_0 > 0$, the velocity and the parallel component of the polarisation is antiparallel, so A of Fig. 2.10 indicates the repulsion between particles. $\hat{\mathbf{p}}$ means the propelling direction of the particle at the centre of the figure. B of Fig. 2.10 is a dipolar field. It suggests that a particle tend to move in the same direction as that of the centre at the front and the back relatively. That is to say, particles tend to align when their configuration is long in their moving direction and do not align in the other configuration.

Hydrodynamic interaction Secondly, the hydrodynamic interaction is discussed as follows. The flow field at $\boldsymbol{x}_i$ produced by the particle j is $\boldsymbol{u}^{(j)}$. When we consider the effect of the flow to the particle rotation, z-direction differentiation of the parallel flow field is relevant. This was calculated as Eq. (2.54):

$$\partial_z \boldsymbol{u}_\parallel^{(j)}\Big|_{z=0}(\boldsymbol{x}_i, t) = \begin{cases} \frac{6\mu_r}{a\tilde{\mu_t}} v_0 \frac{a^3}{x_{ij}^3}(\hat{\boldsymbol{n}}_j \cdot \hat{\boldsymbol{x}}_{ij})\hat{\boldsymbol{x}}_{ij} & \text{for } x_{ij} < H/\pi \\ \frac{6\mu_r}{H\tilde{\mu_t}} v_0 \frac{a^2}{x_{ij}^2} \hat{\boldsymbol{n}}_j \cdot (2\hat{\boldsymbol{x}}_{ij}\hat{\boldsymbol{x}}_{ij} - \boldsymbol{I}) & \text{for } x_{ij} \gg H/\pi, \end{cases} \tag{2.54}$$

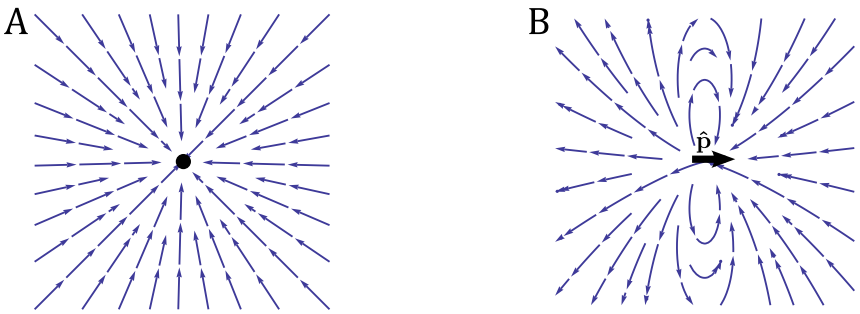

Figure 2.10: Electrostatic disturbance by a roller [8]. A: the isotropic part which corresponds to the first term of Eq. (2.53). B: the unisotropic part of Eq. (2.53).

where $\hat{\boldsymbol{n}}_j$ is the unit vector of the propelling direction which is denoted as $\hat{\mathbf{p}}$ in the Figs. 2.10 and 2.11.

The flow is visualised in Fig. 2.11 for each range. In short-range of $x_{ij} < H/\pi$, there is the alignment flow depicted in A of Fig. 2.11. In the range of $x_{ij} \gg H/\pi$, the dipolar flow is created so that the alignment of particles is to be destroyed.

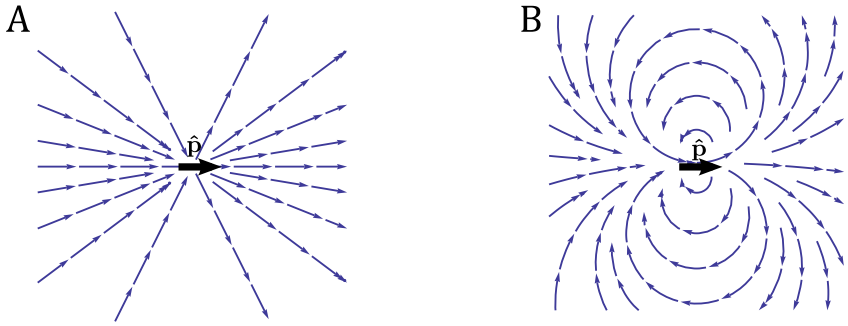

Figure 2.11: Hydrodynamic flow by a roller [8]

The Eq. (2.54) was derived by assuming a point torque exists at the distance of the particle radius from the lower electrode. The flow field produced by a point torque in the vicinity of plane is known as the calculation by Blake *et al.* [64]. This is applied to the case that a point torque existing between two planes by Hackborn [65], which was used for obtaining Eq. (2.54).

In the paper by Bricard *et al.* [8], they assumed particles do not change their speeds but only change the directions by interactions. Though they succeeded to reproduce the collective motions which they experimentally observed under this assumption with bipartite interactions, another research reported that the speeds of the Quincke roller can be changed by interactions [66].

2.3.3 Collective motion of the Quincke rollers driven by the DC field

The Quincke rollers under a DC field collectively migrate because of the interaction explained above [8, 47]. In the two literature [8, 47], the channel width H was large as $H = 220\mu$m so that the short-range hydrodynamic interaction in the left of Fig. 2.11 dominated. Thus, the particles tended to align their propelling directions if the number density was large. The Fig. 2.12 shows the appearance of macroscopic directed motions in the race track shape boundary. In the low number density, particles' directions were isotropic. In the middle range of the number density, the band in which the particles were migrating in one direction appeared. In the large number density, the polar liquid phase which consists of particles aligning their propelling directions but their positions are liquid-like were appeared [8].

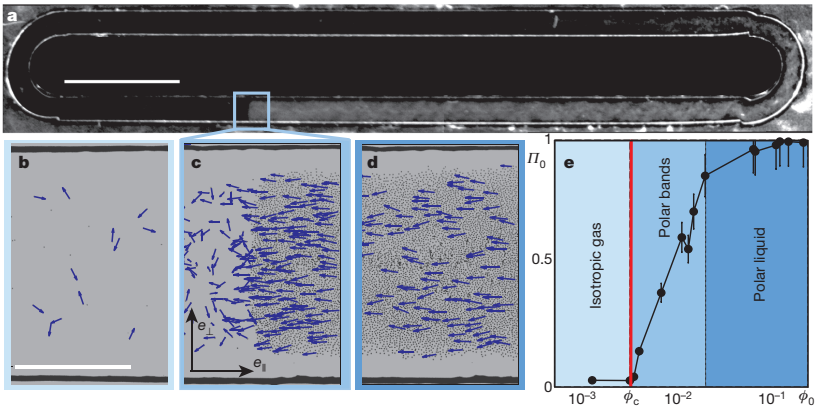

Figure 2.12: Macroscopic directed motion [8]. The width of the track was 1mm.

Another situation is the confinement in a circular region [47]. Similarly to the above case, a rotating vortex appeared when the number density was large enough as shown in Fig. 2.13 thanks to the alignment interactions.

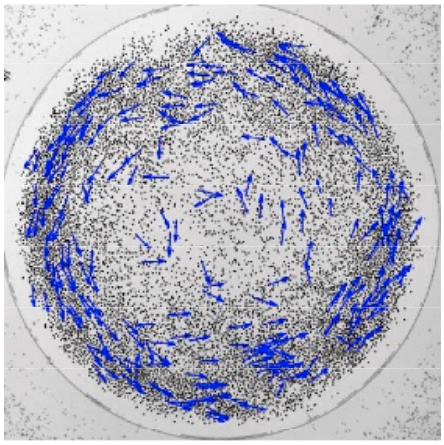

Figure 2.13: Vortex formed along the circular boundary [47]. The radius of the region was 1mm.

The Quincke rollers driven by a DC pulse sequence As explained in Section 1.2, the switchings of the DC electric field in (a) of Fig. 1.10 bare the changes of the single-particle motion [50]. Collective motions which depend on the rest time τ_T and the running time τ_R were also reported in this system [50] as shown in Fig. 2.14 Surprisingly, the particles form various types of dynamic clusters as shown in Fig. 2.14.

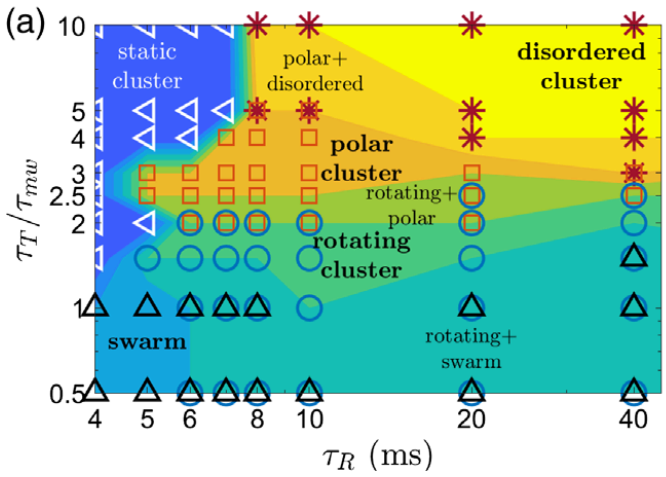

(a) Phase diagram of the collective motions

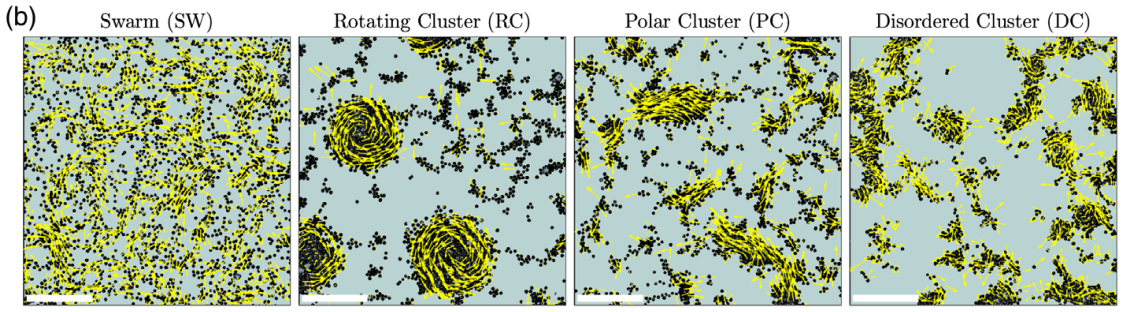

(b) Collective motions (Scale bar=1mm)

Figure 2.14: Collective motions of the Quincke roller driven by the DC pulse sequence [50]

In their single-particle analysis, $\tau_T/\tau_{\mathrm{MW}} \simeq 2$ is the boundary of the memory-effect existence.

2.4 Summary on the researches on the Quincke rollers

In summary, the Quincke roller is the SPP rolling on an electrode by the electrohydrodynamic effect called the Quincke effect [56, 67]. The effect occurs to dielectric particles dispersed in a conducting liquid when a sufficiently large DC electric field is applied. The single-particle dynamics is ruled by the polarisation dynamics on the surface of the particle, which is nonlinear differential equations [8]. They have the stable steady solution which corresponds to the motion with a constant speed. The particles interact by the

electrostatic interaction of the polarisations and the hydrodynamic interaction. Experimentally, not only the single-particle straight motion but also collective motion such as the polar liquid and the vortex along the confined region were reported [8, 47]. By applying the DC pulse sequences, various collective motions including cluster formations were realised [50].

Chapter 3

Experimental setup: the Quincke rollers under the AC field

In this chapter, the experimental setup and the procedures of the Quincke rollers under the AC electric field are illustrated.

3.1 Experimental setup

The Quincke rollers are realised by applying the electric field vertically to the suspension sandwiched by two electrodes as shown in Fig. 3.1. The colloidal particles sediment on the lower electrode of the Quincke cell which is explained in the following paragraph. The electric apparatus' used and the data acquisition is explained in the next paragraph.

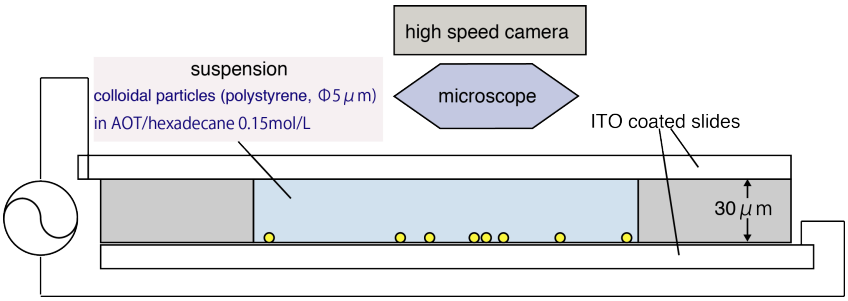

Figure 3.1: Experimental setup

The Quincke cell preparation Here, how to prepare the Quincke cell are explained. The solution is chemically same as what Bricard *et al.* [8, 47] used. Before dispersing colloids to the solution, rinsing of particles is needed as follows:

- The protocol to rinse colloidal particles

    1. Make the solution AOT[1]/hexadecane 0.15mol/L.

[1]surfactant. di-2-ethylhexyl sodium sulfosuccinate, minus ion in water. The chemical formula is shown in Fig. A.1.

2. Centrifuge polystyrene beads dispersed in water (GS0500, Thermo Scientific) which was taken into a microtube[2]. The diameter is 5μm.

3. Remove the supernatant.
4. Add the solution 1 to the microtube and make it disperse.
5. Centrifuge it.
6. Repeat the procedure from 3 to 5 six times.

- ITO coated slide glasses[3] were washed using alkaline cleaner SDNU-A1 (As One).
- The rinsed particles were suspended in the solution (AOT/hexadecane 0.15mol/L). Then the suspension was sandwiched by the ITO coated slide glasses using double-sided tapes (width=30μm)[4] as a spacer.

Because of the density difference (Cf. Appendix A), polystyrene colloids are on the lower electrode as illustrated in Fig. 3.1 in equilibrium. The channel width was set to 30μm, which is smaller than that set in the literature [8, 47]. This can change that the far-field effective hydrodynamic field in Fig. 2.11 B become more dominant than A. More precisely, for the short-range of the interparticle distance $r < 10\mu$m (=twice the particle's diameter), the alignment flow A is dominant, while dipolar flow B is dominant for $r > 10\mu$m.

Electrical circuit and data acquisition Then, the AC electric field was applied to the prepared Quincke cell using function/arbitrary waveform generator 33220A, 20MHz (Agilent) with amplification by the power amplifier TA120 (NF). The electric field applied to the cell was continuously measured by a digital multimeter: 34401A (Hewlett Packard). The motions were captured via a bright-field inverted microscope IX70 (Olympus) with objective lens' LUCPlanFL 40x/0.60 $\infty/0-2$ or UPlanFl 10x/0.30 ∞/- and a high speed camera (Fastcam mini AX (Photron)[5]). The capture rate (fps) was set to the multiple of the applied frequencies. (Typically 10 or 20 slices per period)

3.2 Image analysis

In this setup, all images obtained were 1.32μm/pixel (0.756 pixel/μm) in x10 and 0.314μm/pixel (3.18 pixel/μm) in x40. Before the analysis, particles on the lower electrode that did not stick to other particles were carefully chosen, because some particles exist above the lower electrode under the electric field or aggregate perpendicularly or horizontally. After the selection by eye, the positions of particles were tracked via binarisation of images using MATLAB or imageJ (Mosaic Particle Tracker [68]) by the following procedures basically:

1. Subtract the time average background image if it is necessary.
2. Enhance the contrast of it.
3. Binarise it. Then a particle became an annulus.

[2] Simfort T330-7LST
[3] $30 \times 60 \times 1.1$ (mm), ITO thickness 50nm.
[4] NITTO, No.5603, PET with acrylic adhesive.
[5] full resolution: 1024×1024 pixels. 4000fps is the upper limit which is possible for the full resolution.

4. Fill holes. The particle became a circular disk.
5. Perform segmentation by watershed transformation if it is necessary.

The necessity of the procedures and the thresholds for binarisation depended on movies.

Chapter 4

A single Quincke roller under the AC field

In this chapter, the dynamics of a single Quincke roller is focused on. First, the experimental results are shown in Sections 4.1 and 4.2. Then the polarisation dynamics under the DC field in Section 2.3 is generalised to the AC field in Sections 4.3 and shown in Section 4.4.

4.1 Overview of Experimental results

Before showing experimental results in detail, let us overview behaviours of the Quincke rollers under the AC field in our experiments.

Because AC electric voltages are applied, there are two parameters: effective value of voltage and frequency. In theory, the Quincke rollers are always staying on the two-dimensional plane (=the lower electrode) in any effective values over a threshold and any frequencies smaller than $\sim 1/\tau_{\mathrm{MW}}$. However, the particles stayed on the plane with only a small range of the parameter space experimentally. In the other range, the colloidal particles levitated, so they did not stay the two dimensional plane even though the density of the particle is larger than the liquid. Under those parameters, particles assembled and dissembled three-dimensionally and periodically.

In this thesis, the range of parameters which yields two-dimensional motions was focused on. The AC electric field are applied to dilute suspensions initially dispersed. After a moment, some particles made clusters and others did not as shown in Fig. 4.1. The cluster was like "dynamic clustering" [32] in the sense that clusters assemble and disassemble temporally, though the clusters was persistent during the time scale over 100 periods. Typically, the persistent clusters are made of two or three particles. Here they are named a doublet and a triplet for a two-particle cluster and a three-particle cluster. Population of doublets is larger than that of triplets. More than three-particle clusters were observed as well, which were rare compared to triplets. The trajectories in Fig. 4.1 are for 1.0 seconds (=200 periods) captured stroboscopically at the frequency of the external field.

In Section 4.2 of this chapter, single particle motions were analysed and discussed. In Chapter 5, the dynamic clustering was analysed and discussed.

Lastly for the overview, let us remark an experimental situation. When the AC field with DC elements were applied, the Quincke cell burned after applying voltages for around 30 minutes and particles are gradually aggregated on the edge of the double-sided tape as

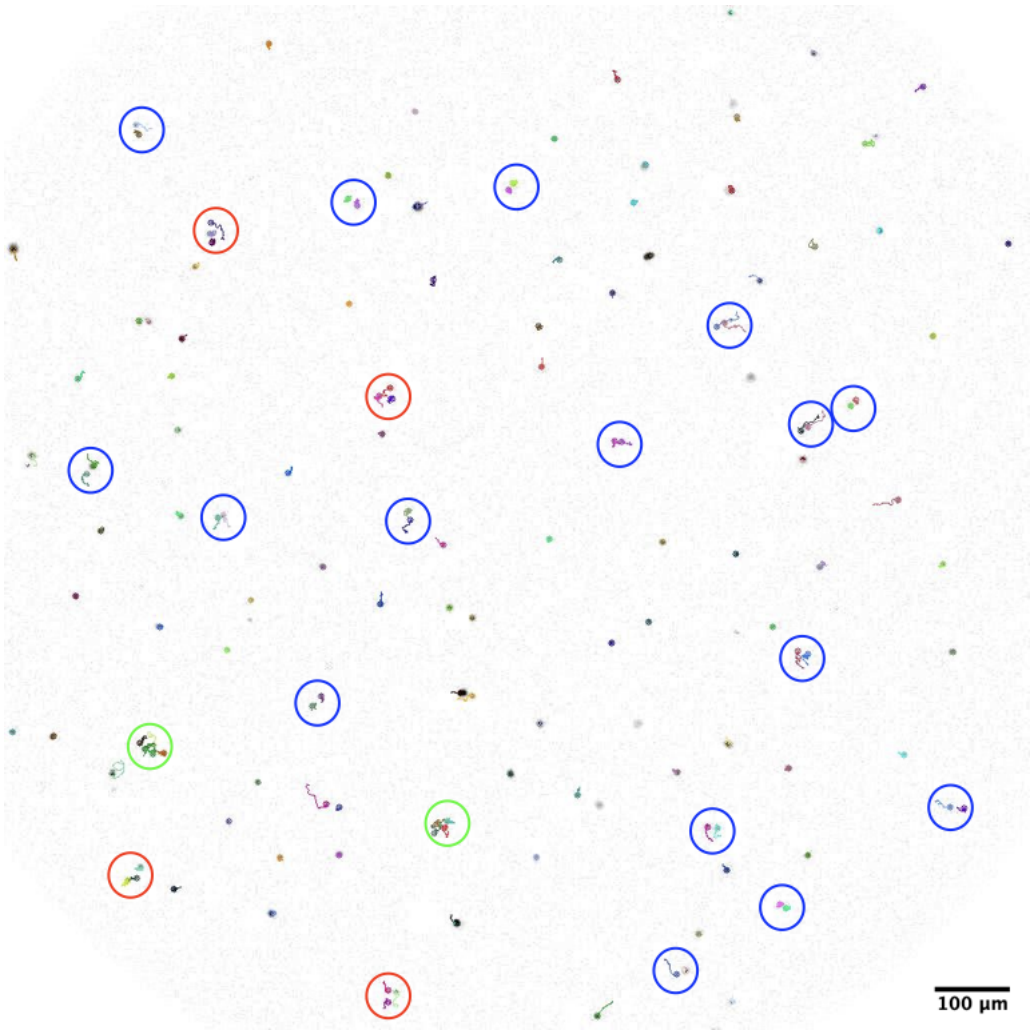

Figure 4.1: Dynamic Clustering (x10, 200Hz, 150V_{eff}). Trajectories for 1.0s (=200 periods). The blue, red, and green circles are doublets, triplets, and the clusters made of more than three particles.

the spacer. Therefore, it is difficult to measure with many parameters using the same cell and in the same number density of particles, though the available time of cells is enough for producing collective motion as realised by Bricard *et al.* [8, 47].

In contrast, the zero DC element of voltage avoids the cell burning, so that a Quincke cell can be used repeatedly. However, similarly to the DC case, it is difficult to maintain the number density of particles for a long time. Hence the number density affect collective motion as well as in the DC case [8, 47], a single cell cannot be used repeatedly.

4.2 Experimental results: motions of a single particle in dilute suspension

In this section, motions of an isolated single particle in dilute suspension which was obtained experimentally are focused on. The typical distance from other particles was more than 100μm. First, the external parameter: effective voltage and frequency are fixed to $V_{\text{eff}} = 150$V and 300Hz. Here the motion is captured at 3000fps (one period=10 slices) and by x40 objective lens.

4.2.1 Typical dynamics

Typical trajectory and velocity A typical trajectory of the Quincke roller under the AC field for long-time range is shown in (a) of Fig. 4.2. The time length 3.639s corresponds to approximately 1091 periods. For the comparison of the Quincke particle under the AC field to Brownian particles, the typical trajectory of a particle in the Quincke setup but with no electric field is depicted in (b) of Fig. 4.2 (captured at 4000fps). The trajectory of the Quincke roller is random-like, but it moved much more than the Brownian particle.

To see the typical changes in position and velocity, position $x(t)$, $y(t)$ and velocity $v_x(t)$, $v_y(t)$ for a short-time range are shown in (a) and (b) of Fig. 4.3, where the indice x, y mean x, y-components. The root mean square velocity is measured as $v_{\text{RMS}} = \sqrt{\overline{v^2(t)}} \sim 6 \times 10^2 \mu$m/s, where the overline indicates the average over the whole time series for 3.639 seconds. For reference, the velocity(t) of a Brownian particle for a short-time range is shown in (c) of Fig. 4.3. From the measurement, the root mean square velocity $v_{\text{RMS}} = \sqrt{\overline{v^2(t)}} \sim 2 \times 10^2 \mu$m/s, whereas $\sqrt{\langle v^2 \rangle}_{\text{eq}} := \sqrt{k_{\text{B}}T/m} \simeq 2.4 \times 10^2 \mu$m/s, from the equipartition law in equilibrium (cf. Appendix B). (m is the mass of a particle.)

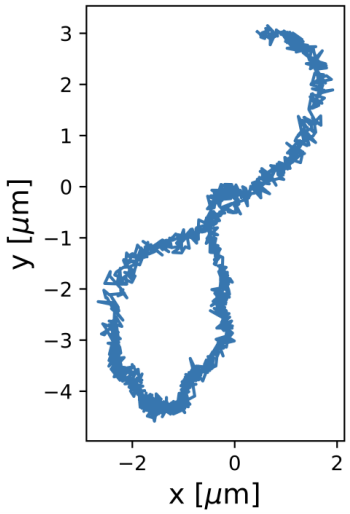

(a) Trajectory for 0.500 s (300Hz, $150V_{eff}$)

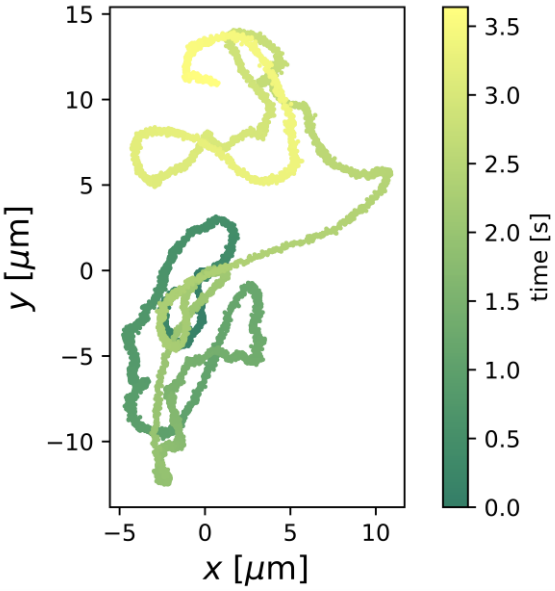

(b) Trajectory for 3.639 s (300Hz, $150V_{eff}$)

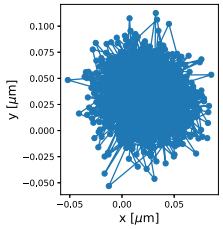

(c) Trajectory of a Brownian particle for 0.500s

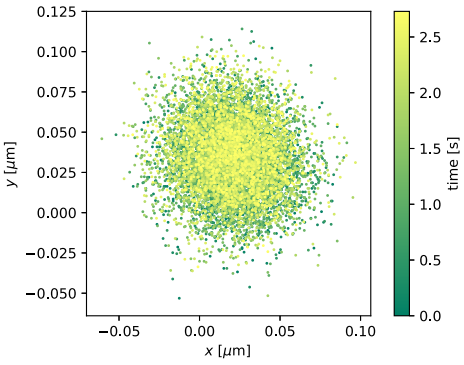

(d) Trajectory of a Brownian particle

Figure 4.2: Typical trajectories of the Quincke roller under AC and a Brownian motion ((a)(c): short-time, (b)(d): full-time length)

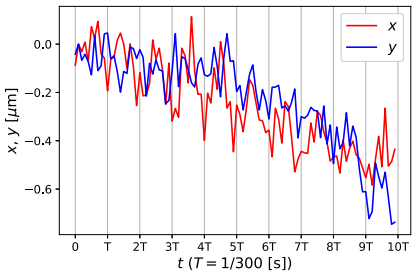

(a) $x(t)$, $y(t)$ (300Hz, 150V_{eff})

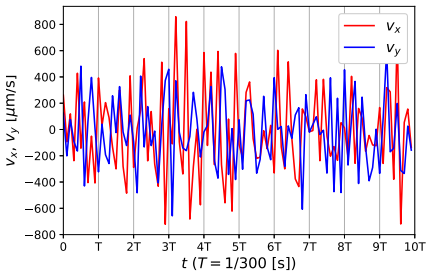

(b) $v_x(t)$, $v_y(t)$ (300Hz, 150V_{eff})

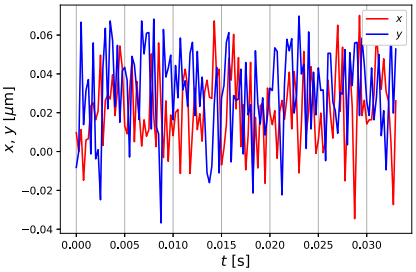

(c) For reference: $x(t)$, $y(t)$ of the Brownian particle

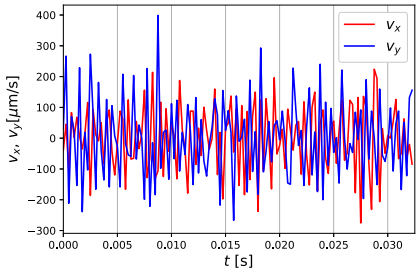

(d) For reference: $v_x(t)$, $v_y(t)$ of the Brownian particle

Figure 4.3: Positional and velocity changes (300Hz, 150V_{eff} and Brownian)

Power spectrum of the velocity In (a) of Fig. 4.3, the apparent periodicity is not observed. To investigate the velocity more, the power spectrum of the velocity time series is calculated along both x-axis and y-axis which are denoted as $S_{v_x v_x}$, $S_{v_y v_y}$, and shown in (a) of Fig. 4.4.[1] There is a peak at the external frequency f, so the periodicity in the velocity time series is observed.

To average the heterogeneity in x and y, "the velocity amplitude" which is the square root of the sum of normalised power in Fig. 4.4 is depicted in Fig. 4.5.

In (a) of Fig. 4.4 and Fig. 4.5, there is no peak at higher harmonics.

Moreover, small peaks are observed in the low frequency region (<10Hz) presented in (b) of Fig. 4.4, which corresponds the slow persistent motion of $\sim 0.1 - 1$s. Though these peaks are smaller than noisy components in high frequencies, they do not seems to be noises because there is the trend of larger noise in higher frequencies. In addition, the frequencies and magnitudes of these peaks can deviate slightly in the range 0∼10Hz by changing the data length unlike the peak at f.

These low frequency peaks were observed in more than ten samples including non-isolated particles. In these samples, the frequencies and magnitudes of these peaks were different in samples and data lengths, though the low frequency regions having peaks were approximately same.

It is not trivial based on the following facts. The translational diffusion only bears the constant baseline of the spectrum. If there is a DC velocity, the peak at 0Hz appears. This phenomena will be considered more in Section 4.5.

For the comparison to the Brownian motion, the velocity power spectrum of the Brownian particle is shown in Fig. 4.6. There is no peak, and there is the tendency of larger noise in higher frequency similarly to the Quincke particle. The spectra increase as the frequency increases. It is because the particle sticked to the substrate, because the velocity power spectrum of a Brownian motion in a harmonic potential is proportional to $\frac{\omega^2}{\omega^2+\omega_0^2}$, where ω, ω_0 is the angular frequency and $\omega_0 = k/\gamma$: the ratio of the spring constant k and the damping factor γ. (b) of Fig. 4.6 shows that there is no peak in low frequency region whereas the spectra of the AC roller in Fig. 4.4 had such peaks.

[1] The accuracy of the frequency axis ∼0.3Hz.

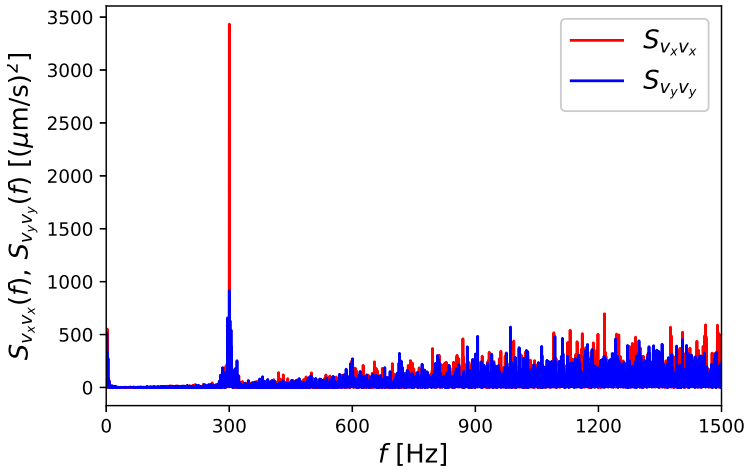

(a) Typical power spectrum (calculated using the time series for 3.639 s)

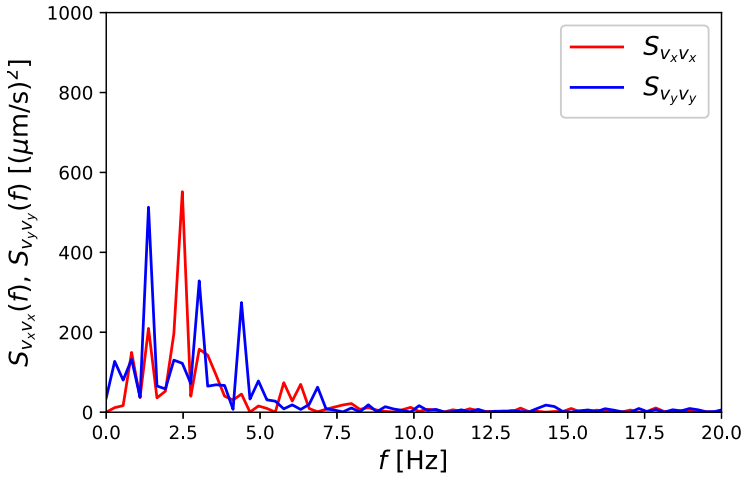

(b) The close view in the low frequency region

Figure 4.4: Power spectra of $v_x(t), v_y(t)$ (300Hz, 150V$_{\text{eff}}$)

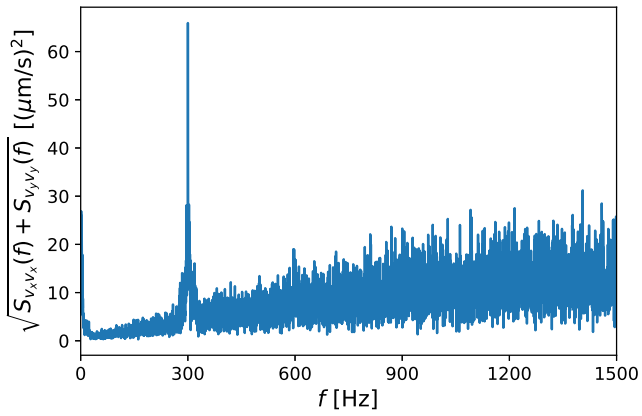

Figure 4.5: Velocity amplitude (300Hz, V_{eff})

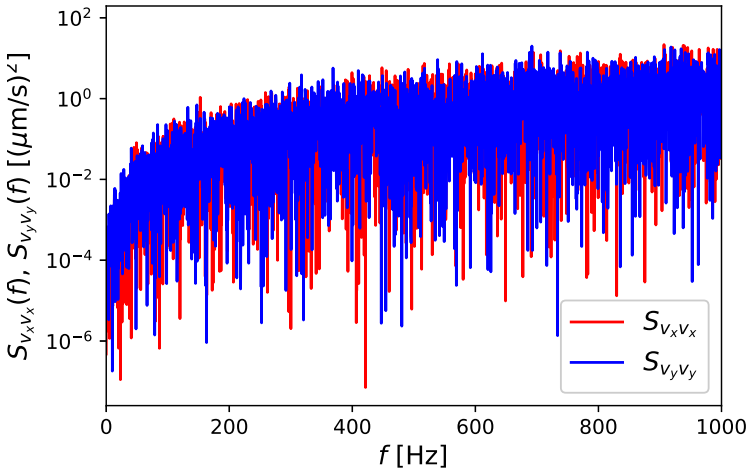

(a) Power spectrum $v_x(t), v_y(t)$ (a Brownian particle in the Quincke cell)

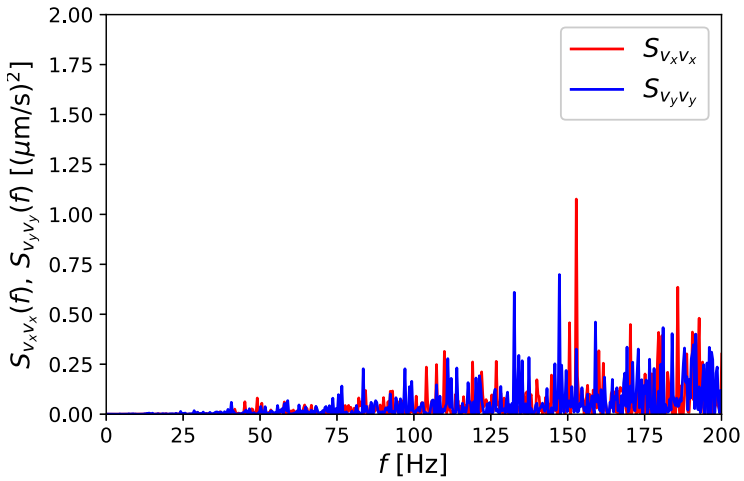

(b) The close view in the low frequency region

Figure 4.6: Power spectra of $v_x(t), v_y(t)$ (No electric field was applied)

On the other hand, the power spectrum of the speed time series $|\boldsymbol{v}(t)|$ shown in Fig. 4.7 has no peak at the external frequency f (=300Hz). Therefore, it means the directional changes tend to be periodic. The reason why the speed periodicity cannot be observed is supposed to be the low accuracy of the speed due to the high-speed capturing.

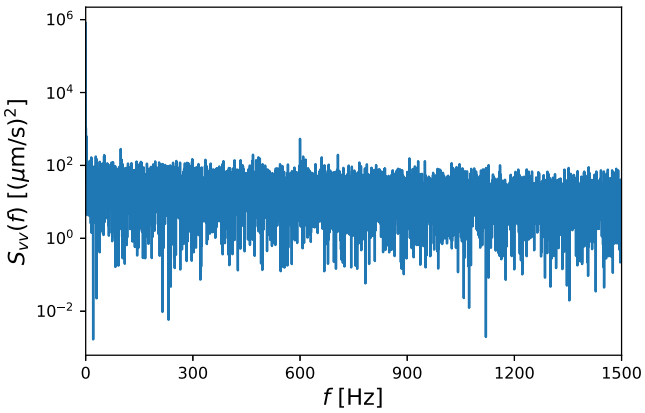

Figure 4.7: Power spectrum of $|\boldsymbol{v}(t)|$ (300Hz, 150V_{eff})

More directly, the angle change after a half period is worth calculating. Here, define the k-th half period displacement vector $\Delta\boldsymbol{d}(k) \equiv \boldsymbol{x}(t_0 + \frac{k}{2}T) - \boldsymbol{x}(t_0 + \frac{k-1}{2}T)$, where the initial time t_0 was set the value satisfies $0 \leq t_0 < \frac{T}{2}$ and gave the largest $|\Delta\boldsymbol{d}(k)|$ on average over k by the measurement. The angle between $\Delta\boldsymbol{d}(k)$ and the subsequent vector $\Delta\boldsymbol{d}(k+1)$ for every $k = 1, 2, \ldots$ is denoted by $\Delta\theta$. The histogram of angle changes after a half period $\Delta\theta$ is shown in Fig. 4.8. The typical angle change $\Delta\theta = \pi$, which means that the directional reversal tend to occur. The persistent index which is defined by the ensemble average of its cosine is $\langle \cos\Delta\theta \rangle \simeq -0.5$, which is larger than -1 in perfect reversal. In summary, the Quincke roller under AC field tend to reciprocate at the frequency of the external field.

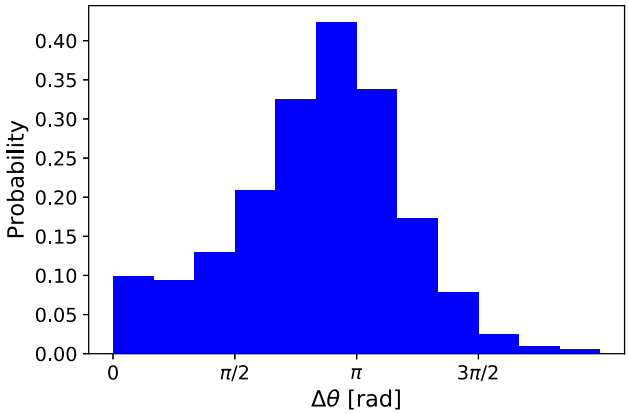

Figure 4.8: Histogram of angle changes after a half period $\Delta\theta$ (300Hz, 150V_{eff})

Let us consider another particle (denoted as "particle 2") which existed 177-198μm away from the particle analysed above (denoted as "particle 1") in the whole observation time. Each velocity correlation is shown in Fig. 4.9. It is remarkable that they were not clustered apparently. (a) of Fig. 4.9 shows the particle 2 moved periodically as well as particle 1. The particle 2 has also low frequency peaks as shown in (b) of Fig. 4.9. However, the peaks do not coincide with those of the particle 1, though the frequency ranges of the peaks are approximately same. It means that the two particles apart were not globally vibrated, which might have caused the low frequency peaks correspondent with the long-time persistent motion.

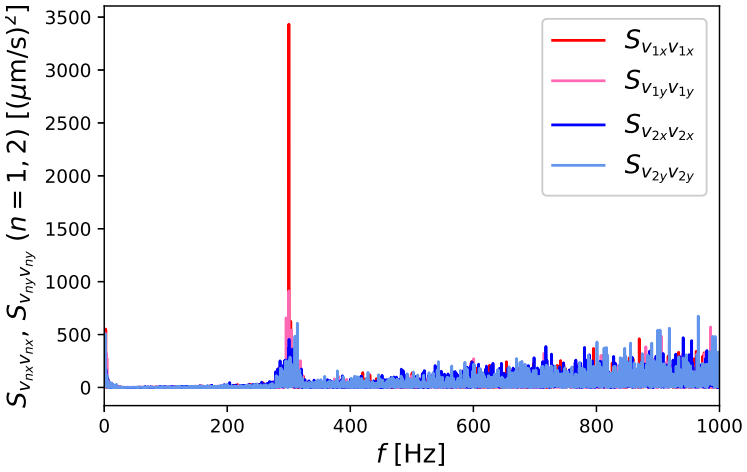

(a) Wide range of frequencies

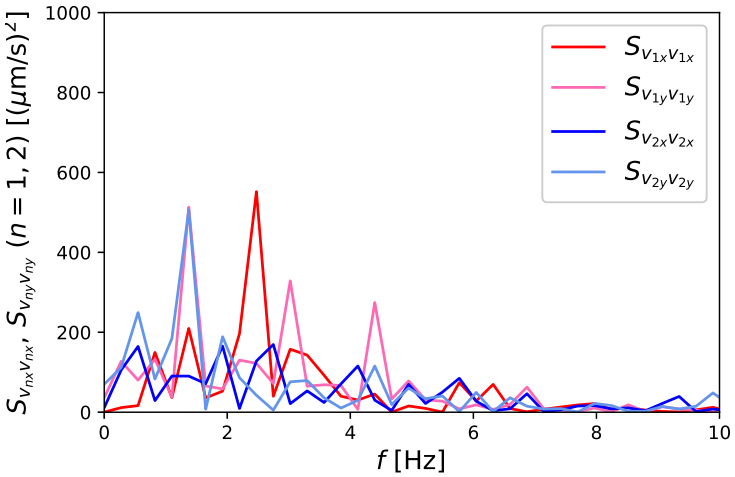

(b) The close view in the low frequency region

Figure 4.9: Power spectra of $v_{nx}(t), v_{ny}(t)$ $(n = 1, 2)$ (Particle 1 and 2 are not clustered.)

4.2.2 Estimation of the effective rotational diffusion coefficient D_θ

The reciprocating motion that was observed in the last subsection was not perfect. To investigate the axis changes of the reciprocating motion, the effective rotational diffusion constant is calculated. The velocity autocorrelations $\overline{\boldsymbol{v}(t+\tau)\cdot\boldsymbol{v}(t)}$ of three samples are shown in Fig. 4.10, where the overline indicates that the average was taken for t. The figure indicates that the correlation quickly decay but have peaks at the integer multiples of the period.[2]

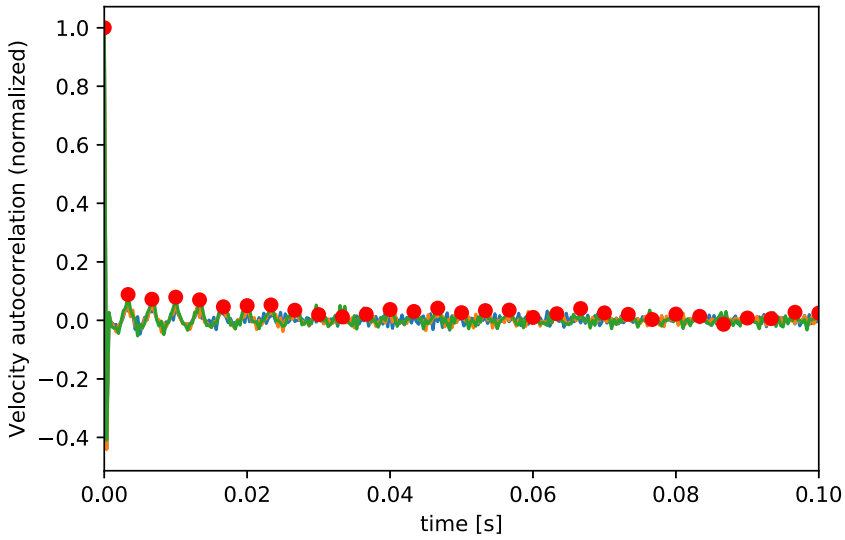

Figure 4.10: Velocity autocorrelation $\overline{\boldsymbol{v}(t+\tau)\cdot\boldsymbol{v}(t)}$ for AC 300Hz, 150V_{eff} (three samples) For the green line, the integer multiples of the period (=multiples of 1/300 s) are plotted by red points.

To estimate the rotational diffusion, the absolute values of the correlations at the integer multiples of the period $\tau = 0, T, 2T, \ldots$ are displayed in Fig. 4.11 which is needed for an exponential fitting. The correlation is averaged over three different particles.

It decays fast in short time around 0.1 seconds and then decrease slowly, so the exponent of the fast decay is obtained by the linear fitting to the semilog plot Fig. 4.11 as $D_\theta \simeq 3\times 10^2 \text{s}^{-1}$ ($D_\theta^{-1} \simeq$0.03s)[3] The time scale of the angular changes is smaller than 0.3 seconds which was obtained for DC rollers in [8]. Similarly to the DC case, it is much faster than that of thermal rotational diffusion in equilibrium ($D_\theta^{-1} \sim 2\times 10^2$ s).

[2]The reason why it decay so quickly is that the correlations between the same value ($\tau = 0$) and between different values ($\tau \neq 0$) make a serious difference for noisy signals.

[3]The fitting was executed to the time interval $[0, 0.1]$.

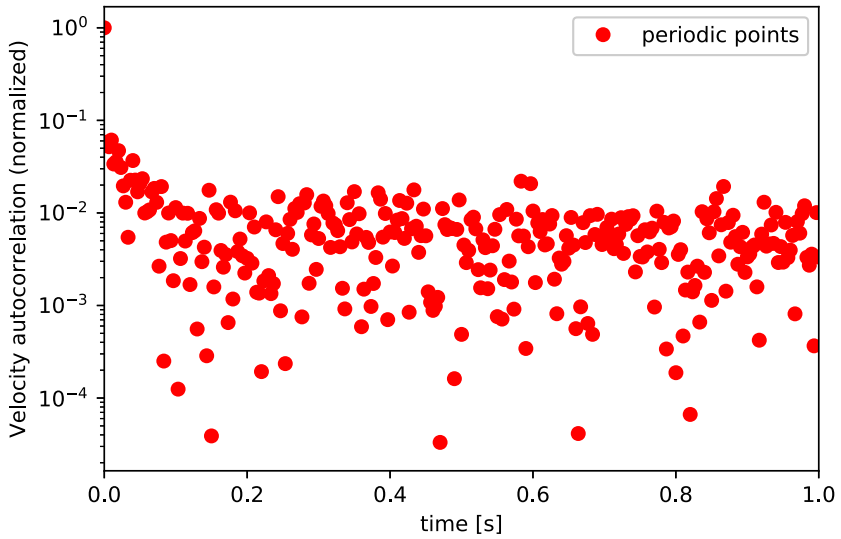

Figure 4.11: Velocity autocorrelation $\overline{\boldsymbol{v}(t+\tau)\cdot\boldsymbol{v}(t)}$ plotted for only $\tau = nT$ (AC 300Hz, $150\mathrm{V}_{\mathrm{eff}}$, ensemble average of three particles)

4.2.3 Mean square displacement

To characterise the dynamics of the Quincke roller, the mean square displacement (MSD) is calculated and shown in Fig. 4.12 comparing to that of the Brownian particle which experimentally acquired and shown in Subsection 4.2.1.

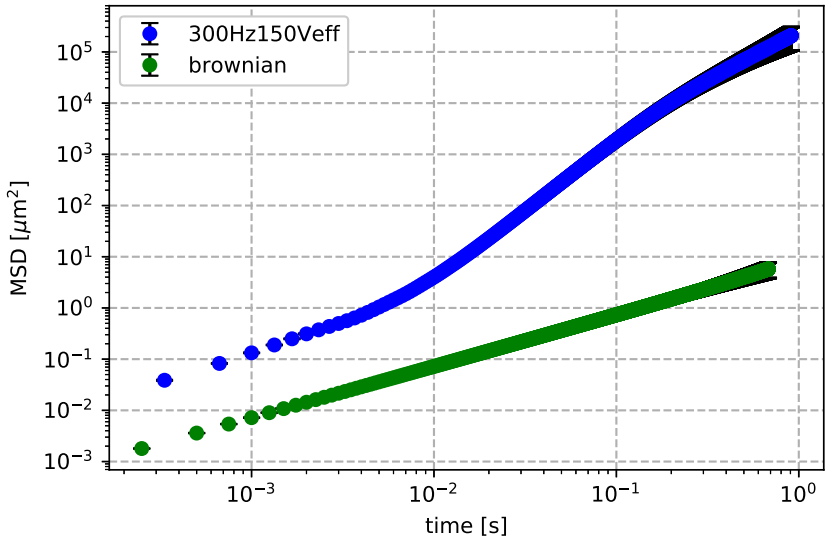

Figure 4.12: MSD for AC 300Hz, 150V_{eff} (averaged for three samples) and a Brownian particle (one particle). (Time is until one forth of whole time series. 1 error bar = 1 standard error.)

The Brownian particle is diffusive (MSD(τ) $\propto \tau$) as is well known. The translational diffusion coefficient is $D \sim 2\mu\text{m}^2/\text{s}$ from the slope. This translational diffusion coefficient D is larger than the value calculated by the fluctuation and dissipation theorem in equilibrium (See Appendix B.), which was probably caused by the sticking of the particle and the substrate. In contrast, the Quincke particle is diffusive in small-time scale, then the exponent increases and then decreases.

To clarify the exponent of the MSD, the exponent $\beta(\tau)$ of MSD(τ)$\propto \tau^{\beta}$ is calculated by

$$\beta(\tau) \equiv \frac{\mathrm{d}(\log \mathrm{MSD}(\tau))}{\mathrm{d}(\log \tau)} \tag{4.1}$$

and shown in Fig. 4.13. The left and right figures of Fig. 4.13 show the long-time and short-time behaviour of the exponent. (The different colours mean different particles.) One of the striking features is that the exponent grows dramatically around 10 periods and the maximum exponent is over 2, which means superballistic. This anomalous behaviour is not understood easily, so it will be discussed in Section 4.5. Another feature is that there is the periodicity in the exponent, which the right figure shows. The exponent in the long-time region obtained is still ballistic. It might be because the observation time is too small to the appearance of the diffusive region.

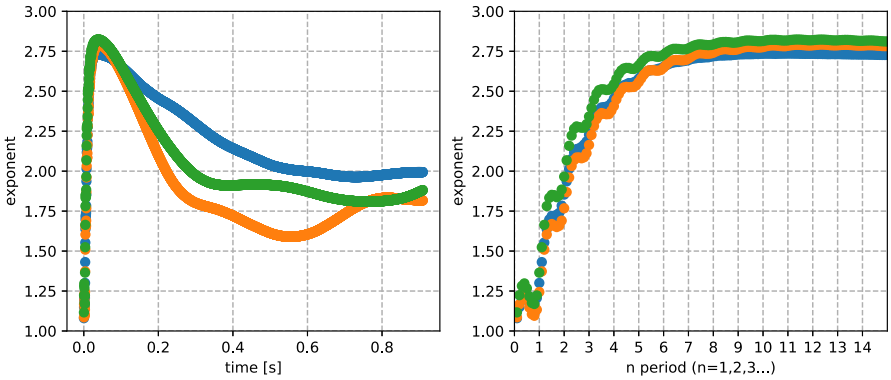

Figure 4.13: The exponent $\beta(\tau)$ of MSD$(\tau) \propto \tau^{\beta}$ for AC 300Hz, 150V$_{\text{eff}}$. (Three samples are plotted.) left: long-time behaviour, right: short-time behaviour

4.2.4 Summary and discussion of the experimental results

In this section, the motion of a single Quincke roller under the fixed voltage (300Hz, 150V$_{\text{eff}}$) is analysed. It reciprocates at the frequency of the external field with noisy components in high frequencies and small peaks at low frequencies. The directional reversal tends to occur every half period, and the directional axis changes at $\sim$ 0.03s which is approximately 10 times of the period. The exponent of the MSD grows periodically from diffusive and reaches a peak which is superballistic then decreases.

4.3 Generalised model on the dynamics of one Quincke roller under the AC field

In the above sections in this chapter, the behaviours of the Quincke roller under the AC field experimentally were notated. To understand the behaviour quantitatively, the model of the Quincke roller explained in Chapter 2 is generalised to the AC regime in this section.

For the beginning, $\boldsymbol{E}_0$ is substituted to $\boldsymbol{E}_0 \cos \omega t$ in the equation Eq. (2.21). Decompose Eq. (2.21) into z and parallel components. Then, decompose the polarisations into the instantaneous part and the surface part by

$$P_{\parallel}(t) = P_{\parallel}^{\sigma}(t) + P_{\parallel}^{\epsilon}(t) \tag{4.2}$$
$$P_z(t) = P_z^{\epsilon}(t) + P_z^{\sigma}(t) \tag{4.3}$$

Here, $\boldsymbol{P}^{\epsilon}(t)$ is determined by the electric field the particle feels at time t instantaneously (dielectric polarisation):

$$P_z^{\epsilon}(t) = 4\pi\epsilon_0 a^3 \chi^{\infty} E_0 \cos \omega t \tag{4.4}$$
$$P_{\parallel}^{\epsilon}(t) = 0 \tag{4.5}$$

Conversion to dimensionless values Now nondimensionalisation are conducted by using the unit in Table. 2.1 as

$$A = \frac{\mu_r \varepsilon_l E_0^2 a^3}{D_\theta} \tag{4.6}$$
$$\tau_{\tilde{\mathrm{MW}}} = \tau_{\mathrm{MW}} D_\theta \tag{4.7}$$
$$\tilde{t} = D_\theta t \tag{4.8}$$
$$\tilde{P} = \frac{P}{\varepsilon_0 E_0 a^3} \tag{4.9}$$

Therefore, nondimensionalised equations are the followings (For brevity, the tilde is omitted.):

The equations of the polarisation with angular frequency ω

$$\begin{aligned} &\frac{\mathrm{d}P_z^{\sigma}}{\mathrm{d}t} + \frac{1}{\tau_{\mathrm{MW}}} P_z^{\sigma} + 4\pi\chi^{\infty} \frac{\mathrm{d}(\cos \omega t)}{\mathrm{d}t} + \frac{4\pi(\chi^{\infty} + 1/2)}{\tau_{\mathrm{MW}}} \cos \omega t \\ = \; & A P_{\parallel}^{\sigma 2} \cos \omega t \end{aligned} \tag{4.10}$$

$$\frac{\mathrm{d}P_{\parallel}^{\sigma}}{\mathrm{d}t} + \frac{1}{\tau_{\mathrm{MW}}} P_{\parallel}^{\sigma} = -A \cos \omega t P_z^{\sigma} P_{\parallel}^{\sigma} \tag{4.11}$$

By introducing a variable φ defined by $\frac{\mathrm{d}\varphi}{\mathrm{d}t} = \omega$ and $\varphi(0) = 0$, it can be seen as a three-dimensional autonomous dynamical system:

$$\frac{\mathrm{d}P_{\parallel}^{\sigma}}{\mathrm{d}t} = -\frac{1}{\tau_{\mathrm{MW}}} P_{\parallel}^{\sigma} - A \cos \varphi P_z^{\sigma} P_{\parallel}^{\sigma} \tag{4.12}$$

$$\frac{\mathrm{d}P_z^{\sigma}}{\mathrm{d}t} = -\frac{1}{\tau_{\mathrm{MW}}} P_z^{\sigma} - 4\pi\chi^{\infty}\omega \sin \varphi + \frac{4\pi(\chi^{\infty} + 1/2)}{\tau_{\mathrm{MW}}} \cos \varphi + A P_{\parallel}^{\sigma 2} \cos \varphi \tag{4.13}$$

The translation velocity (with dimension) expressed via values with dimension is

$$v(t) = -\frac{\epsilon_l}{\epsilon_0} a\tilde{\mu_t} E_0 \cos(\omega t) P_{\parallel}(t) \tag{4.14}$$

The translation velocity (with dimension) expressed using dimensionless values as Eq. (2.47) is

$$v(t) = -\frac{a\tilde{\mu_t}}{\mu_r \tau_{\rm MW}} \cdot \tilde{\tau_{\rm MW}} A \tilde{P_{\parallel}^{\sigma}} \cos(\omega t), \tag{4.15}$$

which is useful in numerical simulation.

4.4 Numerical results

4.4.1 Physical values used for the calculation

The parameters were set using the parameter list in Section 2.3 basically to compare our experimental results. It was assumed $\frac{a\tilde{\mu_t}}{\mu_r \tau_{\rm MW}} = 82.1\mu$m/s to draw the figure for the DC regime. This was assumed by the following reasons. First, this can be determined experimentally also in our system by DC experiments with a few voltages like in [8, 47] but independently to them. However, it is doubtful to correspond to the value under the AC field. Therefore, it is used an idea to approximate from only AC experimental data as follows: First, numerically, it was found that $v_{\rm RMS} := \sqrt{\overline{v(t)^2}}$ is proportional to the electric field (the effective voltage) as shown later in Fig. 4.20 with little dependency on frequencies. On the other hand, $v_{\rm RMS}$ can be calculated experimentally, so that the root mean square velocity coincides by tuning the coefficient $\frac{a\tilde{\mu_t}}{\mu_r \tau_{\rm MW}}$ in simulation.

Here $v_{\rm RMS} \sim 6 \times 10^2 \mu$m/s was set when the electric voltage is 300Hz and 150$V_{\rm eff}$, so that it is assumed $\frac{a\tilde{\mu_t}}{\mu_r \tau_{\rm MW}} = 82.1\mu$m/s globally[4].

4.4.2 Dynamics

Let us fix the amplitude of the voltage first. The dynamics $(P_{\parallel}^{\sigma}(t), P_z^{\sigma}(t))$ under several frequencies are shown in Fig. 4.14. $(P_{\parallel}^{\sigma}(t), P_z^{\sigma}(t))$ reach periodic states whose frequencies corresponds external frequencies,[5] though they include many higher harmonics. The initial value is set $(P_{\parallel}^{\sigma}(0), P_z^{\sigma}(0)) = (0.1, 0.1)$ (dimensionless values) to plot these figures. It is notable that $P_{\parallel}$ does not change its sign when time develops. Another remark is that the periodic state is invariant with changes in initial values except for the sign of $P_{\parallel}^{\sigma}(0)$.

[4]The DC element was eliminated from experimental $v_{\rm RMS}$, which does not affect the one significant figure.

[5]For this calculation, the time interval for numerical calculation is 100000-time steps for one period.

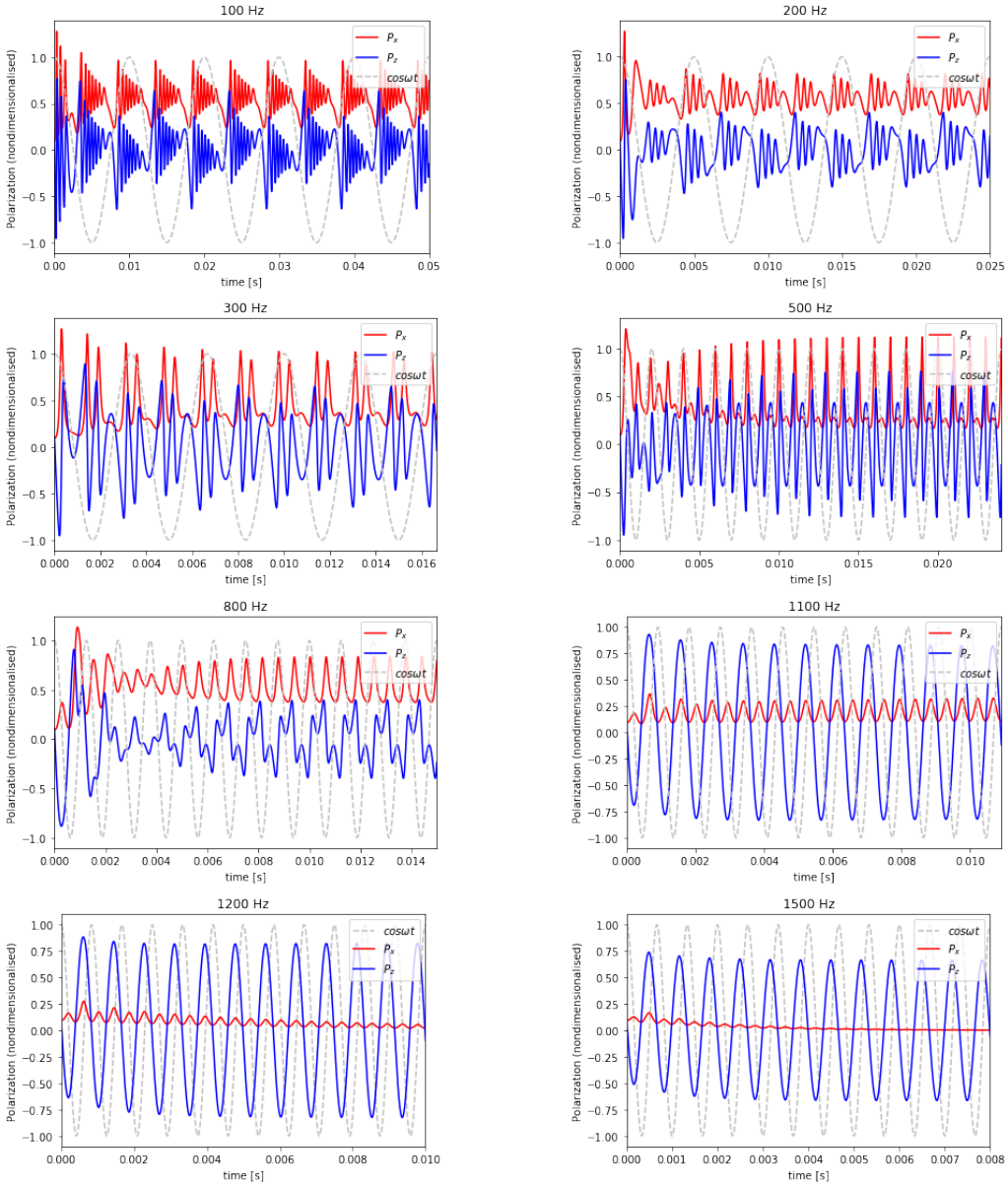

Figure 4.14: Time series of polarisation in each frequency

In order to observe the periodic states more clearly, $P_{\parallel}^{\sigma} P_{z}^{\sigma}-$ trajectories projected along $\varphi = \omega t$ are shown in Fig. 4.15. Here $(P_{\parallel}^{\sigma}(0), P_{z}^{\sigma}(0)) = (0.1, 0.1)$. In each frequency, the trajectory goes to the red closed loop that is correspondent to one period. Because a state relaxes to the frequency-dependent closed loop independent on initial states (aside from the sign of $P_{\parallel}^{\sigma}(0)$), the closed loop can be understood as the limit cycle. The limit cycle is symmetric to $P_{\parallel}^{\sigma}$ axis. For negative initial $P_{\parallel}^{\sigma}(0) < 0$, the limit cycles are the mirror symmetries of those for $P_{\parallel}^{\sigma}(0) > 0$ to P_z axis, which is similarly to the DC case. The limit cycles tend to be simpler as frequencies increase.

In high frequencies like 1200Hz and 1500Hz, the limit cycles (the red closed loops in Fig. 4.15) do not have finite $P_{\parallel}^{\sigma}$ component. It is because the time scale of external frequencies are comparable to that of Maxwell-Wagner polarisation so that the field reversal occurs before interfacial charges rearrange, which causes no motion.

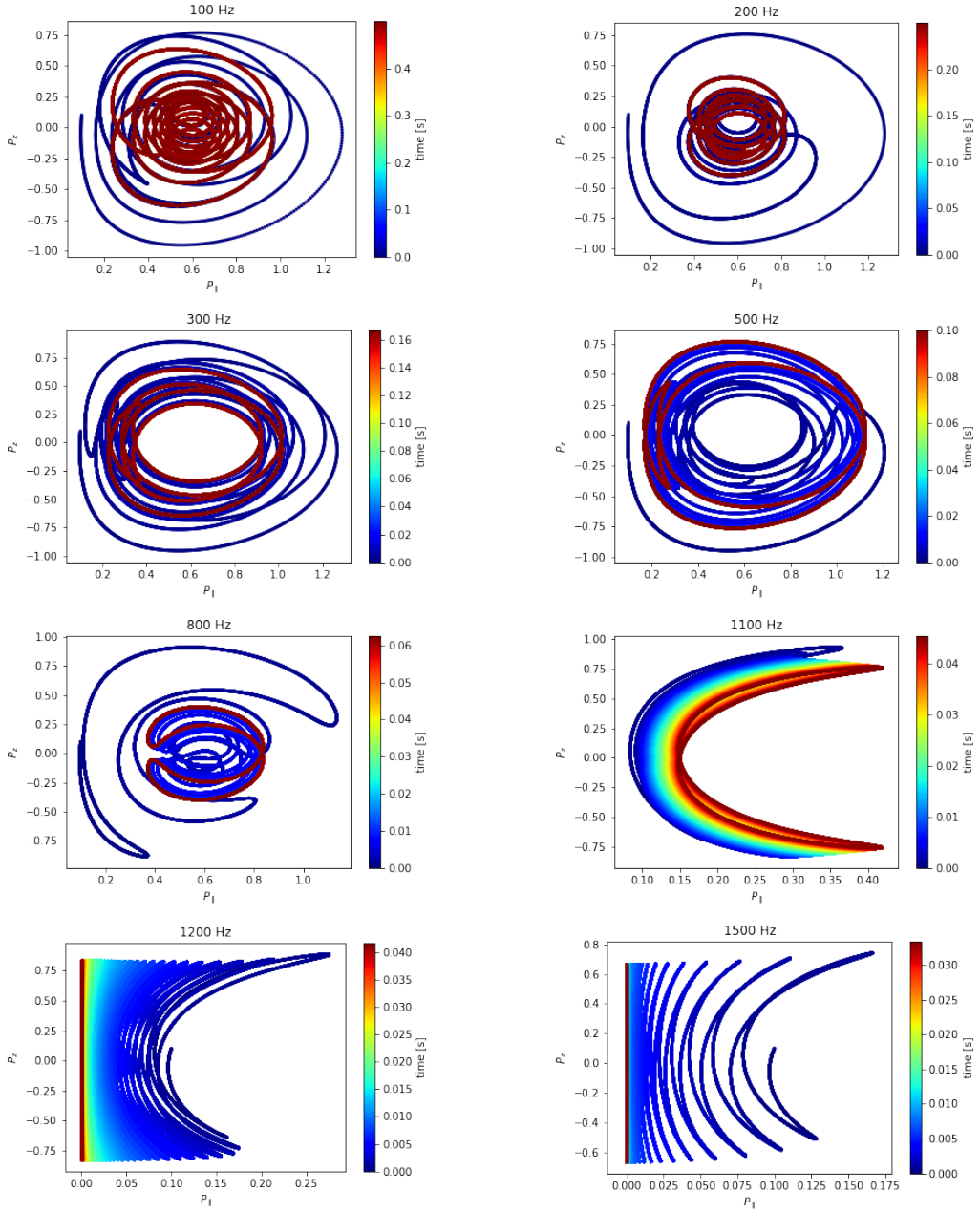

Figure 4.15: $P_{\parallel}^{\sigma} P_z^{\sigma}-$ trajectory in each frequency

Velocity and position By using Eq. (4.14) or Eq. (4.15), the velocity and position were obtained as a function of time t as shown in Fig. 4.16. This figure shows that the velocity periodically changes and the particle reciprocates at the frequency of the external field. In high frequencies in Fig. 4.17, the particle becomes stationary in the periodic state, as expected from having zero $P_{\parallel}^{\sigma}$ in Fig. 4.15.

Therefore, as illustrated in Fig. 4.18, a particle reciprocates but the parallel component of polarisation $P_{\parallel}(= P_{\parallel}^{\sigma})$ do not alter its sign even in the periodic state.

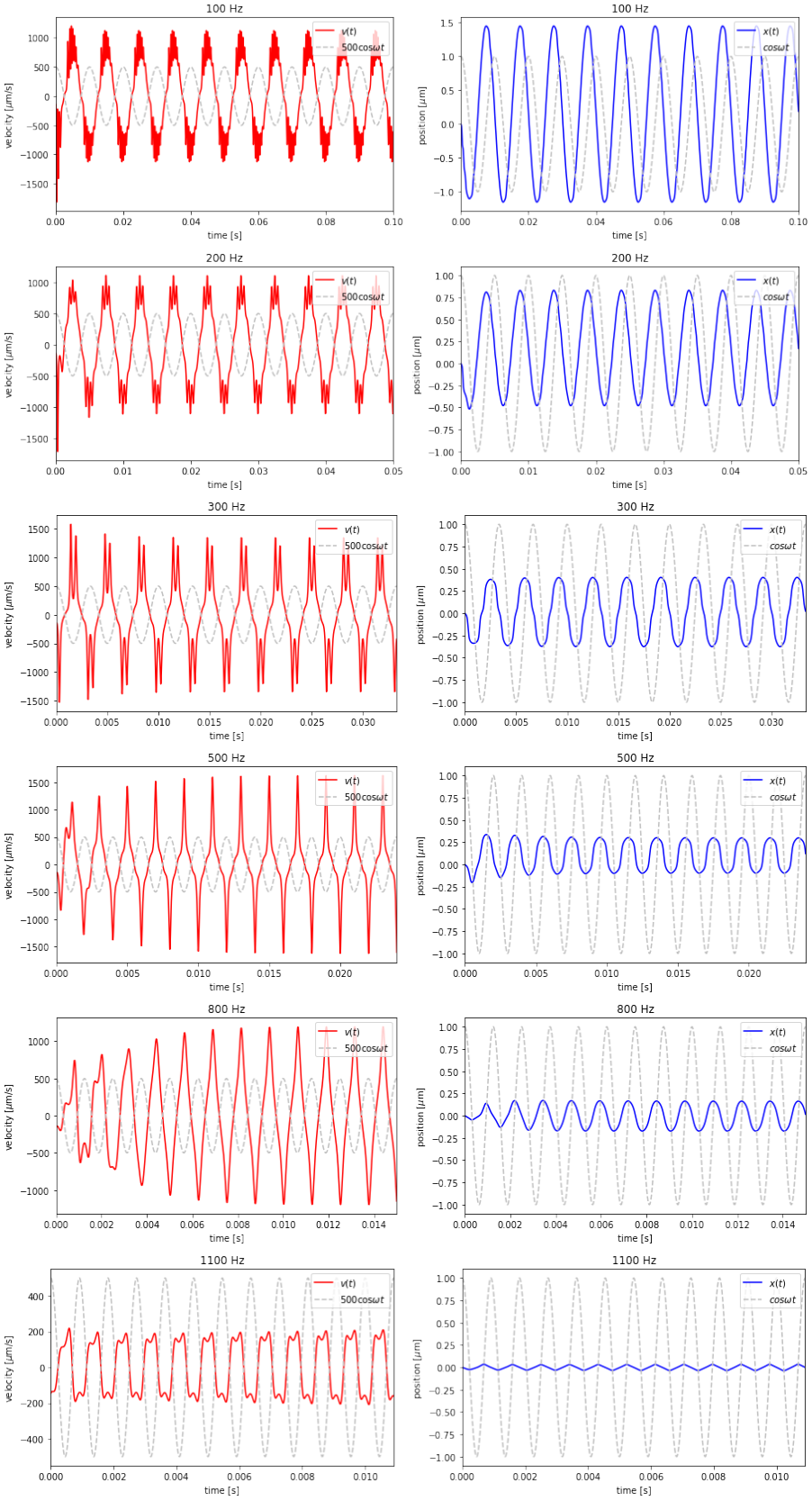

Figure 4.16: Velocity and position in each frequency

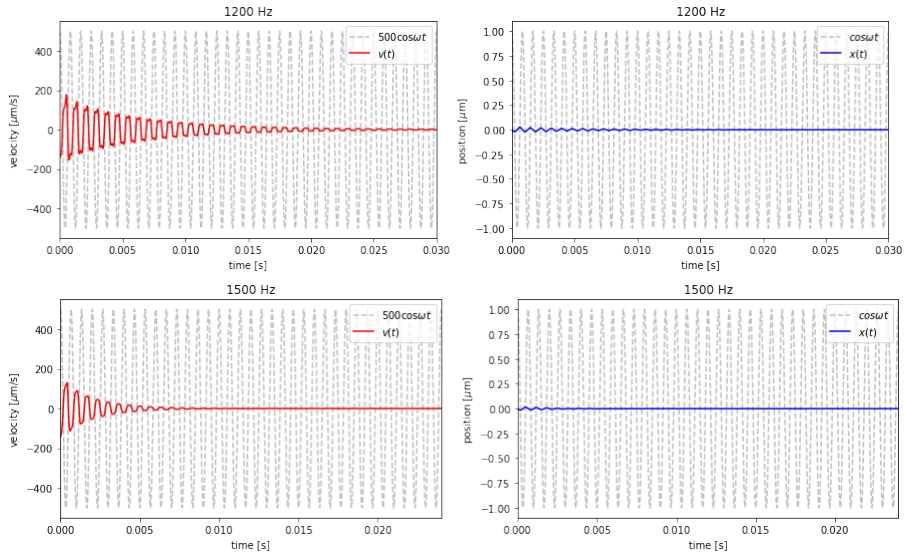

Figure 4.17: Velocity and position in each frequency in high frequencies

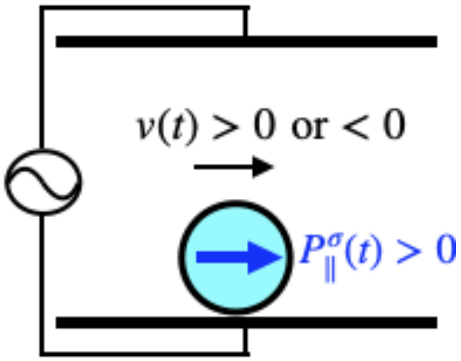

Figure 4.18: $P_{\parallel}^{\sigma}$ does not change its sign, but $v(t)$ does. (figure for $P_{\parallel}(0) > 0$)

4.4.3 Parameter dependency

Here the frequency dependencies of the reciprocating amplitude and the root mean square velocity $v_{\mathrm{RMS}} := \sqrt{\overline{v(t)^2}}$ averaged only in the periodic states after transient states are argued and presented in Fig. 4.19. (from 50 to 1090Hz, every 10Hz)

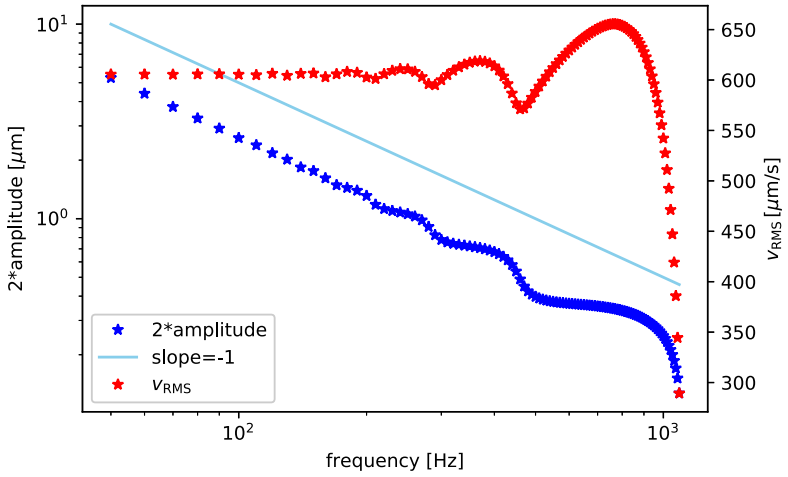

Figure 4.19: Frequency dependency of reciprocating amplitude and velocity v_{RMS} after transient states (calculated every 10Hz)

First, the amplitude of reciprocating motion in periodic states is approximately proportional to the inverse of frequency. This relationship occurs when the velocity is sinusoidal.

Secondly, the root mean square of velocity v_{RMS} is almost constant for small frequencies but fluctuate in intermediate frequencies. In high frequency, the v_{RMS} drops.[6]

Until now, only the frequency of the electric field are changed. Let us briefly argue the amplitude of electric voltage dependency.

Unlike in the DC case, the relationship between the amplitude of electric voltage (or effective voltage of alternative current V_{eff} $(=\frac{V_{\mathrm{pp}}}{2\sqrt{2}})$) and the propelling velocity is not given a single equation like Eq. 2.39. Therefore, the propelling velocity-related value which is one-to-one correspondent with V_{eff} should be clarified numerically.

Then it is found that v_{RMS} is proportional to effective voltage V_{eff} for the range of frequencies from 50 to 350Hz which includes the parameters in the later experiment as shown in Fig. 4.20, although other values such as 2×amplitude and the peak-to-peak velocity v_{pp} fail to have one-to-one correspondence as depicted in Fig. 4.21.

[6]The real transition frequency is over 1090Hz (around 1130Hz). Because the relaxation time to periodic states become longer, the frequency range was limited here to calculate amplitude and v_{RMS} in periodic states.

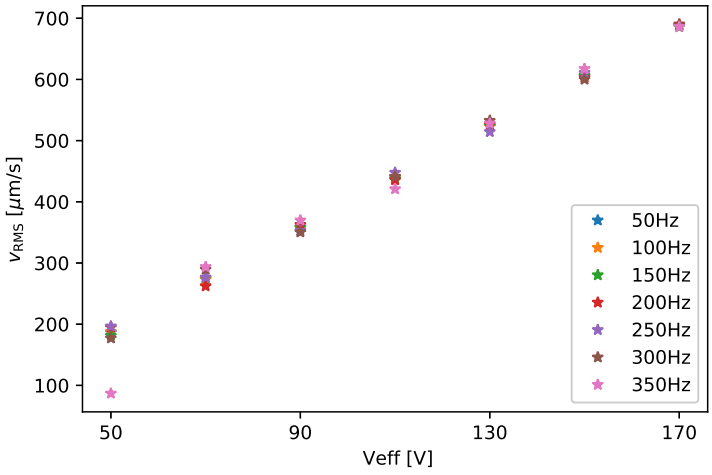

Figure 4.20: v_{RMS} is proportional to effective voltage V_{eff}.

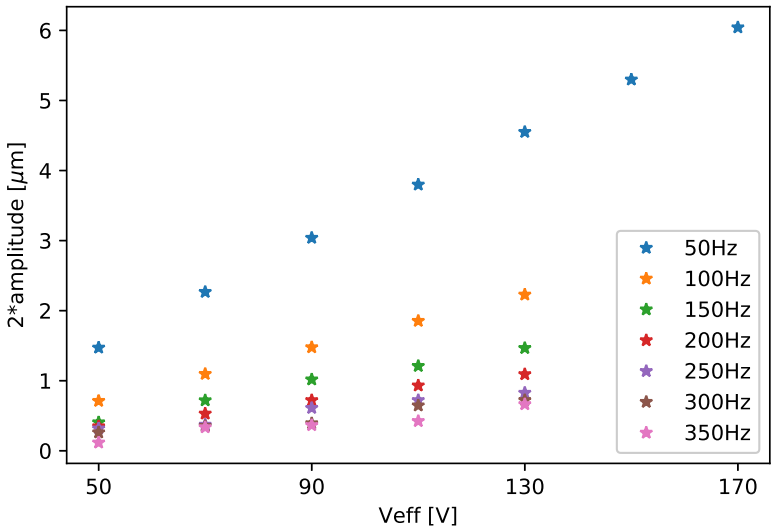

(a) 2×amplitude vs V_{eff}

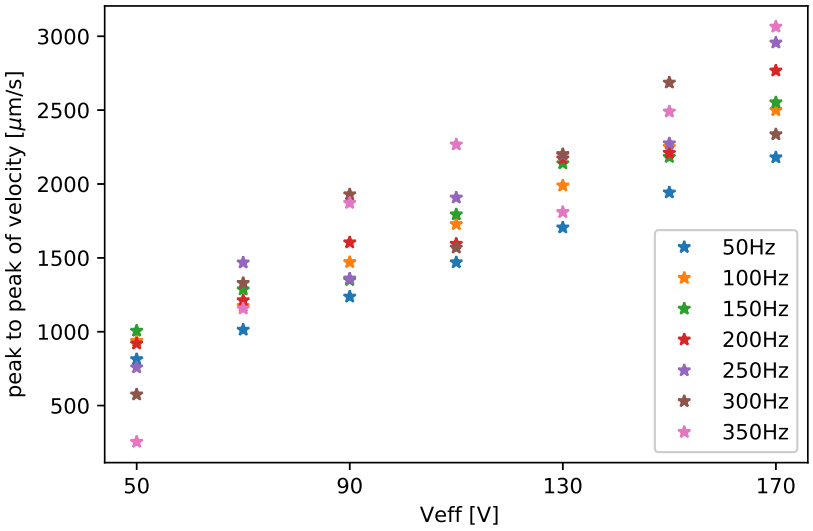

(b) Peak-to-peak velocity v_{pp} vs V_{eff}

Figure 4.21: Exploration for one-to-one corespondent values with V_{eff}

4.4.4 Properties of power spectrum

In the periodic states, the polarisations and velocities include higher harmonics. Here the power spectra of $P_{\parallel}^{\sigma}(t)$, $P_z(t)$ and $v(t)$ are calculated as shown in Fig. 4.22.

In periodic states, $P_{\parallel}^{\sigma}$ only has even harmonics including the DC component, while P_z has only odd harmonics. Thus, the velocity which is determined by Eq. (4.14) only has odd harmonics, which means no net motion in this one-dimensional dynamics.

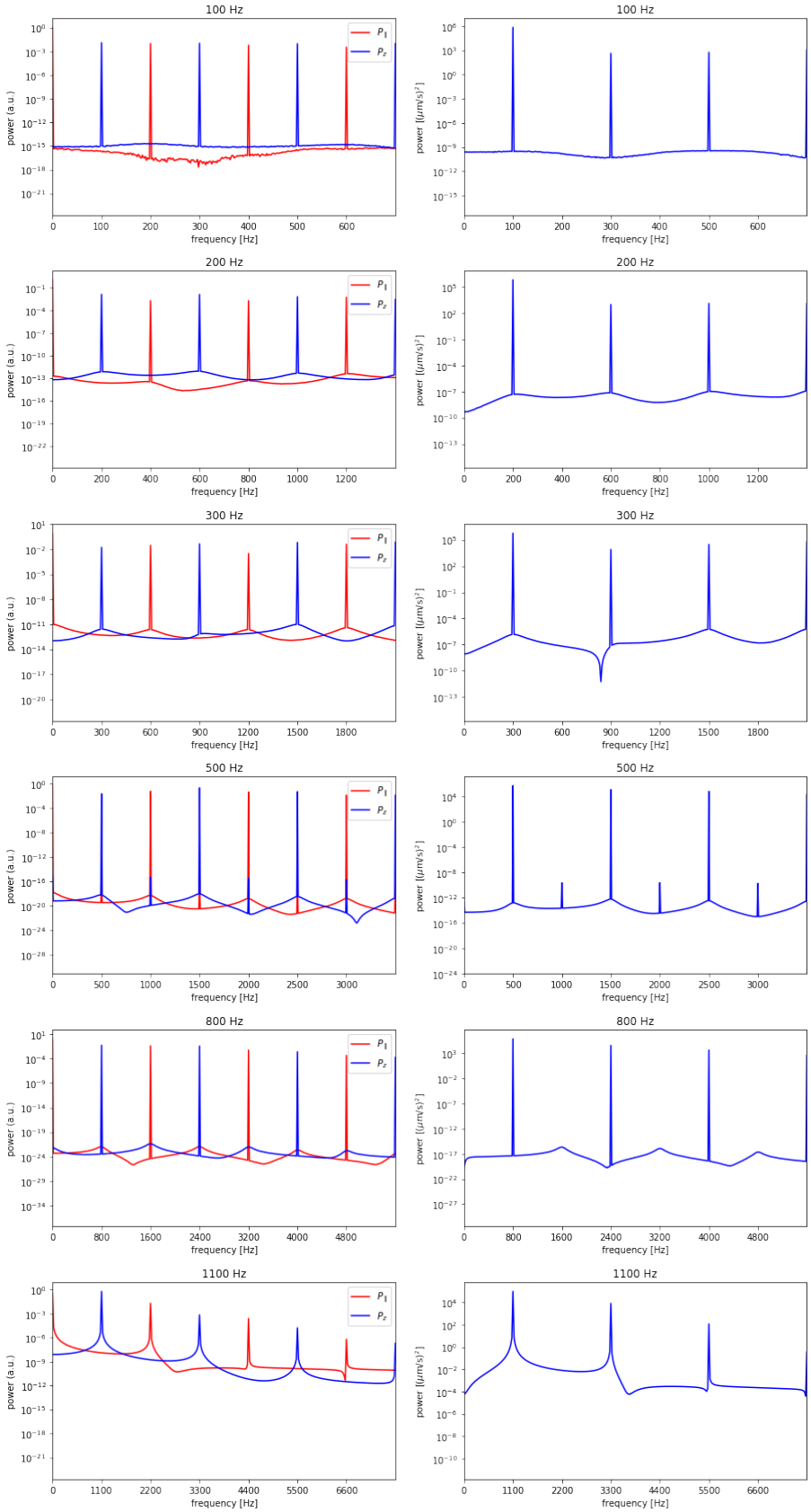

Figure 4.22: Power spectra of polarisation (left column) and velocity (right column) in each frequency

4.4.5 Method for obtaining Lyapunov exponents numerically

To check whether the dynamics go to limit cycles at all frequencies or not, the Lyapunov exponents was calculated. Here the method for obtaining Lyapunov exponents are explained, and the result is shown in the next subsection.

To derive Lyapunov exponents, the differential equations of the polarisation Eq. (C.9) and Eq. (C.10) were solved with the time evolution of the vectors in tangent space which is explained in the following.

For a dynamical system $\dot{\boldsymbol{x}} = \boldsymbol{F}(\boldsymbol{x})$, a variation from the orbit $\boldsymbol{u}$ follows this equation:

$$\dot{\boldsymbol{u}} = \frac{\partial \boldsymbol{F}}{\partial \boldsymbol{x}}(T^t \boldsymbol{x}_0)\boldsymbol{u} \tag{4.16}$$

where T^t satisfies $\boldsymbol{x}(t) = T^t \boldsymbol{x}_0$. $\boldsymbol{x}_0$ is the initial state.

Here, a vector $\boldsymbol{x}$ is set to

$$\boldsymbol{x} = \begin{pmatrix} P_\parallel^\sigma \\ P_z^\sigma \\ \varphi \end{pmatrix}. \tag{4.17}$$

The equation of the tangent space Eq. (4.4.5) can be written as

$$\dot{\boldsymbol{u}} = \begin{pmatrix} -1/\tau_{\mathrm{MW}} - AP_z^\sigma \cos\varphi & -AP_\parallel^\sigma \cos\varphi & AP_\parallel^\sigma P_z^\sigma \sin\varphi \\ 2AP_\parallel^\sigma \cos\varphi & -1/\tau_{\mathrm{MW}} & 4\pi\chi^\infty\omega\cos\varphi + \frac{4\pi(\chi^\infty+1/2)}{\tau_{\mathrm{MW}}}\sin\varphi - AP_\parallel^{\sigma\,2}\sin\varphi \\ 0 & 0 & 0 \end{pmatrix} \boldsymbol{u} \tag{4.18}$$

φ is marginally stable, so one of the Lyapunov exponent is zero. Therefore $\boldsymbol{u}$ is considered as a two-dimensional vector from now. The vector set $\{\boldsymbol{e}_i(t)\}$ $(i = 1, 2)$ evolve with

$$\dot{\boldsymbol{u}} = \begin{pmatrix} -1/\tau_{\mathrm{MW}} - AP_z^\sigma \cos\varphi & -AP_\parallel^\sigma \cos\varphi \\ 2AP_\parallel^\sigma \cos\varphi & -1/\tau_{\mathrm{MW}} \end{pmatrix} \boldsymbol{u}, \tag{4.19}$$

where $\boldsymbol{u}$ is redefined as a 2×1 vector.

Numerical calculation of Lyapunov exponents by the Shimada-Nagashima method
The Shimada-Nagashima method is a numerical method to calculate Lyapunov exponents. In this method, whole time length is divided into the time intervals of time length τ (Here $\tau = 2\pi/\omega$). Consider the time evolution of the ordinary differential equation and the differential equations for the tangential space which explained above. The initial orthonormal vector can be set the orthonormal vector set $\{\boldsymbol{e}_1(0)\ , \boldsymbol{e}_2(0)\}$= {(1,0), (0,1)} whose choice is arbitrary. Then the orthonormal vector set evolves from $t = 0$ to τ. $\boldsymbol{e}_1(\tau)$ and $\boldsymbol{e}_2(\tau)$ might shrink or expand with changing their directions. Then, the Gram-Schmidt orthonormalisation:

$$\boldsymbol{e}_1'(\tau) = \frac{\boldsymbol{e}_1(\tau)}{\|\boldsymbol{e}_1(\tau)\|} \tag{4.20}$$

$$\boldsymbol{e}_2'(\tau) = \frac{\boldsymbol{e}_2(\tau) - (\boldsymbol{e}_2(\tau)\cdot\boldsymbol{e}_1'(\tau))\boldsymbol{e}_1'(\tau)}{\|\boldsymbol{e}_2(\tau) - (\boldsymbol{e}_2(\tau)\cdot\boldsymbol{e}_1'(\tau))\boldsymbol{e}_1'(\tau)\|} \tag{4.21}$$

are performed, so that the new orthonormal set $\{\boldsymbol{e}_1'(\tau), \boldsymbol{e}_2'(\tau)\}$ is prepared. This is the first step.

As the second step or later (j-th step, $j = 2, 3, 4...$), the initial state is inherited from the final state of the step before ($P_{\parallel}^{\sigma}((j-1)\tau), P_{z}^{\sigma}((j-1)\tau)$), but the initial orthonormal vector set is the new orthonormal vector set $\{\boldsymbol{e}_1'((j-1)\tau), \boldsymbol{e}_2'((j-1)\tau)\}$. Then the state and the new vector set evolve with time length τ. The last vector set is denoted $\{\boldsymbol{e}_1(j\tau), \boldsymbol{e}_2(j\tau)\}$ which is not orthogonal nor normal in general. This set of vectors is used for the initial set of the next $(j+1)$-th step after the Gram-Schmidt orthonormalisation.

In this way, $\boldsymbol{e}_i(j\tau)$ is obtained, so that the Lyapunov exponents λ_i ($\lambda_1 \geq \lambda_2 \geq ...$) are calculated via

$$\lambda_i = \lim_{n\to\infty} \frac{1}{n\tau} \sum_{j=1}^{n} \ln \|\boldsymbol{e}_i(j\tau)\|. \tag{4.22}$$

Practically, the exponent λ can be obtained by the value $\frac{1}{n\tau}\sum_{j=1}^{n} \ln \|\boldsymbol{e}_i(j\tau)\|$ saturated for n sufficiently large.

4.4.6 Lyapunov exponents

Here is the result for calculating the Lyapunov exponents. By introducing φ in Eqs. (4.12) and (4.13), one of the three Lyapunov exponents is zero by definition. Therefore, the problem is calculating the remaining two exponents.

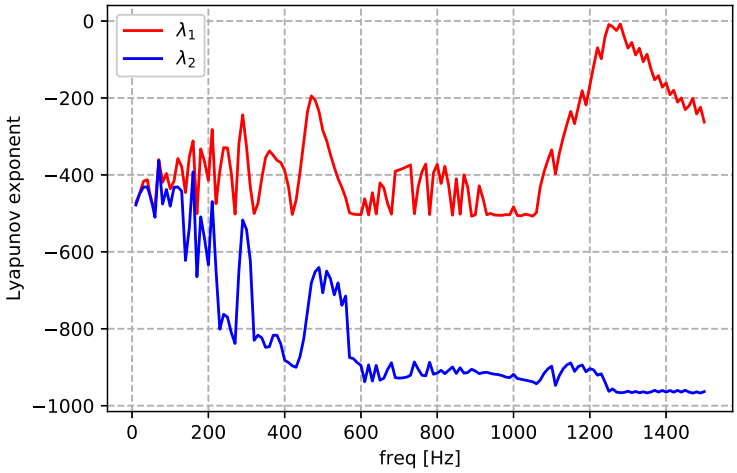

Figure 4.23: Lyapunov exponents $\left[\mathrm{s}^{-1}\right]$ ($V_{\mathrm{eff}} = 150\mathrm{V}$, calculated every 10Hz.)

The result for $V_{\mathrm{eff}} = 150\mathrm{V}$ ($E_0 = 7.07 \times 10^6 \mathrm{V/m}$) is shown in Fig. 4.23, where $\lambda_{1,2}$ are the Lyapunov exponents ($\lambda_1 \geq \lambda_2$) except for zero.The maximum value of λ_1 is approximately -7.3 which is still negative. In summary, the state collapse to limit cycle overall frequencies including the states with no motion in the high frequency region.

Furthermore, the amplitude dependency of the electric field is also investigated and presented in Fig. 4.24. In this voltage range, the Lyapunov exponents $\lambda_{1,2}$ are all negative, which means that all states are periodic.

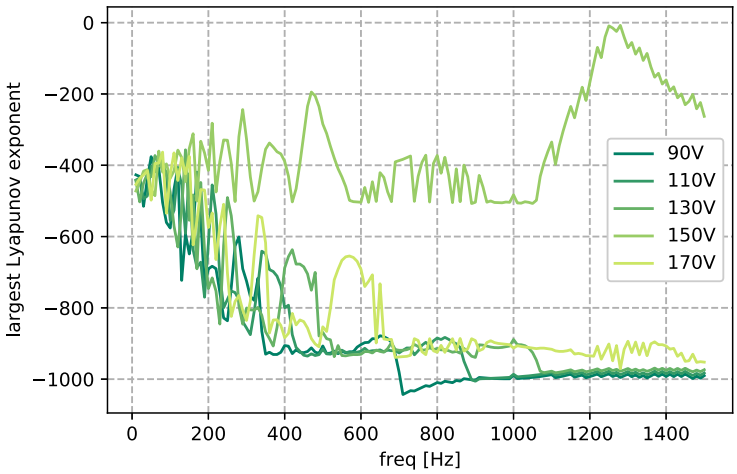

Figure 4.24: The Lyapunov exponents λ_1 in several effective voltages (calculated every 10Hz.)

4.4.7 Brief summary of the numerical results of the generalised model

The dynamics of $(P_{\parallel}^{\sigma}(t), P_{z}^{\sigma}(t))$ was obtained by the generalisation from the DC to the AC field. In each parameter of the voltages, it goes to the periodic state with the external frequency independent on the initial value with the exception of the sign of $P_{\parallel}$. $P_{\parallel}^{\sigma}(t)$ and $P_{z}^{\sigma}(t)$ have even and odd harmonics, so the velocity has only odd harmonics. The velocity also becomes periodic so that the reciprocating motion occurs. As the frequency f increases and gets close to $\sim 1/\tau_{\mathrm{MW}}$, the amplitude of the reciprocating motion decrease as $1/f$. By calculating the Lyapunov exponents, it was found that the system is the limit cycle which physically means the reciprocating motion in any frequencies we investigated.

4.5 Discussion: Comparison of the experimental results and the numerical results

In this section, the experimental results appeared in Sections 4.1 and 4.2 and the model and the numerical results appeared in Sections 4.3 and 4.4 are compared and discussed. Note that in the model, only one-dimensional motion is considered.

Though the experimental velocity was noisy, both the velocities obtained experimentally and numerically have the periodicity of the external frequency f. The odd high harmonics appeared only in numerical results. Because the peaks at high harmonics are more than ten times smaller than that at f, it is considered that the high harmonics buried in noise. The peaks in the low frequencies in (b) of Fig. 4.4 did not appear in the numerical result. The differences in the low frequency peaks of the two particles apart and non-clustered (See (b) of Fig. 4.9) indicate that this low frequency peaks are not due to a global vibration.

How can the low frequency (0-10Hz) peaks arise in principle? Is the surface viscosity related with? In Section 4.3, the translation velocity is expressed as

$$v(t) = -\frac{\epsilon_l}{\epsilon_0} a\tilde{\mu}_t E_0 \cos(\omega t) P_{\parallel}(t),$$

which already appeared in Eq. (4.14). Theoretically, $E_0 \cos(\omega t) P_{\parallel}(t)$ includes only odd peaks. To have δf :=0-10 Hz peaks in $v(t)$, $\tilde{\mu}_t$ should include peaks at $f + \delta f$ ($\simeq$ 300-310 Hz). If the $f + \delta f$ signal is assumed, $v(t)$ must include also $(f + \delta f) + f = 2f + \delta f$ peaks. However it was not observed. This means that the time dependency of $\tilde{\mu}_t$ (due to possible effects by vibration and surface friction) was NOT the reason for the low frequency peaks. The possible reasons for the low frequency peaks are follows: First, the reciprocating motion is physically asymmetric, because the the horizontal polarisation $P_{\parallel}$ do not alter its sign while the velocity do. There is a possibility to exist other unincorporated effect by this asymmetry. Secondly, the single particle was not completely isolated; it is possible to deviate by interactions with other particles away from it. By the later results in Chapter 5, the electrostatic interaction between the single particle and others seems to be negligible, because the single particle had no even peak. In contrast, the hydrodynamic interaction can affect to the single-particle motion. In fact, the slow time scale corresponding to the low frequency peaks is comparable to the time scale of interparticle distance changes of the clusters as shown later in Chapter 5.

As for the rotational diffusion, the time scale was $D_\theta^{-1} \simeq$0.03s in the experiment. The coefficient can be approximated from neither the one-dimensional model nor theory. The propelling axis is determined by the first moment of the surface charge distribution, so that the direction can be changed easily by the fluctuation of the distribution. This can be also affected by the shape of particles which is assumed to be spheres. Remind that the time scale of the angular changes for the DC rollers was 0.3 seconds in the literature [8] which used the particle of the similar material and the radius. It might be considered that the big difference in D_θ came from the difference in velocities.

To discuss the results of the MSD, a two-dimensional model is required. Thus a simple model is proposed in the next subsection.

4.5.1 A simple model for a roller reciprocating

Let us simplify the velocity of the Quincke roller under the AC field. To explore the possibility of the origin of the peaks in the low frequencies in (b) of Fig. 4.4, the existence of

a DC component of velocity is tentatively assumed. Consider a particle driven periodically with the DC component and with a translational diffusion and a rotational diffusion noise. Let $\boldsymbol{x}$ and θ be the position and the propelling axis. The equations follows

$$\dot{\boldsymbol{x}} = v(t)\hat{\boldsymbol{n}}(t) + \boldsymbol{\eta}(t) \tag{4.23}$$

$$\dot{\theta} = \sqrt{2D_\theta}\xi(t). \tag{4.24}$$

Here, $\hat{\boldsymbol{n}}(t) = (\cos\theta(t), \sin\theta(t))$ is the propelling direction vector. The noises are white gaussian: $\langle \eta_i(t)\eta_j(t')\rangle = 2D\delta(t-t')\delta_{ij}$, $\langle \eta_i(t)\rangle = 0$, $\langle \xi(t)\xi(t')\rangle = \delta(t-t')$, and $\langle \xi(t)\rangle = 0$ for arbitrary t, t'. Here let us assume velocity $v(t)$ to be sinusoidal with a DC element: $v(t) = v_0 + v_1\cos\omega t$.

4.5.2 The velocity autocorrelation of the simple model in Subsection 4.5.1

Velocity autocorrelation is calculated as follows.

$$\begin{aligned}
\langle \boldsymbol{v}(t_1)\cdot\boldsymbol{v}(t_2)\rangle &= v(t_1)v(t_2)\langle \hat{\boldsymbol{n}}(t_1)\cdot\hat{\boldsymbol{n}}(t_2)\rangle + 2D\delta(t_1-t_2) \\
&= v(t_1)v(t_2)\langle \cos\theta(t_1)\cos\theta(t_2) + \sin\theta(t_1)\sin\theta(t_2)\rangle + 4D\delta(t_1-t_2) \\
&= v(t_1)v(t_2)\langle \cos(\theta(t_1)-\theta(t_2))\rangle + 4D\delta(t_1-t_2) \\
&= v(t_1)v(t_2)\langle \cos(\Delta_{t_1-t_2}\theta)\rangle + 4D\delta(t_1-t_2),
\end{aligned} \tag{4.25}$$

where the average $\langle \dots \rangle$ means ensemble average. $\langle \cos(\Delta_\tau\theta)\rangle$ is angle deviation during time length τ. The probability which holds $\Delta_\tau\theta = \theta$ is defined $P(\theta,\tau)$, and its characteristic function is $\phi(s,t) := \int_{-\infty}^{\infty} \mathrm{d}\theta P(\theta,t)e^{i\theta s} = e^{-D_\theta s^2 t}$. For $\tau > 0$,

$$\begin{aligned}
\langle \cos(\Delta_\tau\theta)\rangle &= \int P(\theta,\tau)\cos\theta \mathrm{d}\theta \\
&= \frac{\phi(1,\tau)+\phi(-1,\tau)}{2} \\
&= e^{-D_\theta\tau}.
\end{aligned} \tag{4.26}$$

Therefore, with the exception of the translation diffusion, the velocity autocorrelation is calculated as

$$\begin{aligned}
& \langle \boldsymbol{v}(t_1)\cdot\boldsymbol{v}(t_2)\rangle \\
=\ & v(t_1)v(t_2)e^{-D_\theta|t_1-t_2|} \\
=\ & \left[v_0^2 + v_0v_1\left\{\cos(\omega t_1)+\cos(\omega t_2)\right\} + v_1^2\cos(\omega t_1)\cos(\omega t_2)\right] e^{-D_\theta|t_1-t_2|}
\end{aligned} \tag{4.27}$$

which cannot be expressed as a function of $(t_1 - t_2)$. That is to say, $\langle \boldsymbol{v}(t_1)\cdot\boldsymbol{v}(t_2)\rangle \neq \langle \boldsymbol{v}(t_1-t_2)\cdot\boldsymbol{v}(0)\rangle$.

Furthermore, the period-averaged velocity autocorrelation $C(\tau)$ obtained by the average over a period for t of $\langle \boldsymbol{v}(t)\cdot\boldsymbol{v}(t+\tau)\rangle$ ($\tau > 0$) (denoted by an overline) is

$$\begin{aligned}
C(\tau) := \overline{\langle \boldsymbol{v}(t)\cdot\boldsymbol{v}(t+\tau)\rangle} &= \left(v_0^2 + v_1^2\overline{\cos(\omega t)\cos(\omega(t+\tau))}\right)e^{-D_\theta\tau} \\
&= \left(v_0^2 + \frac{v_1^2}{2}\overline{(\cos(2\omega t+\omega\tau)+\cos(\omega\tau))}\right)e^{-D_\theta\tau} \\
&= \left(v_0^2 + \frac{v_1^2}{2}\cos(\omega\tau)\right)e^{-D_\theta\tau}.
\end{aligned} \tag{4.28}$$

The correlations Eq. (4.28) is displayed in Fig. 4.25, when DC: $(v_0, v_1) = (100, 0)$, oscillation: $(v_0, v_1) = (0, 100)$, and DC+oscillation: $(v_0, v_1) = (100, 100)$. (The unit for velocity is μm/s.) In the DC regime, the correlation is an exponential decay, and a damped oscillation in the oscillation regime. In the DC+oscillation regime, it is also the damped oscillation biased by the DC element.

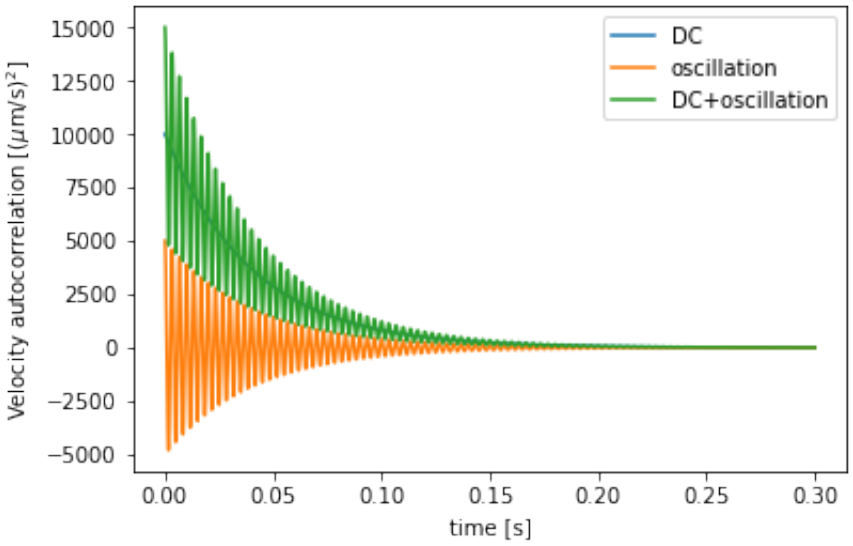

Figure 4.25: (Periodically averaged) velocity time correlation $C(\tau)$. (D_θ=25s^{-1}, $\omega/2\pi$ = 300Hz)

Practically, velocity autocorrelation calculated from experimental data for time series length t_f is

$$\mathrm{VelCor}(\tau; t_f) = \frac{1}{t_f - \tau} \int_0^{t_f - \tau} \langle \boldsymbol{v}(t) \cdot \boldsymbol{v}(t+\tau) \rangle \tag{4.29}$$

$$= \frac{v_0^2}{2} \left(\frac{\sin(2\omega t_f - \omega\tau) - \sin\omega\tau}{2\omega(t_f - \tau)} + \cos\omega\tau \right) e^{-D_\theta \tau}, \tag{4.30}$$

which is deviated from Eq. (4.28), but it is a damped oscillation similarly.

Comparison to the experiment The correlation is strongly dependent on the velocity's function form generally, it is not suitable to compare the experimental data in Fig. 4.10 directly. Instead of that, the decay rate for the periodic points can be compared to that estimated from Fig. 4.11: $D_\theta \simeq 3 \times 10^2 \mathrm{s}^{-1}$.

4.5.3 The power spectrum of velocity of the simple model in Subsection 4.5.1

The power spectrum of the velocity time series is calculated by Fourier transformation of the velocity autocorrelation $\langle \boldsymbol{v}(t)\cdot\boldsymbol{v}(t+\tau)\rangle$ generally. In this periodic model, $\langle \boldsymbol{v}(t)\cdot\boldsymbol{v}(t+\tau)\rangle$ cannot be expressed as a function of only τ, so periodically averaged velocity correlation $C(\tau)$ Eq. (4.28) is used for obtaining the following power spectra. (If $v_1 = 0$, it corresponds $\langle \boldsymbol{v}(t)\cdot\boldsymbol{v}(t+\tau)\rangle$.)

The power spectrum of the velocity $\hat{C}(\Omega)$ at the external angular frequency ω is

$$\hat{C}(\Omega) = v_0^2 \frac{2D_\theta}{D_\theta^2 + \Omega^2} + \frac{v_1^2}{4}\left(\frac{2D_\theta}{D_\theta^2 + (\omega+\Omega)^2} + \frac{2D_\theta}{D_\theta^2 + (\omega-\Omega)^2}\right), \tag{4.31}$$

when the translational diffusion is neglected. The power spectrums are illustrated in Fig. 4.26, when DC: $(v_0, v_1) = (100, 0)$, oscillation: $(v_0, v_1) = (0, 100)$, and DC+oscillation: $(v_0, v_1) = (100, 100)$. (The unit for velocity is μm/s.) As understood from Eq. (4.31), the

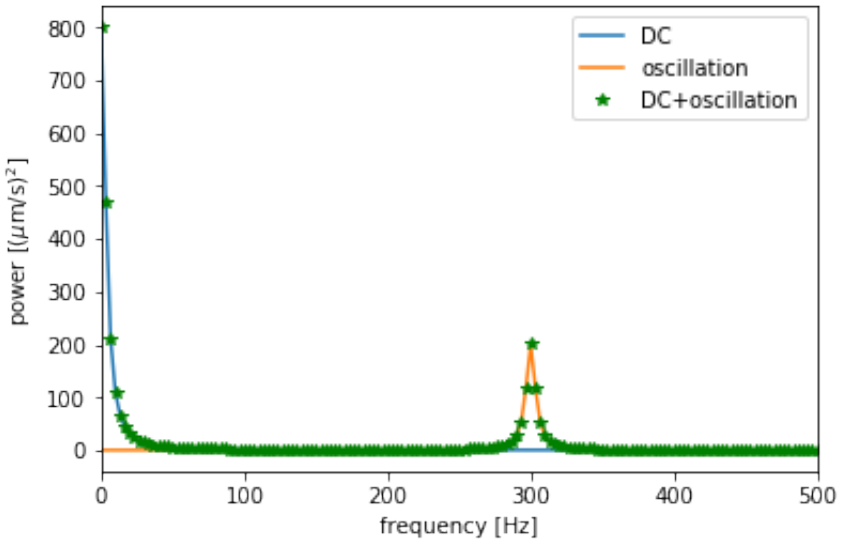

Figure 4.26: Power spectrum of velocity $\hat{C}(\Omega)$. (D_θ=25s^{-1}, $\omega/2\pi$ = 300Hz)

peak ratio of the DC element to ω is approximated by

$$\frac{\hat{C}(0)}{\hat{C}(\omega)} \simeq \frac{4v_0^2}{v_1^2}, \tag{4.32}$$

because the each tail is negligible. Therefore, the peaks at 0Hz and the external frequency ω are determined by v_0 and v_1. Until now, the translational diffusion has been neglected. If there is a translational diffusion, the constant value $4D$ is added to the spectrum.

Furthermore, the v_0 and D_θ dependencies are visualised in Fig. 4.27. The left figure in Fig. 4.27 shows that the DC element of velocity v_0 determined the zero component of the spectrum. The right figure in Fig. 4.27 depicts that the peak width at ω originates from D_θ.

For the information, the velocity autocorrelation $C(\tau)$ and the power spectrum $\hat{C}(\Omega)$ in the simple model is summarised in Table 4.1.

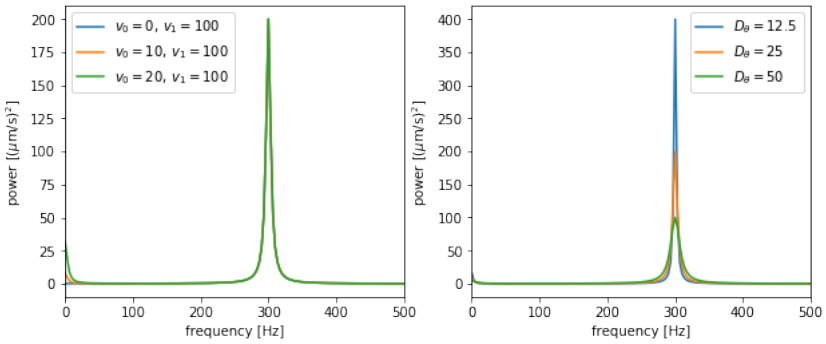

Figure 4.27: Power spectrum of velocity $\hat{C}(\Omega)$ ($\omega/2\pi = 300$Hz). left: $D_\theta = 25\text{s}^{-1}$, right: $(v_0, v_1) = (10, 100)[\mu\text{m/s}]$)

Table 4.1: Velocity autocorrelation $C(\tau)$ and power spectrum $\hat{C}(\Omega)$ in the simple model

	Brownian[7]	constant self-prop. with rot. diff.	oscillation with rot. diff.
$v(t)$	0	v_0	$v_1 \cos \omega t$
$C(\tau)$	$4\pi\delta(\tau)$	$v_0^2 e^{-D_\theta \lvert\tau\rvert}$	$\frac{v_1^2}{2} \cos\omega\tau e^{-D_\theta \lvert\tau\rvert}$
$\hat{C}(\Omega)$	$4D$	$v_0^2 \frac{2D_\theta}{D_\theta^2+\Omega^2}$	$\frac{v_1^2}{4}\left(\frac{2D_\theta}{D_\theta^2+(\omega+\Omega)^2} + \frac{2D_\theta}{D_\theta^2+(\omega-\Omega)^2}\right)$

	constant and sinusoidal self-prop.
$v(t)$	$v_0 + v_1 \cos \omega t$
$C(\tau)$	$\left(v_0^2 + \frac{v_1^2}{2}\cos(\omega\tau)\right) e^{-D_\theta \lvert\tau\rvert}$
$\hat{C}(\Omega)$	$v_0^2 \frac{2D_\theta}{D_\theta^2+\Omega^2} + \frac{v_1^2}{4}\left(\frac{2D_\theta}{D_\theta^2+(\omega+\Omega)^2} + \frac{2D_\theta}{D_\theta^2+(\omega-\Omega)^2}\right)$

Comparison to the experiment Based on this model, let us reconsider the experimental power spectrum in Fig. 4.5. First, the constant value in the spectrum by the DC element is smaller than the baseline of the spectrum. The peak at f naturally comes from the sinusoidal velocity. The peaks at small frequencies in (b) of Fig. 4.4 are all at smaller than 7.5 Hz, so they can be in the tail of the DC peak whose peak width $\sim D_\theta\,(\sim 30Hz)$. Though it cannot be concluded that the small-frequency peaks experimentally observed originated from the DC components of velocity, it is a possible reason. In this case, the DC peak appears 4 times larger than the peak at f (Eq. (4.32)), so v_0 is smaller than $\sqrt{(\text{the maximum value of the peaks})/4} \sim 10\mu\text{m/s}$.

4.5.4 The Mean Square Displacement of the simple model in Subsection 4.5.1

The mean square displacement is defined as $\mathrm{MSD}(\tau;t) = \langle(\boldsymbol{x}(t+\tau)-\boldsymbol{x}(t))^2\rangle$. Let us consider the MSD of the simple model in Subsection 4.5.1. By using the result Eq. (4.27),

$$\begin{aligned}
&\mathrm{MSD}(\tau;t)\\
&= \int_t^{t+\tau} \mathrm{d}t_1 \int_t^{t+\tau} \mathrm{d}t_2 \langle \boldsymbol{v}(t_1)\cdot\boldsymbol{v}(t_2)\rangle\\
&= \mathrm{MSD}^{00}(\tau;t) + \mathrm{MSD}^{01}(\tau;t) + \mathrm{MSD}^{11}(\tau;t) + \mathrm{MSD}^{(\mathrm{trans})}(\tau;t)
\end{aligned} \tag{4.33}$$

Here, MSD^{nm} means the part of MSD which came from the products of n-th and m-th component of velocity. $\mathrm{MSD}^{(\mathrm{trans})}$ is the term from the translation diffusion.

$$\mathrm{MSD}^{(\mathrm{trans})}(\tau;t) = 4D\tau \tag{4.34}$$

$$\mathrm{MSD}^{00}(\tau;t) = \frac{2v_0^2}{D_\theta^2}(e^{-D_\theta\tau} - 1 + D_\theta\tau) \tag{4.35}$$

$$\begin{aligned}
&\mathrm{MSD}^{01}(\tau;t)\\
&= \int_t^{t+\tau} \mathrm{d}t_1 \int_t^{t+\tau} \mathrm{d}t_2 v_0 v_1 (\cos(\omega t_1) + \cos(\omega t_2)) e^{-D_\theta|t_1-t_2|}
\end{aligned} \tag{4.36}$$

$$\begin{aligned}
&= \frac{2v_0v_1}{D_\theta^2+\omega^2}\left[\frac{2D_\theta^2+\omega^2}{D_\theta\omega}(\sin\omega(t+\tau)-\sin\omega t) - (\cos\omega t + \cos\omega(t+\tau))\right.\\
&\quad \left. + e^{-D_\theta\tau}\left\{(\cos\omega t + \cos\omega(t+\tau)) - \frac{\omega}{D_\theta}(\sin\omega(t+\tau)-\sin\omega t)\right\}\right]
\end{aligned} \tag{4.37}$$

$$\begin{aligned}
&\mathrm{MSD}^{11}(\tau;t)\\
&= \int_t^{t+\tau} \mathrm{d}t_1 \int_t^{t+\tau} \mathrm{d}t_2 v_0^2 \cos(\omega t_1)\cos(\omega t_2) e^{-D_\theta|t_1-t_2|}
\end{aligned} \tag{4.38}$$

$$\begin{aligned}
&= v_1^2\left[\frac{D_\theta}{D_\theta^2+\omega^2}\tau + \frac{\omega^2-D_\theta^2}{(D_\theta^2+\omega^2)^2}\right.\\
&\quad + \frac{2e^{-D_\theta\tau}}{(D_\theta^2+\omega^2)^2}(D_\theta\cos\omega t + \omega\sin\omega t)(D_\theta\cos(\omega(t+\tau)) - \omega\sin(\omega(t+\tau)))\\
&\quad \left. - \frac{1}{2\omega(D_\theta^2+\omega^2)}\left\{D_\theta\sin 2\omega t + \omega\cos 2\omega t + \omega\cos(2\omega(t+\tau)) - D_\theta\sin(2\omega(t+\tau))\right\}\right]
\end{aligned} \tag{4.39}$$

For a fixed t, it contains the linear term, decaying oscillation (with ω) and 2ω oscillation.

Consider the periodically averaged MSD in the same way as Eq. (4.28).

periodic average of $\mathrm{MSD}^{11}(t;\tau)$ for t:

$$\overline{\mathrm{MSD}^{00}}(\tau) = \mathrm{MSD}^{00}(\tau;t) \tag{4.40}$$

$$\overline{\mathrm{MSD}^{01}}(\tau) = 0 \tag{4.41}$$

Because the second column of Eq. (4.39) is transformed as

$$\frac{2e^{-D_\theta\tau}}{(D_\theta^2+\omega^2)^2}\left[\frac{D_\theta^2}{2}(\cos(2\omega t+\omega\tau)+\cos\omega\tau) - D_\theta\omega\sin\omega\tau - \omega^2(\cos\omega\tau-\cos(2\omega t+\omega\tau))\right], \tag{4.42}$$

the periodic average of $\mathrm{MSD}^{11}(t;\tau)$ for t is

$$\begin{aligned}\overline{\mathrm{MSD}^{11}}(\tau) &= v_1^2\left[\frac{D_\theta}{D_\theta^2+\omega^2}\tau + \frac{\omega^2-D_\theta^2}{(D_\theta^2+\omega^2)^2}\right. \\ &\quad \left.+\frac{e^{-D_\theta\tau}}{(D_\theta^2+\omega^2)^2}((D_\theta^2-\omega^2)\cos\omega\tau - 2D_\theta\omega\sin\omega\tau)\right]. \\ &\quad +4D\tau\end{aligned} \tag{4.43}$$

It includes linear term and damped oscillation with ω. Therefore, the periodic average of MSD which is naturally obtained from experimental data is

$$\begin{aligned}\overline{\mathrm{MSD}}(\tau) &= \frac{2v_0^2}{D_\theta^2}(e^{-D_\theta\tau}-1+D_\theta\tau) \\ &\quad +v_1^2\left[\frac{D_\theta}{D_\theta^2+\omega^2}\tau + \frac{\omega^2-D_\theta^2}{(D_\theta^2+\omega^2)^2}\right. \\ &\quad \left.+\frac{e^{-D_\theta\tau}}{(D_\theta^2+\omega^2)^2}((D_\theta^2-\omega^2)\cos\omega\tau - 2D_\theta\omega\sin\omega\tau)\right] \\ &\quad +4D\tau\end{aligned} \tag{4.44}$$

In the short-time limit ($\tau \to 0$), MSD is

$$\overline{\mathrm{MSD}}(\tau) \simeq 4D\tau + (v_0^2 + \frac{v_1^2}{2})\tau^2 + \mathcal{O}(\tau^3). \tag{4.45}$$

It indicates the diffusive part originates only from translational diffusion.

On the contrary, the long-time limit ($\tau \to \infty$), MSD is

$$\overline{\mathrm{MSD}}(\tau) \simeq \left(\frac{v_1(\omega^2-D_\theta^2)}{(D_\theta^2+\omega^2)^2} - \frac{2v_0^2}{D_\theta^2}\right) + \left(\frac{2v_0^2(D_\theta^2+\omega^2)+v_1^2D_\theta^3}{D_\theta((D_\theta^2+\omega^2)} + 4D\right)\tau, \tag{4.46}$$

which consists of a constant and a proportional term of τ.

The theoretical MSD and the exponent are illustrated in Figs. 4.28 and 4.29. The MSD deviates from the Brownian by increasing v_1 and clearly includes the oscillatory feature. In the short-time limit, the exponent varies from 1 by enhancing the oscillation. The periodicity in the exponent is observed. By increasing the oscillatory component v_1, the exponent can be larger than 2 or smaller than 0. The comparison of the green and red line in the left of Fig. 4.29 shows the difference in v_0 which changes the averaged line of the periodic change. In the long-time limit, the exponent goes to 1 in all cases.

Comparison to the experiment Let us compare the MSD of the model to that of the experiment in Figs. 4.12 and 4.13. The MSD of the simple model cannot fit perfectly to that of the experiment by multi-parameter fitting, so let us discuss by extract the feature

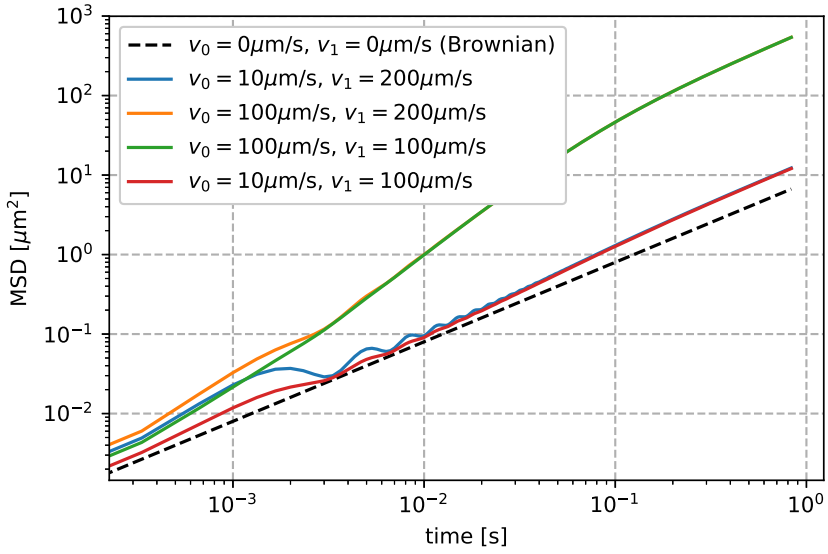

Figure 4.28: Theoretical MSD of the simple reciprocating model ($D_\theta = 30\text{s}^{-1}$, $D = 2\mu\text{m}^2/\text{s}$, 300Hz)

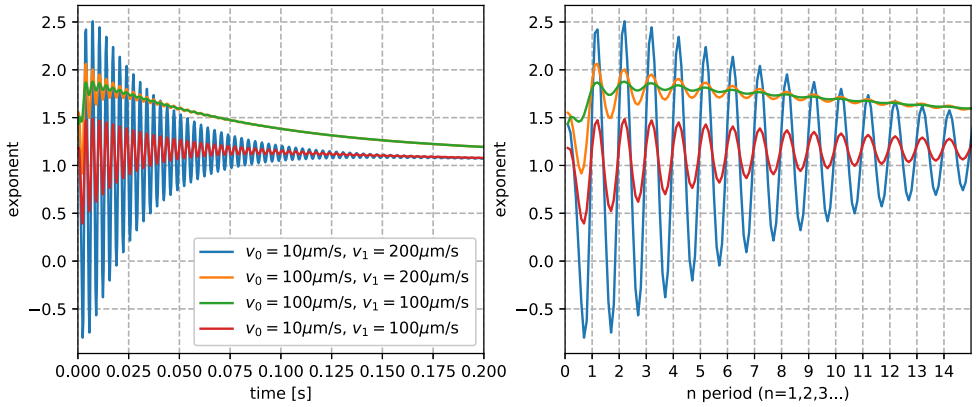

Figure 4.29: Theoretical exponent of the MSD in the model ($D_\theta = 30\text{s}^{-1}$, $D = 2\mu\text{m}^2/\text{s}$, 300Hz)

of both MSDs. The diffusivity in the short-time limit is due to the translational diffusion, although it can deviate from 1 by increasing the oscillation theoretically. The periodicity of the exponents come from the velocity's periodicity observed in both experimentally and theoretically. Though the exponent of the experiment cannot be reproduced, the superballistic behaviour is possible for the large oscillation regime. The averaged line of the periodic change in experimental exponents grows until about 7 periods and then decay, which is similar to the plots for the large DC velocity $v_0 = 100\mu$m/s. It suggests that the model with the DC element is more suitable to understand the experimental MSD, which the tentative assumption of the DC element was adopted in Subsection 4.5.1.

4.6 Summary on the single particle dynamics

In this chapter, the single-particle motion of the Quincke roller under the AC field was investigated experimentally and theoretically. The particle reciprocates at the frequency of the external field experimentally and theoretically, but the experiment included with noisy components especially in high frequencies. In addition, the small peaks at low frequencies were observed only in the experiment. In place of the one-dimensional theory, the simple model which has the velocity with a DC and a sinusoidal component was introduced. It showed that the theory with a non-zero DC component matched with the experimental results better than the model without a DC component in terms of the exponent of the MSD. The exponent of the MSD grows periodically from diffusive and reaches a peak which is superballistic then decreases, which appeared experimentally and theoretically though the exponents do not correspond quantitatively.

Chapter 5

Dynamic clustering of the Quincke rollers under the AC field

The dynamics of the single Quincke roller under the AC field was discussed in the previous chapter basically. In Section 4.1, the dynamic clustering of the Quincke rollers under the AC field in the experiment was introduced. In this chapter, the analysis of the dynamic clustering is reported focusing on the doublet and triplet intensively. Each cluster is 100μm away from other particles at least. Although the isolation of clusters is not complete, there is no particle existing at the comparable distance to the interparticle distances inside a cluster. In that sense, it is reasonable to analyse only clustering particles: a doublet and a triplet in the following.

5.1 Experimental Results: typical dynamics of a doublet

The data captured by the high magnification (x40) and at the high capture rate 3000fps is analysed here to investigate the dynamics comparison to the single reciprocation. The voltage was fixed at $V_{\text{eff}} = 150$V and 300Hz the same as Section 4.2. It should be remarked that the low magnification (x10) like Fig. 4.1 did not capture the reciprocating motion even with the high fps.

Let us focus on a doublet in a dilute suspension.

5.1.1 Typical trajectories and velocities

The trajectories of a doublet for long-time range is shown in Fig. 5.1. The trajectories are similar to that of the non-clustering particle in Section 4.2. Also, they keep the interparticle distance within some range even over 1091 periods.

To see the typical changes in the position and velocity, positional change(t) and velocity(t) for a short-time range are shown in (a) and (b) of Fig. 5.2. x_i, y_i mean the x,y-coordinate of i-th particle's position ($i = 1, 2$), and v_{ix}, v_{iy} is the x,y-coordinate of the velocity of i-th particle.

The root mean square velocity was $v_{\text{RMS}} \simeq \sqrt{\overline{v^2(t)}} \sim 4 \times 10^2 \mu$m/s for the both particles. The time average is taken for 3.639 seconds ($\simeq$1091 periods).

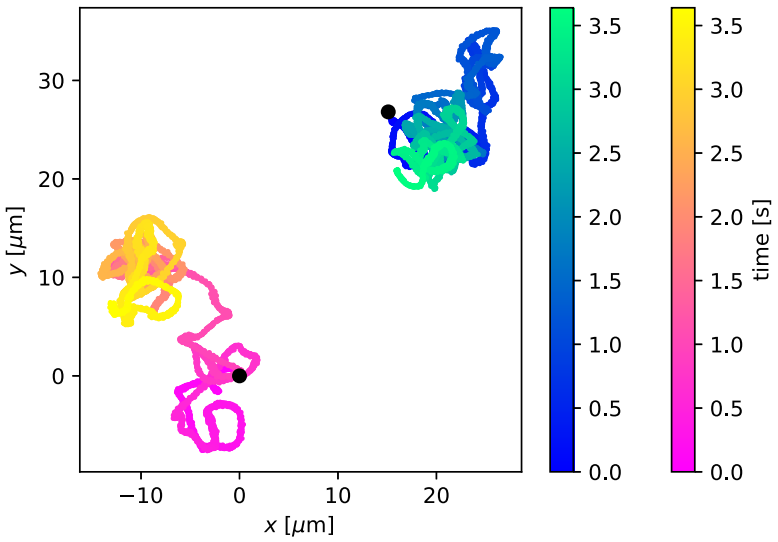

Figure 5.1: Trajectories of a doublet for 3.639 s (300Hz, 150V_{eff}). The black dots are the initial positions.

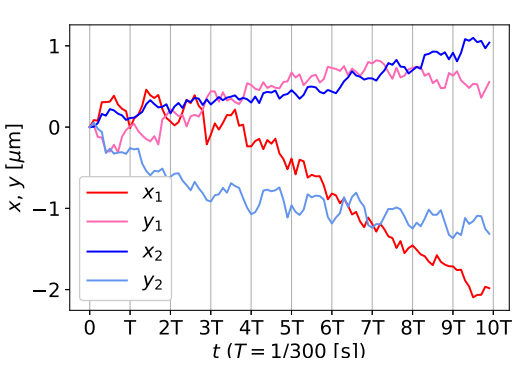

(a) $x_i(t)$, $y_i(t)$ $(i = 1, 2)$ (The initial points of all particles are shifted to (0,0) for visibility)

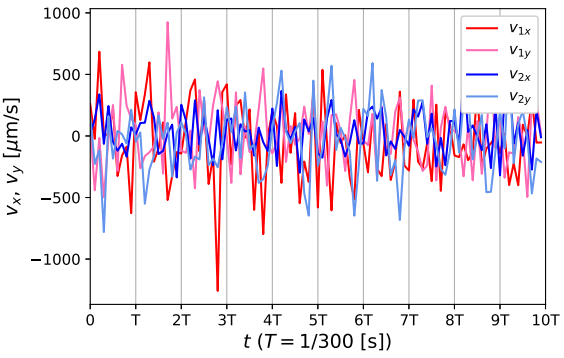

(b) $v_{ix}(t)$, $v_{iy}(t)$ $(i = 1, 2)$

Figure 5.2: Positional and velocity changes of particle 1 and 2 of the doublet (300Hz, 150V_{eff})

5.1.2 Power spectra of the velocities

First, to clarify the properties of the velocities, the power spectra are calculated along both x, y-axis and shown in Fig. 5.3 which are denoted as $S_{v_{nx}v_{nx}}$, $S_{v_{ny}v_{ny}}$ $(n = 1, 2)$.[1] There is the peak at the external frequency f in the both spectra similarly to the single-particle case. They have also the small peak at the third harmonic, which was expected by the result on the single-particle model in Section 4.4. However, they also have the second harmonic in both spectra, which does not appear in the single-particle theory. It is considered due to the dipolar-dipolar interaction.

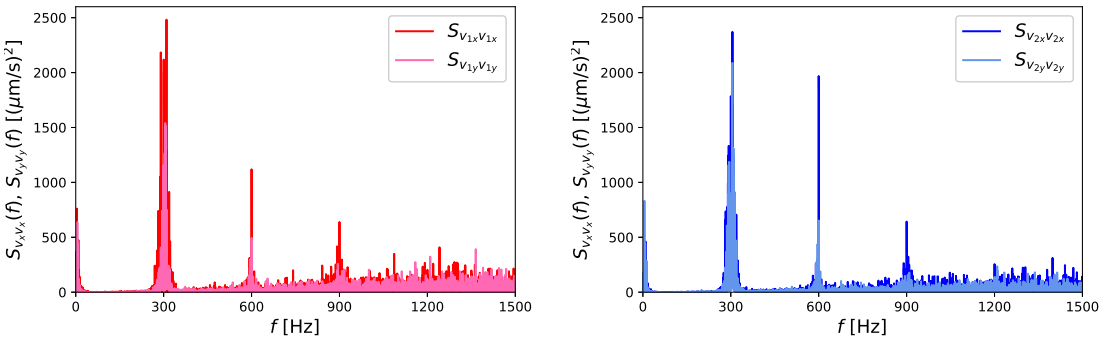

(a) Particle 1 (b) Particle 2

Figure 5.3: Power spectra of $v_{ix}(t), v_{iy}(t)$ of the particle $i = 1, 2$ of the doublet (300Hz, $150\mathrm{V}_{\mathrm{eff}}$)

To average the heterogeneity in x, y, "the velocity amplitude" which is the square root of the sum of normalised power in Fig. 5.3 is depicted in Fig. 5.4. This shows the two particles of the doublet behave equally.

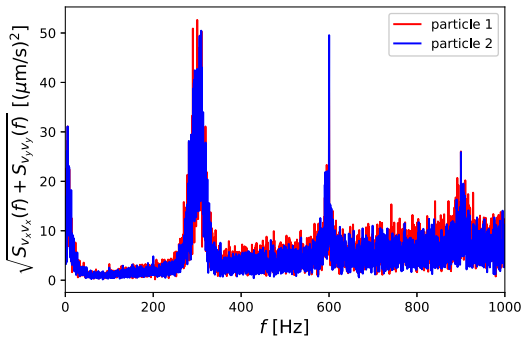

Figure 5.4: Velocity amplitude of particle 1 and 2 of the doublet (300Hz, $150\mathrm{V}_{\mathrm{eff}}$)

[1] The accuracy of the frequency axis ∼0.3Hz.

Next, the close view in the low frequency region of Fig. 5.3 is illustrated in Fig. 5.5. As was observed in the single-particle case in Section 4.2, the small peaks are observed in the low frequency region (<10Hz).

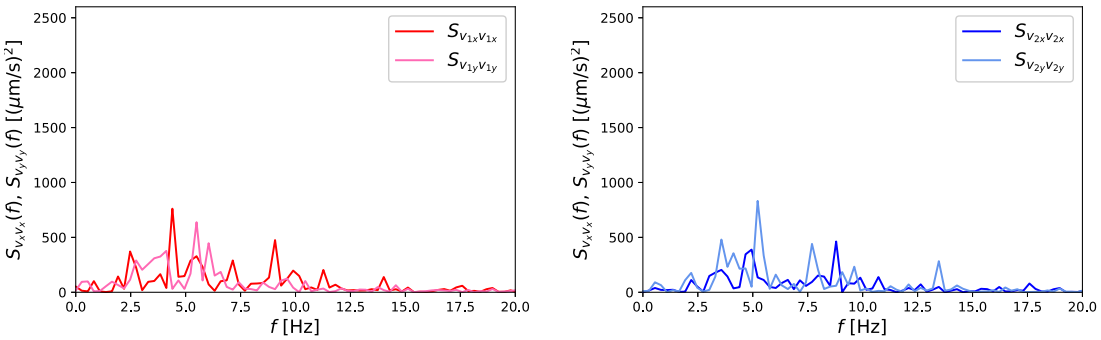

(a) Particle 1 (b) Particle 2

Figure 5.5: The close view in the low frequency region of Fig. 5.3

Then the power spectra of the speed time series $|\boldsymbol{v}_i(t)|$ $(i = 1, 2)$ are shown in Fig. 5.6. Unlike the single-particle case, the small peaks at f and $2f$ are observed, which means the speed periodicity. However, the ratio of the peak and the baseline is ~ 10 which is much smaller than that in the velocity power spectrum $\sim 10^3$. Thus, the periodicity of the speed is much weaker than that of the directional change.

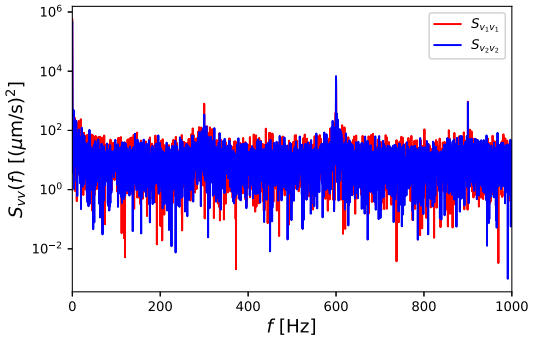

Figure 5.6: Power spectra of $|\boldsymbol{v}_i(t)|$ of particle $i = 1, 2$ of the doublet (300Hz, 150V_{eff})

To show the reciprocating tendency more directly, the angle change after a half period $\Delta\theta$ is shown in Fig. 5.7 similarly to the single-particle case in Fig. 4.8. The typical angle change $\Delta\theta = \pi$, which means that the directional reversal tend to occur. The persistent indices $\langle \cos \Delta\theta \rangle$ are approximately -0.6 and -0.7 respectively, which are closer to perfect reversal than the single-particle system.

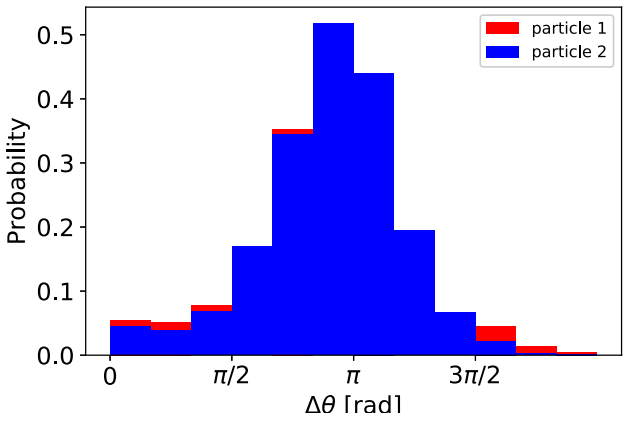

Figure 5.7: Histograms of angle changes after a half period for the doublet (300Hz, $150V_{\text{eff}}$)

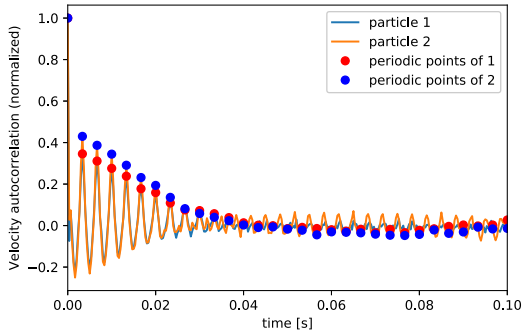

(a) doublet 1

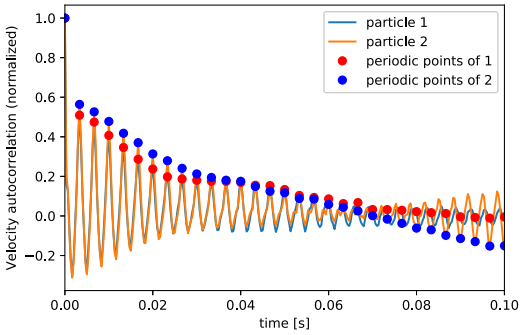

(b) doublet 2

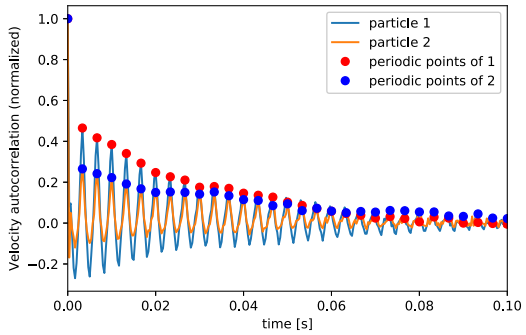

(c) doublet 3

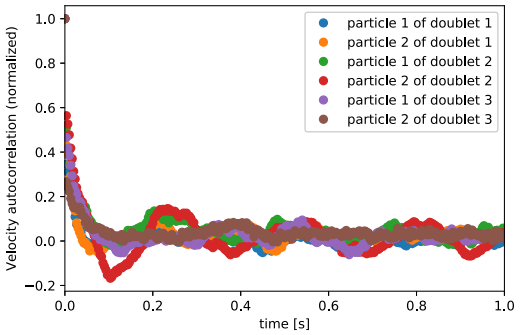

(d) Long-time behaviour (plotted only for $\tau = nT$)

Figure 5.8: (a)(b)(c) Velocity autocorrelations $\overline{\boldsymbol{v}_i(t+\tau)\cdot\boldsymbol{v}_i(t)}$ of each particle in three doublets. (d) Long-time behaviour of the correlation plotted only for integer multiples of the period $\tau = nT$ (300Hz, 150V_{eff})

5.1.3 Estimation of the effective rotational diffusion coefficient D_θ

Similarly to the single-particle case, the velocity autocorrelations $\overline{\boldsymbol{v}_i(t+\tau)\cdot\boldsymbol{v}_i(t)}$ of particle $i = 1, 2$ are calculated and shown in Fig. 5.8. (a), (b) and (c) are the autocorrelations of three doublets: the doublet 1, doublet 2 and doublet 3. In all samples, the correlations of the particle 1 and 2 similarly decay and oscillate at the period of the external frequency, which is shown by the red and blue dots. Comparing to the correlation of the single-particle in Fig. 4.10, the oscillation of the doublet is clearer. The correlation at $\tau = nT$ $(n = 1, 2, \dots)$ is positive for small n, but that at $\tau = nT$ for large n can be negative, as understood by the reversal of the reciprocating axis.

(d) of Fig. 5.8 shows the correlation at only integer multiples of the period of each particle in the three samples. The long-time ($\sim$ 0.1s) periodic structure is observed in the correlations, which did not appear in the single-particle correlation in Fig. 4.11. To estimate the rotational diffusion coefficient D_θ, the autocorrelation averaged over six correlations is plotted in Fig. 5.9. To show in the semilog plot, the absolute values were taken. The fast decay rate in less than 0.08s is obtained $D_\theta \simeq 6 \times 10^2 \text{s}^{-1}$ ($D_\theta^{-1} \simeq$0.02s).

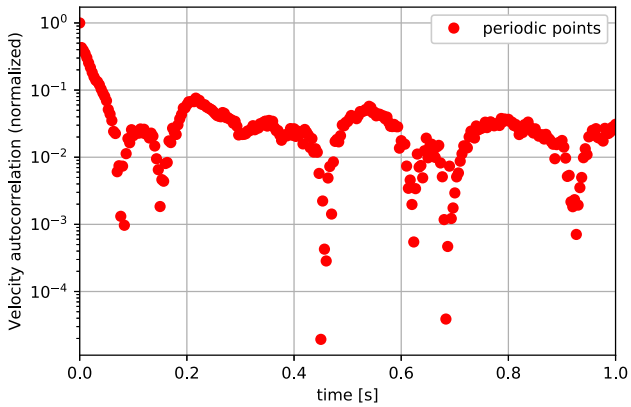

Figure 5.9: Decaying ensemble averaged velocity autocorrelation $\overline{\boldsymbol{v}_i(t+\tau)\cdot\boldsymbol{v}_i(t)}$ of the doublets (plotted only for $\tau = nT$) (300Hz, 150V_{eff})

5.1.4 Configuration of the doublet and Two-particle correlation

In this subsection, the configurational change and correlation between two particles that consist of a doublet are discussed. Consider the situation which is illustrated in Fig. 5.10.

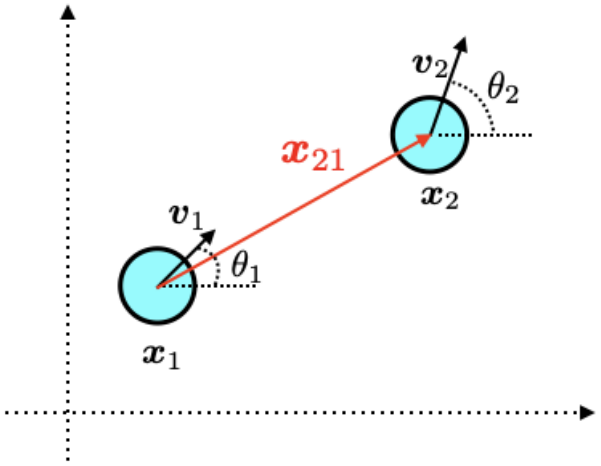

Figure 5.10: Notation for the configuration of particle 1 and 2 of a doublet

Let $\boldsymbol{x}_i$, $\boldsymbol{v}_i$ and θ_i are the position, velocity and propulsion angle of i-th particle. The relative position vector is defined as $\boldsymbol{x}_{21} = \boldsymbol{x}_2 - \boldsymbol{x}_1$.

Configuration (a) and (b) of Fig. 5.11 shows the time series of the distance between two particles in the doublet $|\boldsymbol{x}_{21}(t)|$ and the power spectrum of the time-average subtracted distance. The interparticle distance varies within $7 \sim 20\mu$m, where the minimum distance physically possible is 5μm which means the contact. The time average of the interparticle distance is $12.2\pm3.3\mu$m. The other particles away from the doublet were located at the distances $\sim 100\mu$m. Thus, the interparticle distance of the doublet is sufficiently smaller than the distance to other particles. Since the dipole-dipole interaction and the hydrodynamic interaction are proportional to $1/r^3$ and $1/r^2$ (See Eqs. (2.53) and (2.54).), the hydrodynamic interaction with the particles outside the cluster is more likely to affect the motion of the doublet, yet it is not larger than the interaction inside the cluster.

As for the power spectrum, there are peaks around ∼1Hz. The time scale of the largest peak is 0.4s, which is the long-time changes seen in the time series (a). The inset figure shows the smaller peaks at f and high harmonics, which indicates the periodicity of the interparticle distance.

Next, the angle between the relative position vector $\boldsymbol{x}_{21}(t)$ and the positive direction of x-axis is shown in (c) of Fig. 5.11. The power spectrum of the time-average subtracted angle is also presented in (d) of Fig. 5.11. The angle changes slowly (approximately same time scale as the changes of the interparticle distance) in accompany with the small periodic variation at f.

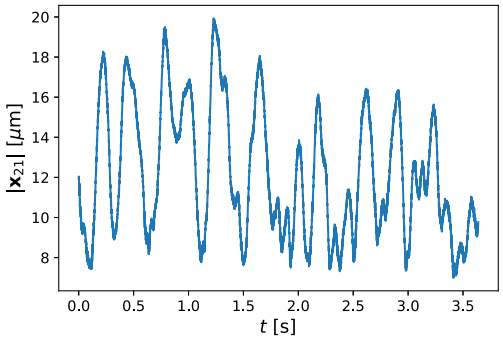

(a) Distance between two particles $|\boldsymbol{x}_{21}|$

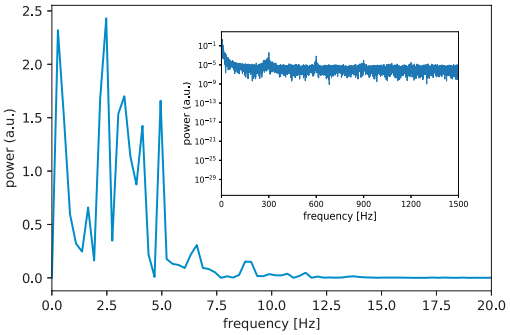

(b) Power spectrum of the interparticle distance (time-average subtracted)

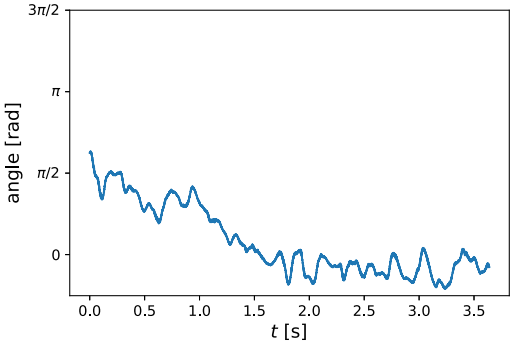

(c) Angle of the relative position vector $\boldsymbol{x}_{21}(t)$

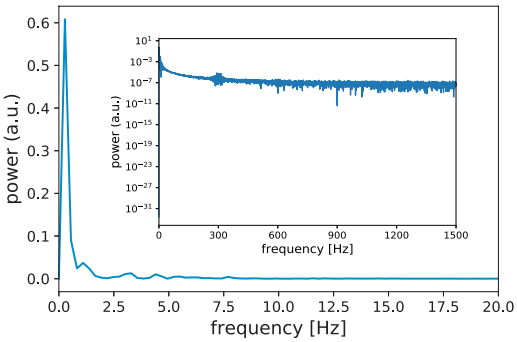

(d) Power spectrum of the angle of relative position vector $\boldsymbol{x}_{21}$ (time-average subtracted)

Figure 5.11: Configuration change of the doublet (300Hz, 150V_{eff})

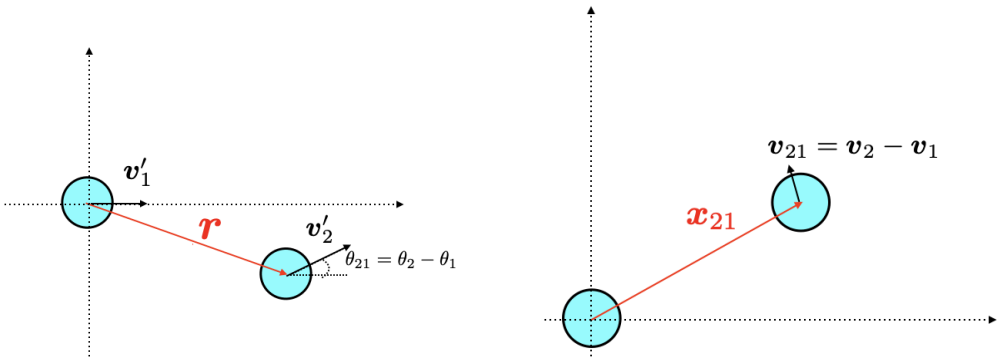

(a) Configuration in the rotating frame keeping direction of particle 1 to the x-axis positive

(b) Configuration in the moving frame with particle 1

Figure 5.12: Notation for the configuration of particle 1 and 2 of a doublet

Pair correlation To elucidate the effect of interactions, the two-particle correlation is computed. Let us consider the following two coordinate systems. One is the rotating frame keeping the direction of the particle 1 to the x-axis positive and the position of the particle 1 is set as the origin. ((a) of Fig. 5.12) The other is the moving frame with the 1st particle. ((b) of Fig. 5.12)

In the rotating frame, the velocity of i-th particle is changed to $\boldsymbol{v}_i' = \mathcal{R}(-\theta_1)\boldsymbol{v}_i$, where $\mathcal{R}(\theta)$ is the 2×2 rotation matrix of the rotation angle θ. The relative angle is $\theta_{21} = \theta_2 - \theta_1$. The relative position of the second particle follows

$$\boldsymbol{r}' = \mathcal{R}(-\theta_1)(\boldsymbol{x}_2 - \boldsymbol{x}_1). \tag{5.1}$$

In the moving frame, the second particle at $\boldsymbol{x}_{21}$ simply moves with the relative velocity $\boldsymbol{v}_{21} = \boldsymbol{v}_2 - \boldsymbol{v}_1$.

First let us see the density correlation. The probability density existing the second particle at $\boldsymbol{r}'$ in the rotating frame $\mathcal{P}(\boldsymbol{r}')$ corresponds the positional pair correlation function up to the normalisation. The (a) of Fig. 5.13 shows the result. Though the particle exists isotropically at the typical distance $\sim 12\mu$m, the propensity to exist the front and back is more frequent. Here the positive direction of x-axis is called "front".

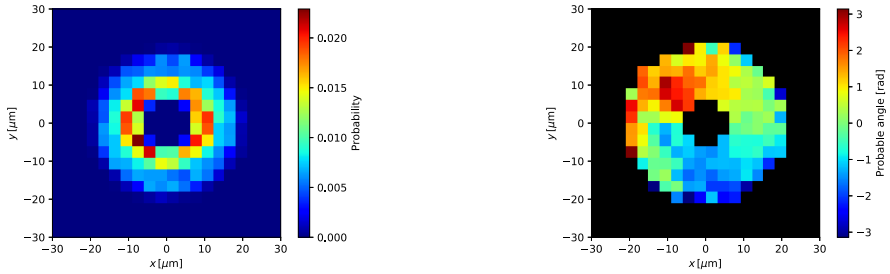

(a) Probability density of the second particle $\mathcal{P}(\boldsymbol{r})$

(b) Probable propulsion angle of the second particle $\Theta(\boldsymbol{r})$

Figure 5.13: (a)Probability density and (b) Probable propulsion angle of the second particle in the rotating frame (The particle 1 always propels positive direction of x-axis.)

Secondly, let us calculate the correlation of the propulsion directions. Although the correlation is the time average of $\cos\theta_{21}$ at every points $\boldsymbol{r}'$ over the whole time series in the rotating frame, the time average of θ_{21} is used for indicating the most probable angle of the particle 2. Here let $\Theta(\boldsymbol{r}')$ be the most probable angle at $\boldsymbol{r}'$, and it is shown in (b) of Fig. 5.13. It indicates that the particle 2 front tends to align the propelling direction, while the particle 2 at the right/left of the particle 1 tends to move diagonally backward right/left.

On the other hand, Fig. 5.14 shows the trajectory of the particle 2 in the moving frame with particle 1, that is $\boldsymbol{x}_{21}(t)$. The trajectory does not cover the surrounding area isotropically.

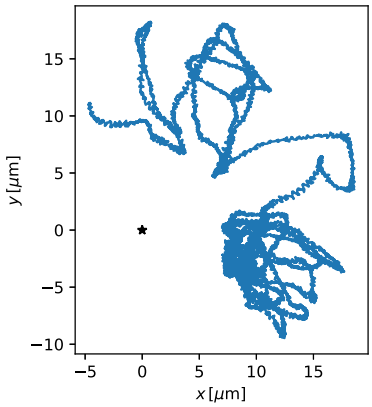

Figure 5.14: The trajectory of the particle 2 in the moving frame with particle 1 $\boldsymbol{x}_{21}(t)$. The black star is the fixed position of the particle 1.

5.1.5 Mean square displacement

Similarly to the single-particle case, the mean square displacement (MSD) is calculated and shown in Fig. 5.15. As the figure shows, the two particles of the doublet behave equally. The exponent of the MSD is shown in Fig. 5.16. The left and right figure show the long-time and short-time behaviour of the exponent $\beta(\tau)$ calculated by Eq. (4.1). There is a peak around 5 periods with the superballistic values that the single-particle MSD also had. The periodicity of the exponent in the short-time region shown in the right figure of Fig. 5.15 is observed similarly to the single-particle case.

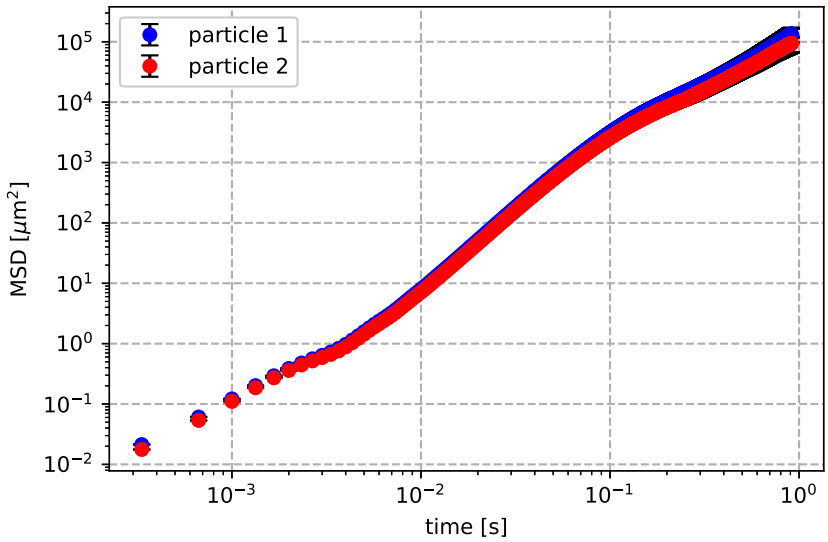

Figure 5.15: MSDs of each particle consists a doublet for AC 300Hz, 150V_{eff}. (Time is until one forth of whole time series. 1 error bar = 1 standard error.)

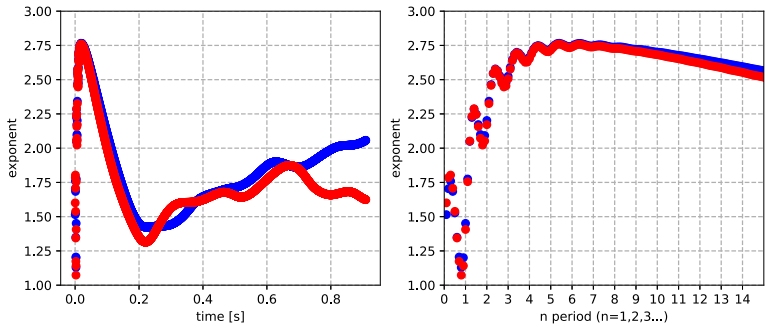

Figure 5.16: The exponent $\beta(\tau)$ of MSD(τ)$\propto \tau^{\beta}$ for AC 300Hz, 150V_{eff}. left: long-time behaviour, right: short-time behaviour

Because the two particles move similarly, the MSD of the c.o.m. (centre of mass) of the doublet is worth calculating. The MSDs of three doublets under the same voltage is shown in Fig. 5.17, and the exponents of the MSDs is presented in Fig. 5.18. The long-time behaviours (>0.2 seconds) differ in the samples, but the short-time is similar: The periodicity of the exponents and the peak of the exponent around 5 periods appear.

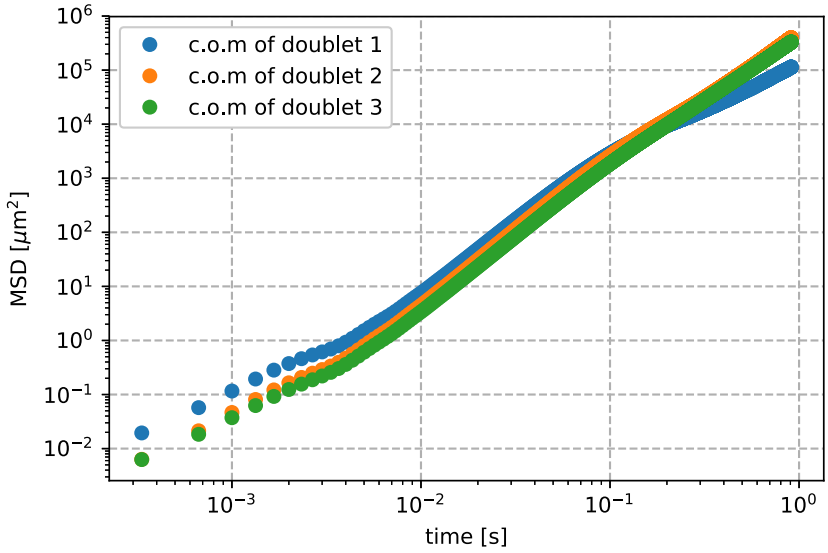

Figure 5.17: MSDs of the c.o.m.'s of three doublets (AC 300Hz, 150V_{eff}). (Time is until one forth of whole time series.)

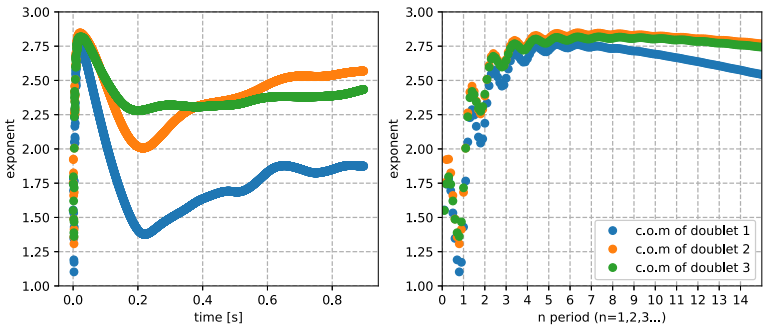

Figure 5.18: The exponent $\beta(\tau)$ of MSD(τ)$\propto \tau^{\beta}$ for AC 300Hz, 150V_{eff}. left: long time behaviour, right: short time behaviour

5.2 Experimental Results: typical dynamics of a triplet

In this section, the motion of a triplet which appeared in Section 4.1 is investigated.

5.2.1 Typical trajectories and velocities

The data captured by the high magnification (x40) and at the high capture rate 3000fps is analysed here to investigate the dynamics comparison to the single reciprocation. The voltage was fixed at $V_{eff} = 150V$ and 300Hz the same as Section 4.2.

The trajectories of a triplet for long-time range is shown in Fig. 5.19. More accurately, the Particle 1 approached to the particle 2 and 3, and they make the triplet which keep the triplet over 500 periods.

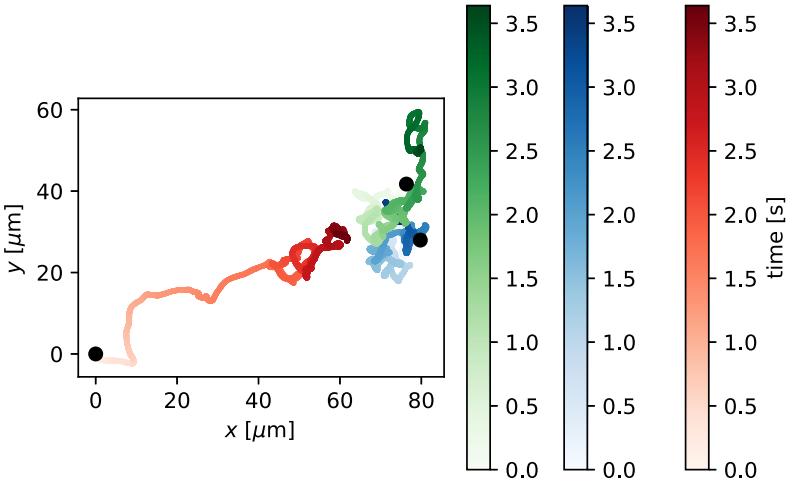

Figure 5.19: Trajectories of a doublet for 3.639 s (300Hz, $150V_{eff}$). The black dots are the initial positions.

To see the typical changes in the position and velocity, position(t) and velocity(t) for a short-time range are shown in (a) and (b) of Fig. 5.20 by extracting the first 10 periods from the whole time series 3.639s. x_i, y_i mean the x,y-coordinate of i-th particle's position ($i = 1, 2, 3$), and v_{ix}, v_{iy} is the x,y-coordinate of the velocity of i-th particle. Seeing the positional change (a) of Fig. 5.20, the reciprocation is clearer than those of the single-particle and the doublet, yet it is not obvious. The reciprocation of the particle 1 is not so clear compared to those of the particle 2 and 3, which seems to stem from the longer interparticle distance.

Moreover, the periodicity of the velocities is clearer than those of the single-particle and the doublet. The root mean square velocity was $v_{\mathrm{RMS}} \simeq \sqrt{\overline{v^2(t)}} \sim 3 \times 10^2 \mu$m/s for all particles. The time average is taken for 3.639 seconds ($\simeq$1091 periods).

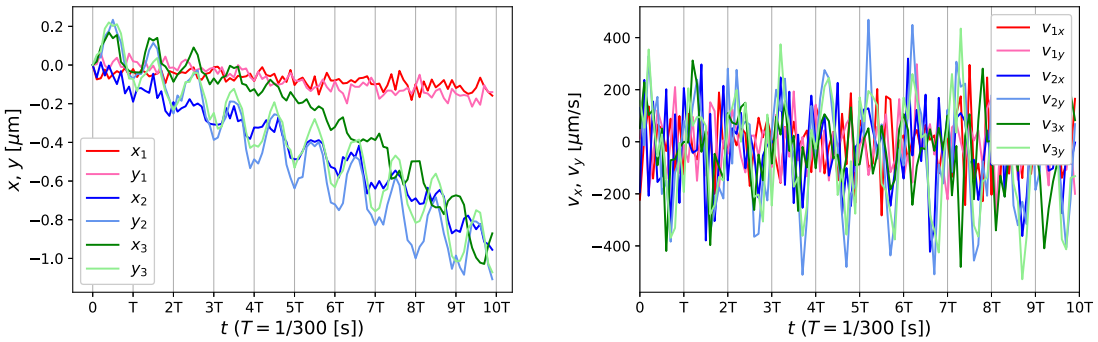

(a) $x_i(t)$, $y_i(t)$ $(i = 1, 2)$ (The initial points of all particles are shifted to (0,0) for visibility)

(b) $v_{ix}(t)$, $v_{iy}(t)$ $(i = 1, 2)$

Figure 5.20: Positional and velocity changes of the particle 1, 2 and 3 of the triplet (300Hz, $150V_{\text{eff}}$)

5.2.2 Power spectra of the velocities of the triplet

First, to clarify the properties of the velocities, the power spectra are calculated along both x, y-axis and shown in Fig. 5.21.[2] There is the peak at the external frequency f in the both spectra similarly to the single-particle case. They have also the small peaks at the second and third and probably fourth harmonics. The odd harmonics was expected by the result on the single-particle model in Section 4.4. The even harmonics is considered to originate from the electrostatic interaction.

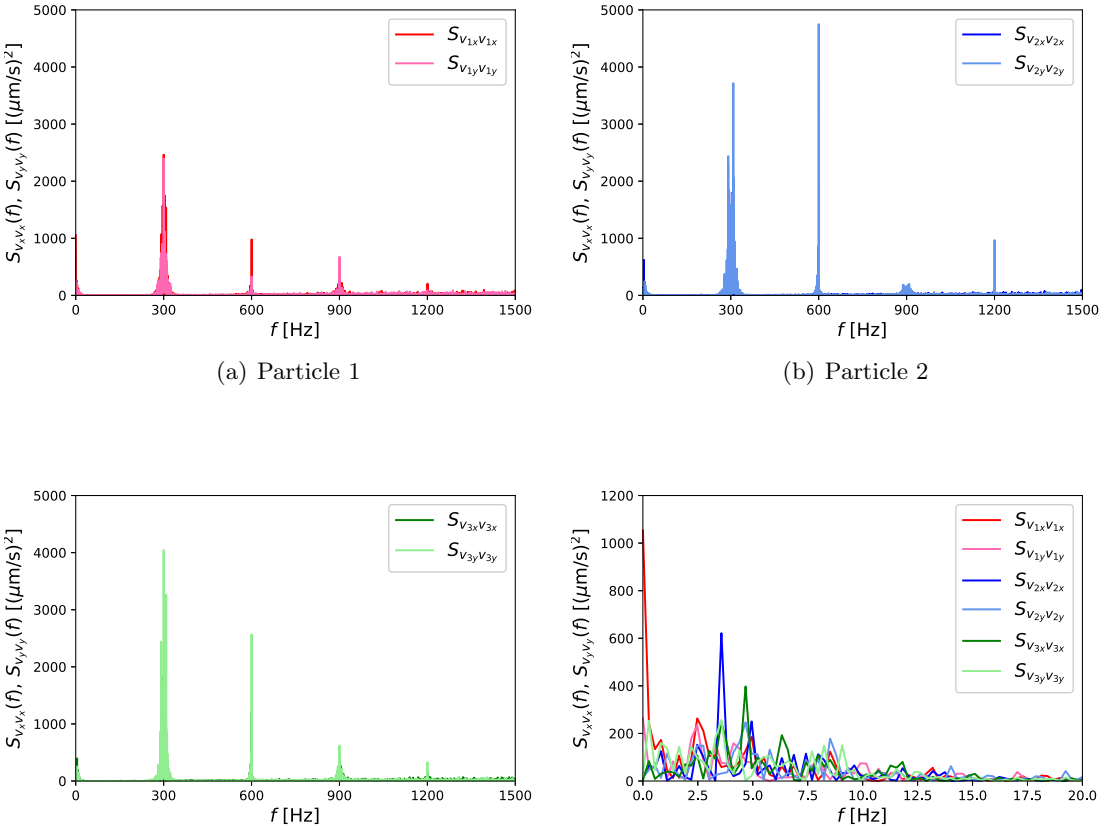

(a) Particle 1

(b) Particle 2

(c) Particle 3

(d) The close view in low frequency

Figure 5.21: Power spectra of velocity(t) of the particle 1, 2 and 3 of the triplet and their close view in low frequency (300Hz, 150V_{eff})

To average the heterogeneity in x, y, the velocity amplitude is depicted in (a) of Fig. 5.22. This shows the three particles of the triplet behave similarly. Next, the close view in the low frequency region of (a) of Fig. 5.22 is illustrated in (b) of Fig. 5.22. As was observed in the single-particle and doublet cases in Sections 4.2 and 5.1, the small peaks are observed in the low frequency region (<10Hz).

Then the power spectra of the speed $|\boldsymbol{v}_i(t)|$ $(i = 1, 2, 3)$ are shown in Fig. 5.23. Unlike the single-particle case, the small peaks at f, $2f$, $3f$ and $4f$ are observed, which means the speed periodicity. The periodicity of the speed is clearer than that of a doublet.

[2]The accuracy of the frequency axis ∼0.3Hz.

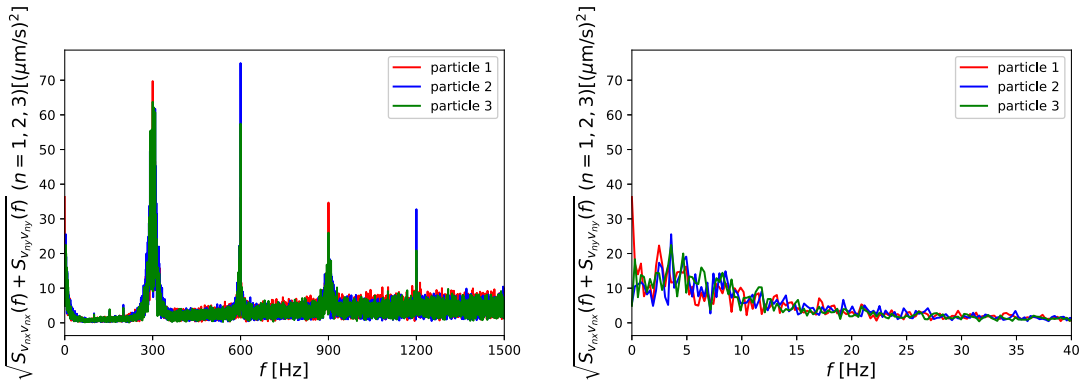

(a) Velocity amplitudes (b) The close view in the low frequency of (a)

Figure 5.22: Velocity amplitudes of the particle 1, 2 and 3 of the triplet (300Hz, 150V_{eff})

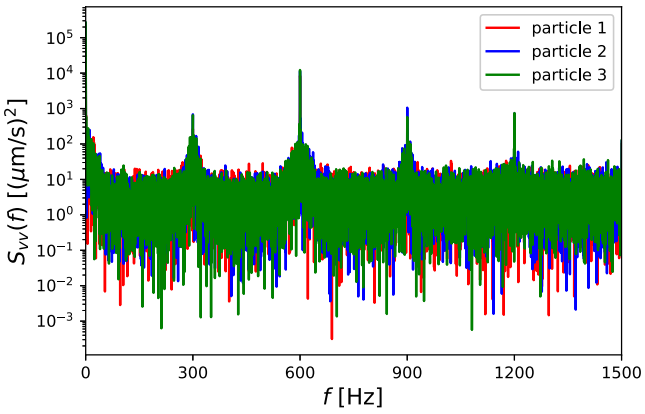

Figure 5.23: Power spectra of $|\boldsymbol{v}_i(t)|$ of particle $i = 1, 2, 3$ of the triplet (300Hz, 150V_{eff})

To show the reciprocating tendency more directly, the angle change after a half period $\Delta\theta$ is shown in Fig. 5.24 similarly to the single-particle case in Fig. 4.8. The typical angle change $\Delta\theta = \pi$, which means that the directional reversal tend to occur. The directional changes tend to be π, which means the directional reversal. The persistent indices $\langle \cos \Delta\theta \rangle$ of the particle 1, 2 and 3 are approximately -0.4, -0.8, -0.8 respectively.

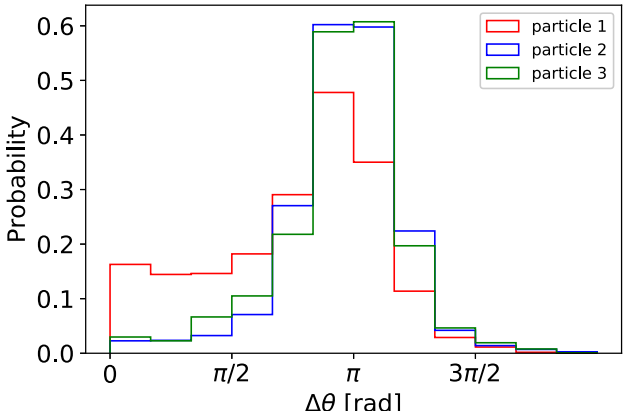

Figure 5.24: Histograms of angle changes after a half period for the triplet (300Hz, 150V_{eff})

5.2.3 Estimation of the effective rotational diffusion coefficient D_θ

Similarly to the single-particle and doublet cases, the velocity autocorrelations of particle 1, 2 and 3 of the doublet are calculated and shown in Fig. 5.25. They similarly decay with oscillation at the period of the external frequency. As is the case of the doublet, the correlation at $\tau = nT$ $(n = 1, 2, \dots)$ is positive for small n, but that at $\tau = nT$ for large n can be negative. It is because the oscillatory axis is inverted by the rotational diffusion. The long-time behaviours of the correlation at $\tau = nT$ shown in (a) of Fig. 5.26 have the long-time periodic structure similarly seen in Fig. 5.9, which is characteristic in the clustering. The absolute value of the average correlation over three particles is presented in (b) of Fig. 5.26. The fast decay rate obtained by the fitting to a exponential[3] is obtained $D_\theta \simeq 5 \times 10^2 \mathrm{s}^{-1}$ ($D_\theta^{-1} \simeq 0.02\mathrm{s}$).

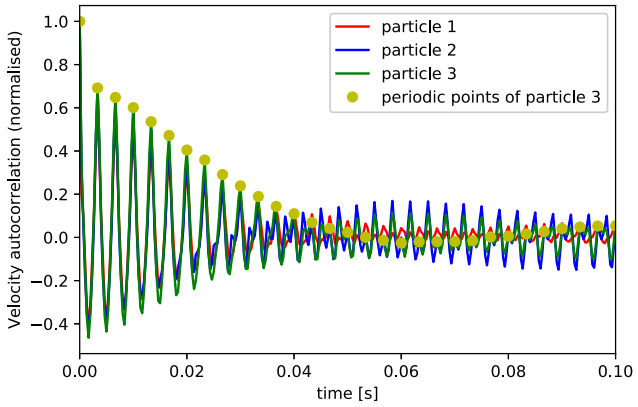

Figure 5.25: Velocity autocorrelations $\overline{\boldsymbol{v}_i(t+\tau) \cdot \boldsymbol{v}_i(t)}$ of particle 1, 2 and 3 of the triplet (300Hz, $150\mathrm{V}_{\mathrm{eff}}$) The correlation at integer multiples of the period $\tau = nT$ only for the particle 3 is plotted by the yellow dots.

[3]The time less than 0.04s is used

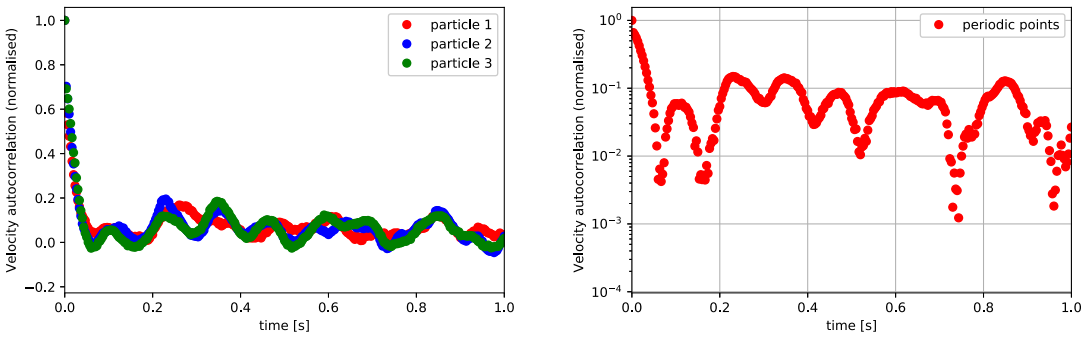

(a) Velocity autocorrelations of the triplet (b) Averaged velocity autocorrelation over the triplet

Figure 5.26: Long-time behaviour of velocity autocorrelation $\overline{\boldsymbol{v}_i(t+\tau)\cdot\boldsymbol{v}_i(t)}$ plotted only for $\tau = nT$ (300Hz, 150V_{eff})

5.2.4 Configuration and Pair correlation of the triplet

In this subsection, the configurational change and pair correlation of the triplet are discussed.

Configuration Consider the situation which is illustrated in Fig. 5.27 with inner angles α_1, α_2 and α_3 of the triangle.

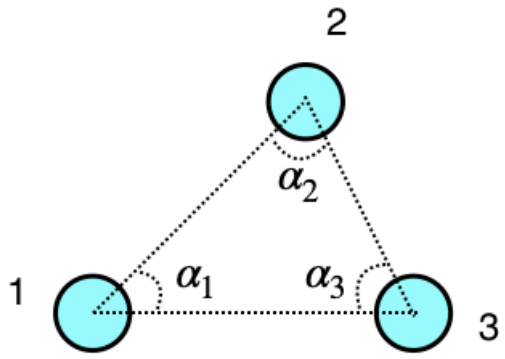

Figure 5.27: Notation for the configuration of the particle 1, 2 and 3 of a triplet

(a) and (b) of Fig. 5.28 shows the time series of the distances between two particles in the triplet $|\boldsymbol{x}_{ij}(t)|$ and the power spectra of the time-average subtracted distances. The distances change gradually with the long time scale 0.4s and the smaller periodicity which the inset figure shows.

Similarly to the doublet case, the other particles away from the doublet were located at the distances $\sim 100\mu$m. The interparticle distances of the triplet is smaller than the distance to other particles outside the triplet. In this triplet, one particle was away from the other two particles at first. Here we consider the triplet was formed after the all interparticle distances became comparable ($t > 1.5$s). The typical interparticle distance is $\sim 30\mu$m. Comparing to the doublet analysed in the above section, the effect by the interaction with the particles outside the cluster became larger, yet it is not dominant compared to the interaction inside the cluster. Next, the angles of the relative position vector $\boldsymbol{x}_{ij}(t)$ and its power spectrum are presented in (c) and (d) of Fig. 5.28. The angles do not alter so much during this time length but they change in accompany with the small periodic variation at f.

The changes of the inner angle α_i of the triangle are calculated and shown in (e) of Fig. 5.28. The value δ which characterises the "distance" from an equilateral triangle are calculated as

$$\delta = \sqrt{\frac{1}{3}\sum_{i=1}^{3}(\alpha_i - \frac{\pi}{3})^2} \tag{5.2}$$

which shown in (f) of Fig. 5.28. $\delta = 0$ means an equilateral triangle. Obtuse triangles have $\delta > \pi/6 \simeq 0.523$, so the triplet makes an obtuse triangle configuration for almost all the times of observation.

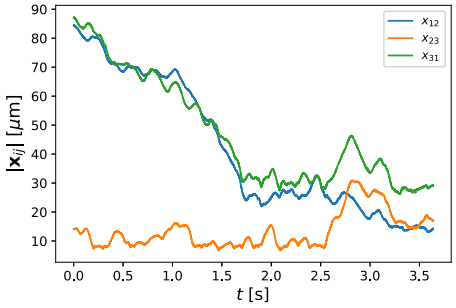

(a) Distances between two particles $|\boldsymbol{x}_{ij}|$

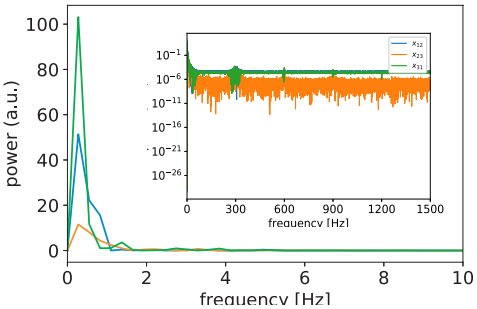

(b) Power spectra of the interparticle distances (time-average subtracted)

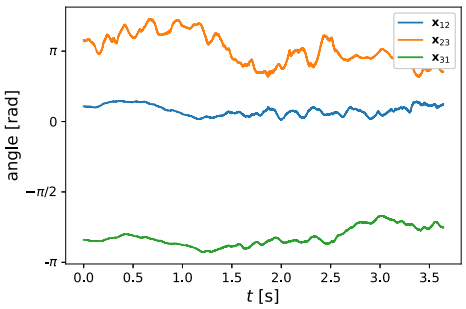

(c) Angles of the relative position vectors $\boldsymbol{x}_{ij}(t)$

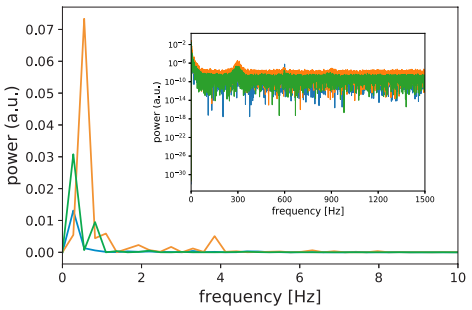

(d) Power spectra of the angles of relative position vectors $\boldsymbol{x}_{ij}$ (time-average subtracted)

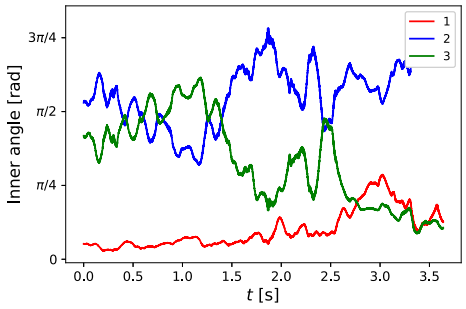

(e) Inner angles $\alpha_i(t)$

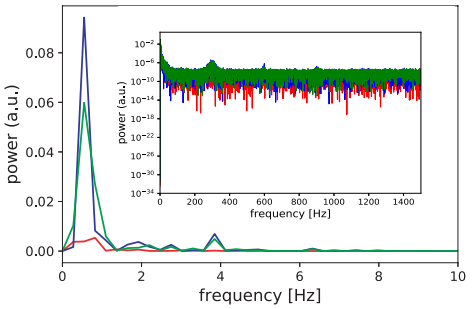

(f) Power spectra of inner angles $\alpha_i(t)$ (time-average subtracted)

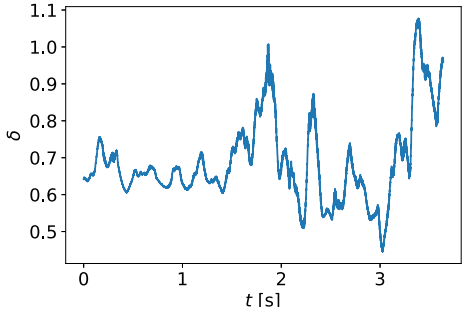

(g) "Distance" from a equilateral triangle δ

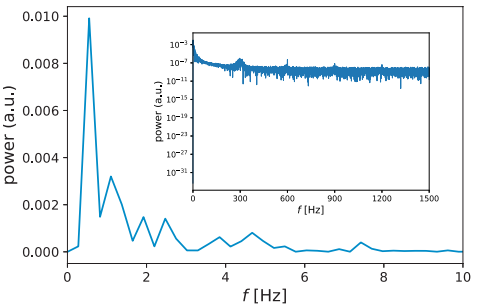

(h) Power spectrum of δ (time-average subtracted)

Figure 5.28: Configuration change of the triplet (300Hz, 150V_{eff})

Pair correlation To elucidate the effect of interactions, the pair correlation is computed in the same way as in Subsection 5.1.4.

First, the behaviours of the particle 2, 3 and 1 in the moving frame of the particle 1, 2, and 3 respectively appear in Fig. 5.29 .

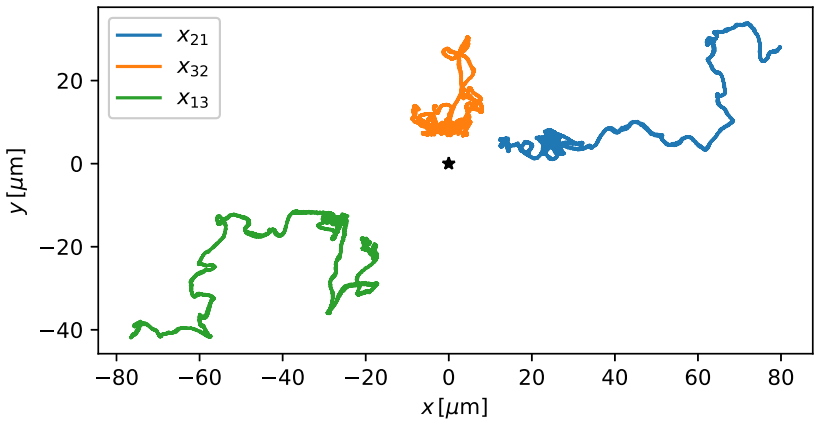

Figure 5.29: Trajectories of the relative vectors $\boldsymbol{x}_{21}$, $\boldsymbol{x}_{32}$ and $\boldsymbol{x}_{13}$ for 3.639s superimposed. The black star is the origin. (300Hz, 150$\mathrm{V}_{\mathrm{eff}}$)

On the other hand, let us consider the rotating frame introduced in Subsection 5.1.4. The probability density existing the second particle at $\boldsymbol{r}'$ in the rotating frame of the first particle is $\mathcal{P}(\boldsymbol{r}')$. Each combination of the probability densities is shown in (a), (c) and (e) of Fig. 5.30, using the time series after 1.700s out of 3.639s. Though the second particle exists isotropically to the front of the first particle, the three particles are not equivalent. It is considered because the observation time was limited.

Secondly, let us calculate the correlation of the propulsion directions. The most probable angles of the particle 2 to the particle 1 are shown in (b), (d) and (f) of Fig. 5.30, using the time series after 1.700s out of 3.639s in which the distances are kept smaller than 50μm. It indicates that the particle 2 at the front of the particle 1 tends to align the propelling direction, while the particle at the right/left of the particle 1 tends to move diagonally backward right/left assuming the propelling direction of the particle 1 to be front. However, the particle 3 at the left of the particle 2 tends to align the propelling direction, while the particle 3 at the right tends to move to the opposite direction. Moreover, the particle 1 at the diagonally backward right of the particle 2 tends to align the propelling direction, while the particle at the diagonally forward left tends to move to the opposite direction.

In principle, the correlation of the propulsion directions should be symmetric with respect to the x-axis as was observed in (b) of Fig. 5.13, when the two-body interaction is assumed. In (b), (d) and (f) of Fig. 5.30, they clearly break the symmetry to x-axis, which is considered to be the result by the three-body interaction.

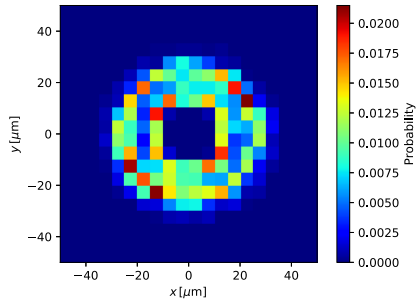

(a) $\mathcal{P}(\boldsymbol{r}')$ of the particle 2 with the rotating frame of 1

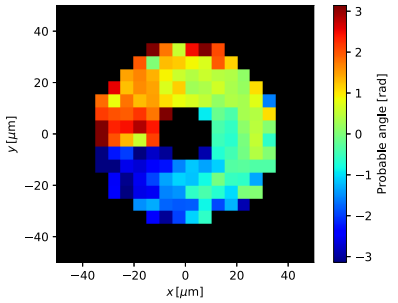

(b) $\Theta(\boldsymbol{r}')$ of the particle 2 with the rotating frame of 1

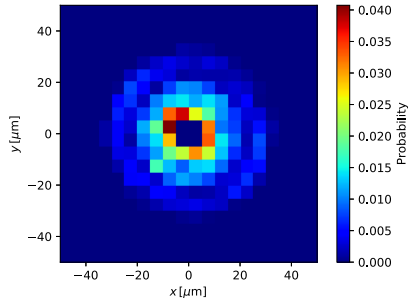

(c) $\mathcal{P}(\boldsymbol{r}')$ of the particle 3 with the rotating frame of 2

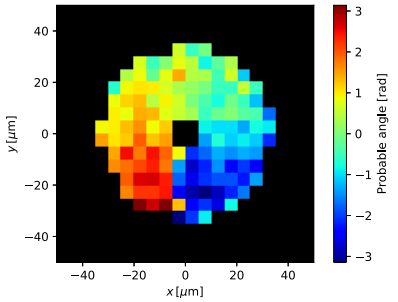

(d) $\Theta(\boldsymbol{r}')$ of the particle 3 with the rotating frame of 2

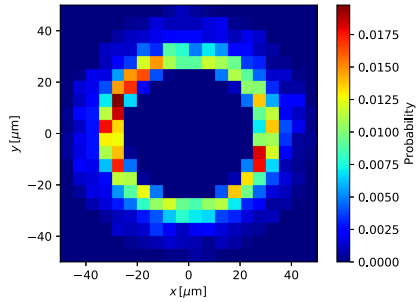

(e) $\mathcal{P}(\boldsymbol{r}')$ of the particle 1 with the rotating frame of 3

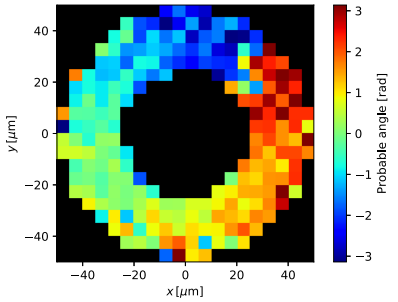

(f) $\Theta(\boldsymbol{r}')$ of the particle 1 with the rotating frame of 3

Figure 5.30: Probability density of the second particle $\mathcal{P}(\boldsymbol{r}')$ and Probable propulsion angle of the second particle $\Theta(\boldsymbol{r}')$ (300Hz, 150V_{eff})

5.2.5 Mean square displacement

Similarly to the single-particle and doublet cases, the mean square displacement (MSD) is calculated and shown in Fig. 5.31.

As the figure shows, the three particles of the triplet behave equivalently for the small-time interval. The exponent of the MSD of Fig. 5.31 is shown in Fig. 5.32. The left and right figure show the long-time and short-time behaviour of the exponent. There is a peak around 5 periods with the superballistic values that the single-particle MSD also had. The periodicity of the exponent in the short-time region shown in the right figure of Fig. 5.32 is observed similarly to the single-particle and doublet cases.

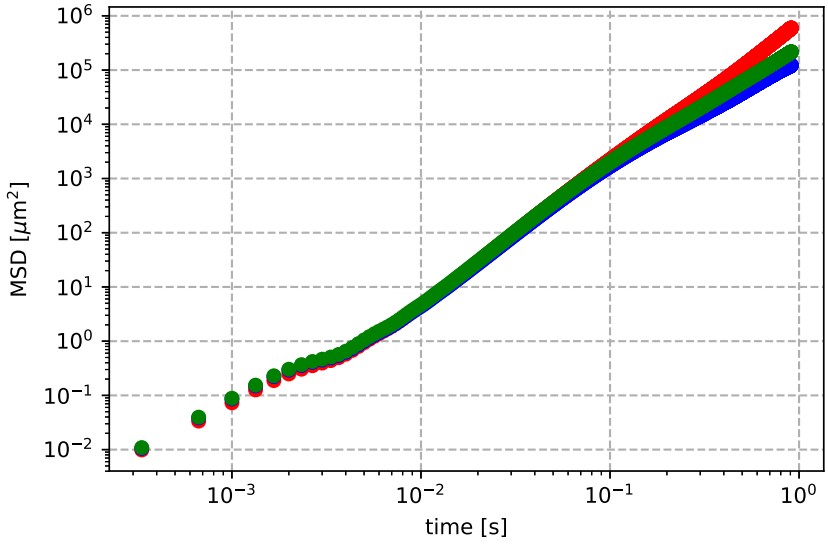

Figure 5.31: MSDs of each particle consists a doublet for AC 300Hz, 150V_{eff}.

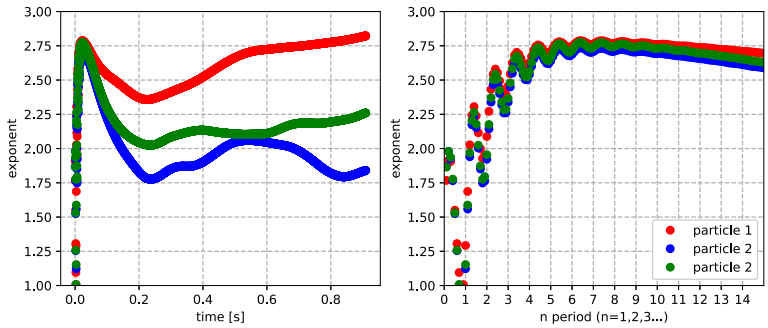

Figure 5.32: The exponent $\beta(\tau)$ of MSD(τ)$\propto \tau^{\beta}$ for AC 300Hz, 150V_{eff}. left: long-time behaviour, right: short-time behaviour

5.3 Discussion about the dynamic clustering

In the above two section, the experimental results of the dynamic clustering were described. However, it is not known that why the dynamic clustering happens. The interaction of the Quincke roller under the DC field calculated by Bricard *et al.* [8] was explained in Subsection 2.3.2. They only considered the propulsion angle change by interaction. In their DC case, there is an isotropic repulsion so that they do not make any clusters. Similarly to the DC case, suppose only the angle change of the propulsion is caused by the electrostatic interaction in the AC case. The P_z of Eq. (2.53) is changed from the constant value to the oscillation with f, so the time average is zero. The $P_{\parallel}$ of Eq. (2.53) is changed from the constant value to another constant value with the oscillation of $2f$ around the constant value, whose average is constant. Thus, this simple argument supports that there is no reason for the clustering when the only angle change is considered. Probably, the changes in the magnitude of the velocity should be taken into account in addition to the directional changes by the interaction to describe the dynamic clustering.

Clusterings of the Quincke rollers in another situation were experimentally realised by Karani *et al.* [50], which means the clustering seems to be robust under unknown conditions. They recently reported that many kinds of moving clusters appeared when the square pulse (DC) was intermittently applied [50]. (Already introduced in Fig. 2.14) The time interval between the two sequential pulses τ_T defined in their paper [50] (See Fig. 1.10) seems to correspond to the frequency in the AC system to some extent. Therefore, the reason why the clustering occurred might be possibly similar or relevant, whereas the reason for the clustering was not mentioned in the paper.

5.3.1 Attractive/Repulsive Interaction of the polarisations

To discuss the velocity changes by the electrostatic interaction, let us consider the constant horizontal polarisations of the two Quincke roller. Although the polarisations are also changed by the interaction in reality, how the c.o.m.'s are changed by the constant interaction is discussed for brevity here.

Here bipartite dipolar-dipolar interaction for constant two-dimensional polarisations $P_1 = 1$ and $P_2 = 1$ is considered. ($P_{\parallel}$ of particle 1 is abbreviated as P_1.)

Interaction energy is

$$U = \frac{1}{4\pi\epsilon_l} P_1 P_2 (\cos(\phi_2 - \phi_1) - \cos(\phi_1 - \varphi)\cos(\phi_2 - \varphi)), \tag{5.3}$$

where ϕ_1, ϕ_2 is the directions of polarisation of the particle 1 and 2, and φ is the angle of relative vector $\boldsymbol{x}_2 - \boldsymbol{x}_1$ to the x-axis direction.

The gradient of the interaction energy Eq. (5.3) is shown in Fig. 5.33 according to the relative angle of two polarisations. It indicates that the two particles can be attractive or repulsive depending on both the relative configuration and the relative propulsion angle. Since the force field always changes together with the configuration changes and the propulsion direction changes, it is not concluded that whether the occurrence of the dynamic clustering observed above is necessary or not without a multi-particle simulation.

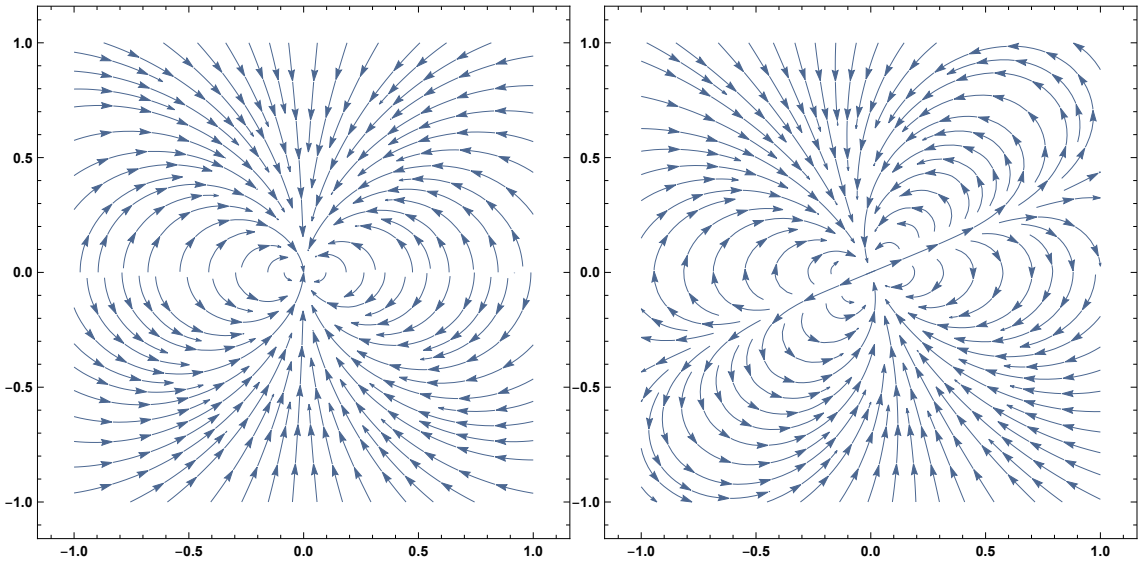

(a) $\phi_1 = 0$, $\phi_2 = 0$ (b) $\phi_1 = 0$, $\phi_2 = \pi/4$

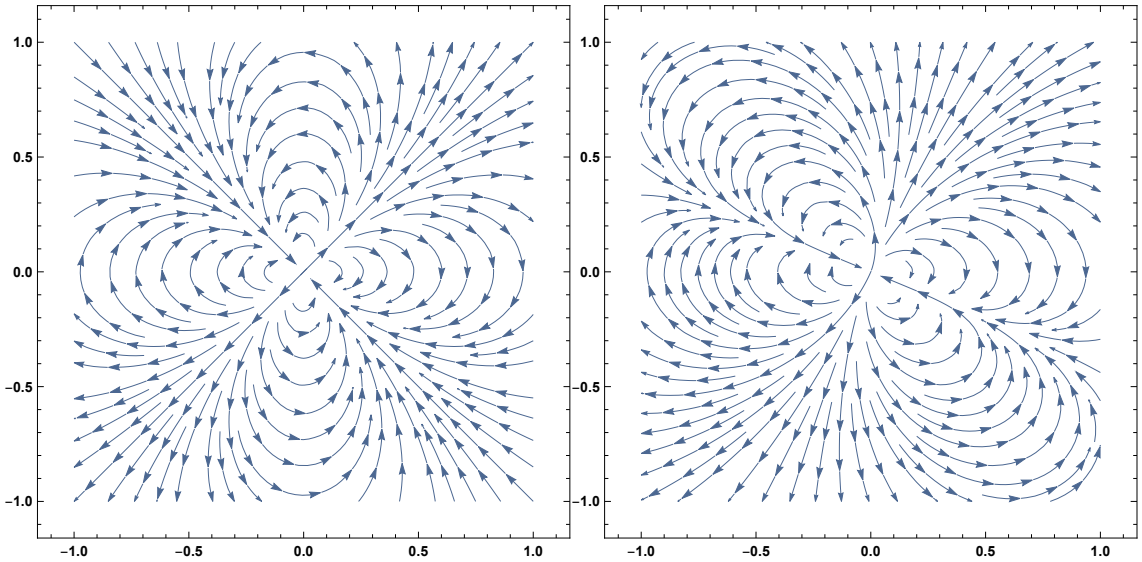

(c) $\phi_1 = 0$, $\phi_2 = \pi/2$ (d) $\phi_1 = 0$, $\phi_2 = 3\pi/4$

Figure 5.33: Gradients of the dipole-dipole interaction energy for each set of the propulsion direction

5.4 Summary on the dynamic clustering

In this chapter, the dynamics of a doublet and a triplet in the dynamic clustering under the AC field was explained. Each particle reciprocated periodically at the external frequency similarly to the single-particle case. The periodicity of the clustered particle was larger than that of the single particle. In addition to that, the power spectra of each particle had not only the odd peaks but also the even peaks which is considered to originate from the dipolar-dipolar interaction. The typical time scale for changing the propulsion axis D_θ^{-1} was the same order as the single-particle's.

As for the configurations of the doublet and triplet, there were typical interparticle distances. Moreover, in the doublet, one particle tended to align the propelling direction when it was at the front of another particle or anti-align near the back of another particle. In the triplet, the alignment and anti-alignment region around one of the particles depended on the individual particle.

Similarly to the single-particle case, the exponent of the MSDs grew with the periodic trend from diffusive and reached a peak which is superballistic then decreases.

Chapter 6

Conclusion and perspective

In this dissertation, nonequilibrium dynamics of periodically driven self-propelled colloids were studied experimentally, as an artificial self-propelled particle with a controllable time-dependent velocity. In the following, the principal results on each chapter are summarised.

In Chapter 4, the single-particle dynamics of the Quincke roller under the AC field were investigated. There was the periodicity of the propelling velocity at the frequency of the external field experimentally due to the angle reversal tendency at every half period. The reciprocating features of the single particle were explained by the generalisation of the theory on the Quincke roller under the DC field to that under the AC field. Although it was impossible to observe two-dimensional motions under various voltage amplitudes and frequencies due to the occurrence of vertical motions, the numerical results of the generalisation included the parameter dependency. Especially, the periodic state was a limit cycle in a wide-range of parameters, whose periodic state only depended on the sign of the horizontal polarisation. The theoretically unexpected features, which are the presence of low-frequency peaks and the anomalous MSD behaviour were found experimentally.

In Chapter 5, the locomotion of the doublet and the triplet which appeared spontaneously as a part of dynamic clustering of the rollers under the AC field was analysed. Each particle of the clusters reciprocated clearer than the single particle by the periodic velocity with not only odd harmonics but also even harmonics because of the dipolar-dipolar interactions. The configurations were dynamically changed with the periodicity but conserved within typical interparticle distances. Moreover, the alignment and anti-alignment regions of the second particle around the first particle were separated depending on the relationship between relative positional vector and the direction of the first particle, which can enhance the synchronisation of propelling direction in parallel or antiparallel.

However, to understand the dynamic clustering, the multi-particle simulation incorporating the velocity changes by the interactions should be performed. It can be the generalisation of the DC roller's simulation by Bricard *et al.* [8, 47] which solved the dynamics of the polarisations and positions simultaneously, or a simpler model which is similar to active nematics [5] but with the periodic velocity and a coarse-grained interaction. Another interesting point of view is the long-time behaviour which is observed in the low magnification. Because the reciprocation is small and fast, only the net motion can be observed in the setup. Instead, the long-time positional changes of the clusters can be captured so that the relationship between the configuration change and the motion of the cluster's c.o.m. is to be clarified. Also, the collective properties such as the cluster size distribution and the number fluctuation can be measured.

For the theoretical point of view on the single-particle, the reason why the low-frequency peaks appeared in the velocity power spectra was not explained. Also, the anomalous MSD behaviour was possible but do not have the perfect fitting to the experiment.

Overall, it is hoped that the study stimulates the researches on self-propelled particles by presenting an experimental example of periodic propulsions. Furthermore, the multi-particle experimental results were rare compared to the results on single-particle systems and collective systems, so that it enables us to understand how the effect of interactions can change the self-propulsions and the configuration change.

Appendix A

Material data

The material data of the particles used in this research and the previous research [8] is shown in Table A.1, where ϵ_r, σ and ρ are the relative permittivity, electric conductivity and density respectively. Also the data of the fluid used in this research is shown in Table A.2 comparing to other fluids. Here, η and $\nu = \eta/\rho$ are the viscosity and kinetic viscosity. The density of AOT/hexadecane (0.15mol/L) in Table A.2 was calculated when the volume change by dissolution was neglected. Thus, polystyrene and PMMA beads sink in the liquid of AOT/hexadecane.

	ϵ_r	σ ($\Omega^{-1}\mathrm{m}^{-1}$)	ρ (kg/m^3)	refractive index
PMMA	3.5∼4.5	$\lesssim 10^{-13}$	1.18×10^3	-
Polystyrene(PS)	2.4∼3.3	$\lesssim 10^{-14}$	$1.04\sim1.09\times10^3$	1.6

Table A.1: Data table of particles

	ϵ_r	σ ($\Omega^{-1}\cdot\mathrm{m}^{-1}$)	ρ (kg/m^3)
hexadecane	2.08	(5×10^{-8}: Dodecane [57])	7.735×10^2
AOT/hexadecane (0.15mol/L)	-	-	8.37×10^2
Water	80.4	-	1.0×10^3
Air	1.00059	-	1.2
	η (Pa·s)	ν (m^2/s)	refractive index
hexadecane [8]	2×10^{-3}	3×10^{-6}	1.4
Water	1×10^{-3}	1×10^{-6}	1.3
Air	1.8×10^{-5}	1.5×10^{-5}	1

Table A.2: Data table of fluids

About materials

- AOT (Bis(2-ethylhexyl) sulfosuccinate sodium, Docusate sodium)
  A surfactant, molecular weight=444.56. The chemical formula is shown in Fig. A.1.

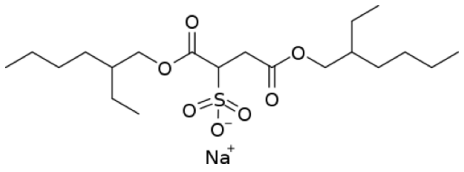

Figure A.1: AOT (Docusate sodium) Figure is from https://en.wikipedia.org/wiki/Docusate

- ITO (Indium Tin Oxide; transparent conducting film)

Appendix B

Physical values of the experimental system

- Debye length λ_D
  Let ϵ_l, T, n_0 and Z be the permittivity of liquid, temperature, the number density of ions and the valency number of ions. The Debye length is

$$\lambda_D = \sqrt{\frac{\epsilon_l k_B T}{2n_0(Ze)^2}}, \tag{B.1}$$

  where k_B and e are the Boltzmann constant and the elementary electrical charge.

  In a Quincke roller system,

$$\lambda_D \sim 10 \text{ (nm)}. \tag{B.2}$$

- Diffusion coefficient
  Diffusion coefficient of beads is calculated using the radius $a = 2.5 \times 10^{-6}$ m, (dynamic) viscosity of hexadecane $\eta = 2 \times 10^{-3}$ Pa·s and $T = 293$ K assuming the Fluctuation Dissipation Theorem (FDT) in equilibrium.

  Translational diffusion coefficient:

$$D = \frac{k_{\mathrm{B}}T}{6\pi a\eta} = \frac{1.38 \cdot 10^{-23} \times 293}{6\pi \times 2.5 \cdot 10^{-6} \times 2 \cdot 10^{-3}} = 4 \times 10^{-14}\,(\mathrm{m}^2/\mathrm{s}) \tag{B.3}$$

  Rotational diffusion coefficient:

$$D_\theta = \frac{k_{\mathrm{B}}T}{8\pi a^3\eta} = \frac{1.38 \cdot 10^{-23} \times 293}{8\pi \times (2.5 \cdot 10^{-6})^3 \times 2 \cdot 10^{-3}} \sim 5 \times 10^{-3}\,(\mathrm{s}^{-1}) \tag{B.4}$$

$$D_\theta^{-1} \sim 2 \times 10^2\,(\mathrm{s}) \tag{B.5}$$

- Péclet number (= (advection) / (diffusion)")
  Péclet number is defined as

$$Pe = \frac{vL}{D} \tag{B.6}$$

  with the typical speed v, the typical length (like a particle diameter) L and the translational diffusion coefficient D. Even assuming the lower speed than a Quincke roller $v = 10\mu\mathrm{m/s} = 10^{-5}$ m/s,

$$Pe = \frac{vL}{D} = \frac{10^{-5} \times 5 \cdot 10^{-5}}{4 \times 10^{-14}} \sim 10^4 \tag{B.7}$$

Thus, the thermal diffusion can be neglected.

- Reynolds number
  The typical speed of Quincke roller v is $100 \sim 1000\mu$m/s. Typical length is $L = 2a \sim 10^{-5}$m and kinetic viscosity is $\nu = 3 \times 10^{-6}$ (m^2/s). Even assuming high speed of a Quincke roller $v = 1$mm/s$= 10^{-3}$ m/s,

$$Re = \frac{VL}{\nu} = \frac{10^{-3} \times 5 \cdot 10^{-6}}{3 \times 10^{-6}} \sim 2 \times 10^{-3}. \tag{B.8}$$

Thus, the inertia is neglected.

Appendix C

An extended model taking into account with the effect by the existence of lower electrode

In this appendix, the equations of the single Quincke roller under an AC field [8] (Eqs. (2.23) and (2.24)) and the generalised versions Eqs. (C.9) and (C.10) are reconsidered if the effect by the existence of lower electrode is taken into account.

The DC case Only the effect from the lower electrode is incorporated as the first mirror image of $\boldsymbol{P}$ to the lower equipotential surface. The reason is that the disturbance from the upper electrode $\propto r^{-3}$ and sufficiently small, when the channel width is five times of particle's diameter. The image dipole $\boldsymbol{P}^{\star}$ is usually defined as

$$\boldsymbol{P}^{\star} = P_z \hat{\boldsymbol{e}_z} - \boldsymbol{P}_{\parallel}. \tag{C.1}$$

The unperturbed solution (the solution of Eqs. (2.23) and (2.24)) is $\boldsymbol{P}^{(0)}$, which makes its image dipole:

$$\boldsymbol{P}^{(0)\star} = P_z^{(0)} \hat{\boldsymbol{e}_z} - \boldsymbol{P}_{\parallel}^{(0)}. \tag{C.2}$$

The image dipole varies the electric field from $\boldsymbol{E}_0$ to $\boldsymbol{E}_0 + \delta\boldsymbol{E}^{\star}$, where

$$\delta\boldsymbol{E}^{\star} = -\nabla \left(\frac{\boldsymbol{P}^{(0)\star} \cdot \boldsymbol{r}}{4\pi\epsilon_0 r^3} \right) |_{\boldsymbol{r}=a\hat{\boldsymbol{e}_z}} \tag{C.3}$$

$$= \frac{1}{4\pi\epsilon_0 a^3} (\boldsymbol{P}_{\parallel}^{(0)}, 2P_z^{(0)}) \tag{C.4}$$

If the unperturbed solution $\boldsymbol{P}^{(0)}$ is assumed to be the steady solutions Eqs. (2.23) and (2.24) in the DC case, the transformation

$$\boldsymbol{E}_0 \longrightarrow \boldsymbol{E}_0 + \delta\boldsymbol{E}^{\star} \tag{C.5}$$

is just a shift of the constant value. Thus, Eqs. (2.23) and (2.24) are still valid in this DC case, which means that the particle moves with constant speed in steady states.

The AC case In DC case, the effect of the electrode can appear as the constant shift of the electric field. However, in the AC case, it can change the form of equations as follows. Let us start with Eq. (2.21).

The electric field disturbance $\delta \boldsymbol{E}^\star$ becomes time-dependent. The time-dependent unperturbed solution $\boldsymbol{P}^{(0)}(t)$ is displaced at $z = -a$ as a image polarisation to the lower electrode. In Eq. (2.21),

$$\begin{aligned} \boldsymbol{E}_0 &\longrightarrow \boldsymbol{E}_0 \cos\omega t + \delta \boldsymbol{E}^\star(t) && \text{(C.6)} \\ &= \left(\delta \boldsymbol{E}^\star_\parallel(t), E_0 \cos\omega t + \delta E^\star_z(t)\right) && \text{(C.7)} \\ &= \left(\frac{1}{4\pi\epsilon_0 a^3}\boldsymbol{P}^{(0)}_\parallel(t), E_0 \cos\omega t + \frac{1}{2\pi\epsilon_0 a^3} P^{(0)}_z(t)\right) && \text{(C.8)} \end{aligned}$$

where $\boldsymbol{P}^{(0)}(t)$ means the unperturbed solution.

Decompose Eq. (2.21) into z and parallel component with the notion in Eq. (C.7):

$$\begin{aligned} &\frac{\mathrm{d}P_z}{\mathrm{d}t} + \frac{1}{\tau_{\mathrm{MW}}} P_z \\ &= -\frac{2\pi\epsilon a^3}{\tau_{\mathrm{MW}}}(E_0 \cos\omega t + \delta E^\star_z(t)) \\ &+\mu_r \frac{\epsilon_l}{\epsilon_0}\Bigg[(P_\parallel^2 + P_z^2)(E_0 \cos\omega t + \delta E^\star_z(t)) - \left\{(E_0 \cos\omega t + \delta E^\star_z(t))P_z + \delta E^\star_\parallel P_\parallel\right\} P_z \\ &-4\pi\epsilon_0 a^3 \chi^\infty \left\{(E_0 \cos\omega t + \delta E^\star_z(t))P_z + \delta E^\star_\parallel P_\parallel\right\}(E_0 \cos\omega t + \delta E^\star_z(t)) \\ &+4\pi\epsilon_0 a^3 \chi^\infty \left\{(E_0 \cos\omega t + \delta E^\star_z(t))^2 + (\delta E^\star_\parallel)^2\right\} P_z\Bigg] \end{aligned} \tag{C.9}$$

$$\begin{aligned} &\frac{\mathrm{d}P_\parallel}{\mathrm{d}t} + \frac{1}{\tau_{\mathrm{MW}}} P_\parallel \\ &= -\frac{2\pi\epsilon a^3}{\tau_{\mathrm{MW}}}\delta E^\star_\parallel(t) \\ &+\mu_r \frac{\epsilon_l}{\epsilon_0}\Bigg[(P_\parallel^2 + P_z^2)\delta E^\star_\parallel(t) - \left\{(E_0 \cos\omega t + \delta E^\star_z(t))P_z + \delta E^\star_\parallel P_\parallel\right\} P_\parallel \\ &-4\pi\epsilon_0 a^3 \chi^\infty \left\{(E_0 \cos\omega t + \delta E^\star_z(t))P_z + \delta E^\star_\parallel P_\parallel\right\}\delta E^\star_\parallel(t) \\ &+4\pi\epsilon_0 a^3 \chi^\infty \left\{(E_0 \cos\omega t + \delta E^\star_z(t))^2 + (\delta E^\star_\parallel)^2\right\} P_\parallel\Bigg] \end{aligned} \tag{C.10}$$

Here, decompose the polarisations into the instantaneous part and the surface part by

$$\begin{aligned} P_\parallel(t) &= P^\sigma_\parallel(t) && \text{(C.11)} \\ P_z(t) &= P^\epsilon_z(t) + P^\sigma_z(t) && \text{(C.12)} \end{aligned}$$

$P^\epsilon_z(t)$ is determined by the electric field the particle feels at time t instantaneously (dielectric polarisation):

$$P^\epsilon_z(t) = 4\pi\epsilon_0 a^3 \chi^\infty (E_0 \cos\omega t + \delta E^\star_z(t)) \tag{C.13}$$

$$P_{\parallel}^{\epsilon}(t) = 4\pi\epsilon_0 a^3 \chi^{\infty} \delta E_{\parallel}^{\star}(t) \tag{C.14}$$

Then,

$$\begin{aligned}
&\frac{\mathrm{d}P_z^{\sigma}}{\mathrm{d}t} + \frac{1}{\tau_{\mathrm{MW}}} P_z^{\sigma} + \frac{\mathrm{d}P_z^{\epsilon}}{\mathrm{d}t} + \frac{1}{\tau_{\mathrm{MW}}} P_z^{\epsilon} \\
&= -\frac{2\pi\epsilon a^3}{\tau_{\mathrm{MW}}} (E_0 \cos\omega t + \delta E_z^{\star}(t)) \\
&+\mu_r \frac{\epsilon_l}{\epsilon_0} \Bigg[(P_{\parallel}^{\sigma 2} + (P_z^{\sigma} + P_z^{\epsilon})^2)(E_0 \cos\omega t + \delta E_z^{\star}(t)) \\
&\quad - \left\{ (E_0 \cos\omega t + \delta E_z^{\star}(t))(P_z^{\sigma} + P_z^{\epsilon}) + \delta E_{\parallel}^{\star} P_{\parallel}^{\sigma} \right\} (P_z^{\sigma} + P_z^{\epsilon}) \\
&\quad -4\pi\epsilon_0 a^3 \chi^{\infty} \left\{ (E_0 \cos\omega t + \delta E_z^{\star}(t))(P_z^{\sigma} + P_z^{\epsilon}) + \delta E_{\parallel}^{\star} P_{\parallel}^{\sigma} \right\} (E_0 \cos\omega t + \delta E_z^{\star}(t)) \\
&\quad +4\pi\epsilon_0 a^3 \chi^{\infty} \left\{ (E_0 \cos\omega t + \delta E_z^{\star}(t))^2 + (\delta E_{\parallel}^{\star})^2 \right\} (P_z^{\sigma} + P_z^{\epsilon}) \Bigg]
\end{aligned} \tag{C.15}$$

$$\begin{aligned}
&\frac{\mathrm{d}P_{\parallel}^{\sigma}}{\mathrm{d}t} + \frac{1}{\tau_{\mathrm{MW}}} P_{\parallel}^{\sigma} \\
&= -\frac{2\pi\epsilon a^3}{\tau_{\mathrm{MW}}} \delta E_{\parallel}^{\star}(t) \\
&+\mu_r \frac{\epsilon_l}{\epsilon_0} \Bigg[(P_{\parallel}^{\sigma 2} + (P_z^{\sigma} + P_z^{\epsilon})^2) \delta E_{\parallel}^{\star}(t) - \left\{ (E_0 \cos\omega t + \delta E_z^{\star}(t))(P_z^{\sigma} + P_z^{\epsilon}) + \delta E_{\parallel}^{\star} P_{\parallel}^{\sigma} \right\} P_{\parallel}^{\sigma} \\
&\quad -4\pi\epsilon_0 a^3 \chi^{\infty} \left\{ (E_0 \cos\omega t + \delta E_z^{\star}(t))(P_z^{\sigma} + P_z^{\epsilon}) + \delta E_{\parallel}^{\star} P_{\parallel}^{\sigma} \right\} \delta E_{\parallel}^{\star}(t) \\
&\quad +4\pi\epsilon_0 a^3 \chi^{\infty} \left\{ (E_0 \cos\omega t + \delta E_z^{\star}(t))^2 + (\delta E_{\parallel}^{\star})^2 \right\} P_{\parallel}^{\sigma} \Bigg]
\end{aligned} \tag{C.16}$$

For unperturbed solution,

$$P_{\parallel}^{(0)}(t) = P_{\parallel}^{(0)\sigma}(t) \tag{C.17}$$

$$P_z^{(0)}(t) = P_z^{(0)\,\epsilon}(t) + P_z^{(0)\,\sigma}(t) \tag{C.18}$$

$$= 4\pi\epsilon_0 a^3 \chi^{\infty} E_0 \cos\omega t + P_z^{(0)\,\sigma}(t) \tag{C.19}$$

hold.

Convert to dimensionless values by

$$A = \frac{\mu_r \varepsilon_l E_0^2 a^3}{D_\theta} \tag{C.20}$$

$$\tau_{\tilde{\mathrm{MW}}} = \tau_{\mathrm{MW}} D_\theta \tag{C.21}$$

$$\tilde{t} = D_\theta t \tag{C.22}$$

$$\tilde{P} = \frac{P}{\varepsilon_0 E_0 a^3} \tag{C.23}$$

$$\delta\tilde{E}^{\star} = \delta E^{\star}/E_0, \tag{C.24}$$

where the values with tilde are dimensionless. Therefore, nondimensionalised equations are following (For brevity, tilda is omitted.):

The equation of polarisation solved perturbatively

$$\begin{aligned}
&\frac{\mathrm{d}P_z^\sigma}{\mathrm{d}t} + \frac{1}{\tau_{\mathrm{MW}}} P_z^\sigma + 4\pi\chi^\infty \frac{\mathrm{d}(\cos\omega t + \delta E_z^\star(t))}{\mathrm{d}t} \\
&+ \frac{4\pi(\chi^\infty + 1/2)}{\tau_{\mathrm{MW}}} (\cos\omega t + \delta E_z^\star(t)) \\
= \;& A\left[P_\parallel^{\sigma\,2} (\cos\omega t + \delta E_z^\star(t)) - \delta E_\parallel^\star P_\parallel^\sigma P_z^\sigma \right] \qquad \text{(C.25)}
\end{aligned}$$

$$\begin{aligned}
&\frac{\mathrm{d}P_\parallel^\sigma}{\mathrm{d}t} + \frac{1}{\tau_{\mathrm{MW}}} P_\parallel^\sigma + 4\pi\chi^\infty \frac{\mathrm{d}(\delta E_\parallel^\star(t))}{\mathrm{d}t} + \frac{4\pi(\chi^\infty + 1/2)}{\tau_{\mathrm{MW}}} \delta E_\parallel^\star(t) \\
&= A\left[P_\parallel^{\sigma\,2} \delta E_\parallel^\star(t) - (\cos\omega t + \delta E_z^\star(t)) P_z^\sigma P_\parallel^\sigma \right] \qquad \text{(C.26)}
\end{aligned}$$

For $\delta \boldsymbol{E}^\star(t)$, Eq. (C.8) is substituted with the unperturbed solution which can be numerically calculated through these equations Eqs. (C.25) and (C.26) with $\delta \boldsymbol{E}^\star(t) = 0$ and Eqs. (C.13) and (C.14) or simply through Eqs. (C.9) and (C.10).

The translation velocity is modified from Eq. (2.38) as

$$\begin{aligned}
\boldsymbol{v}(t) &= \frac{\epsilon_l}{\epsilon_0} a \tilde{\mu_t} \boldsymbol{\Lambda} \boldsymbol{P}(t) \times \boldsymbol{E}(t) \qquad \text{(C.27)} \\
&= -\frac{\epsilon_l}{\epsilon_0} a \tilde{\mu_t} \left\{ (E_0 \cos\omega t + \delta E_z^\star(t)) P_\parallel(t) - P_z(t) \delta E_\parallel^\star(t) \right\}, \qquad \text{(C.28)}
\end{aligned}$$

which is determined by both $P_\parallel$ and P_z.

Bibliography

[1] Tamás Vicsek, András Czirók, Eshel Ben-Jacob, Cohen, and Shochet. Novel Type of Phase Transition in a System of Self-Driven Particles. *Physical Review Letters*, 75(6):729–732, 1995.

[2] Guillaume Grégoire and Hugues Chaté. Onset of collective and cohesive motion. *Phys. Rev. Lett.*, 92:025702, Jan 2004.

[3] John Toner and Yuhai Tu. Flocks, herds, and schools: A quantitative theory of flocking. *Physical Review E*, 58(4):4828–4858, 1998.

[4] Hugues Chaté, Francesco Ginelli, and Raúl Montagne. Simple Model for Active Nematics: Quasi-Long-Range Order and Giant Fluctuations. *Physical Review Letters*, 96(18):180602, 2006.

[5] Xia-qing Shi and Yu-qiang Ma. Topological structure dynamics revealing collective evolution in active nematics. *Nature Communications*, 4(1):3013, 2013.

[6] Francesco Ginelli, Fernando Peruani, Markus Bär, and Hugues Chaté. Large-scale collective properties of self-propelled rods. *Phys. Rev. Lett.*, 104:184502, May 2010.

[7] Julien Deseigne, Olivier Dauchot, and Hugues Chaté. Collective motion of vibrated polar disks. *Physical Review Letters*, 105(9):1–4, 2010.

[8] Antoine Bricard, Jean-Baptiste Caussin, Nicolas Desreumaux, Olivier Dauchot, and Denis Bartolo. Emergence of macroscopic directed motion in populations of motile colloids. *Nature*, 503(7474):95–8, 2013.

[9] Volker Schaller, Christoph Weber, Christine Semmrich, Erwin Frey, and Andreas R. Bausch. Polar patterns of driven filaments. *Nature*, 467(7311):73–77, 2010.

[10] Daiki Nishiguchi, Ken H. Nagai, Hugues Chaté, and Masaki Sano. Long-range nematic order and anomalous fluctuations in suspensions of swimming filamentous bacteria. *Phys. Rev. E*, 95:020601, Feb 2017.

[11] Yutaka Sumino, Ken H. Nagai, Yuji Shitaka, Dan Tanaka, Kenichi Yoshikawa, Hugues Chaté, and Kazuhiro Oiwa. Large-scale vortex lattice emerging from collectively moving microtubules. *Nature*, 483(7390):448–452, 2012.

[12] Kolbjørn Tunstrøm, Yael Katz, Christos C. Ioannou, Cristián Huepe, Matthew J. Lutz, and Iain D. Couzin. Collective States, Multistability and Transitional Behavior in Schooling Fish. *PLoS Computational Biology*, 9(2):e1002915, 2013.

[13] Hugo Wioland, Francis G. Woodhouse, Jörn Dunkel, John O. Kessler, and Raymond E. Goldstein. Confinement Stabilizes a Bacterial Suspension into a Spiral Vortex. *Physical Review Letters*, 110(26):268102, 2013.

[14] Isaac Theurkauff, Cécile Cottin-Bizonne, Jeremie Palacci, Christophe Ybert, and Lydéric Bocquet. Dynamic clustering in active colloidal suspensions with chemical signaling. *Physical Review Letters*, 108(June):1–5, 2012.

[15] Meso-scale turbulence in living fluids. *Proceedings of the National Academy of Sciences*, 109(36):14308–14313, 2012.

[16] Daiki Nishiguchi and Masaki Sano. Mesoscopic turbulence and local order in Janus particles self-propelling under an ac electric field. *Physical Review E*, 92(5):052309, nov 2015.

[17] G. E. Uhlenbeck and L. S. Ornstein. On the theory of the brownian motion. *Phys. Rev.*, 36:823–841, Sep 1930.

[18] Clemens Bechinger, Roberto Di Leonardo, Hartmut Löwen, Charles Reichhardt, Giorgio Volpe, and Giovanni Volpe. Active particles in complex and crowded environments. *Rev. Mod. Phys.*, 88:045006, Nov 2016.

[19] Jonathan R. Howse, Richard A. L. Jones, Anthony J. Ryan, Tim Gough, Reza Vafabakhsh, and Ramin Golestanian. Self-motile colloidal particles: From directed propulsion to random walk. *Phys. Rev. Lett.*, 99:048102, Jul 2007.

[20] Xu Zheng, Borge ten Hagen, Andreas Kaiser, Meiling Wu, Haihang Cui, Zhanhua Silber-Li, and Hartmut Löwen. Non-gaussian statistics for the motion of self-propelled janus particles: Experiment versus theory. *Phys. Rev. E*, 88:032304, Sep 2013.

[21] R Großmann, F Peruani, and M Bär. Diffusion properties of active particles with directional reversal. *New Journal of Physics*, 18(4):043009, apr 2016.

[22] S Babel, B ten Hagen, and H Löwen. Swimming path statistics of an active brownian particle with time-dependent self-propulsion. *Journal of Statistical Mechanics: Theory and Experiment*, 2014(2):P02011, feb 2014.

[23] H. P. Zhang, A. Be'er, E.-L. Florin, and H. L. Swinney. Collective motion and density fluctuations in bacterial colonies. *Proceedings of the National Academy of Sciences*, 107(31):13626–13630, 2010.

[24] Howard C. Berg and Douglas A. Brown. Chemotaxis in escherichia coli analysed by three-dimensional tracking. *Nature*, 239(5374):500–504, 1972.

[25] Howard C. Berg. *E. coli in Motion*. Springer-Verlag, Heidelberg, Germany, 2004.

[26] Yilin Wu, A. Dale Kaiser, Yi Jiang, and Mark S. Alber. Periodic reversal of direction allows myxobacteria to swarm. *Proceedings of the National Academy of Sciences*, 106(4):1222–1227, 2009.

[27] Vijay Narayan, Sriram Ramaswamy, and Narayanan Menon. Long-lived giant number fluctuations in a swarming granular nematic. *Science*, 317(5834):105–108, 2007.

[28] Hiroyuki Ebata and Masaki Sano. Swimming droplets driven by a surface wave. *Scientific Reports*, 5(1):8546, 2015.

[29] Walter F. Paxton, Kevin C. Kistler, Christine C. Olmeda, Ayusman Sen, Sarah K. St. Angelo, Yanyan Cao, Thomas E. Mallouk, Paul E. Lammert, and Vincent H. Crespi. Catalytic nanomotors: Autonomous movement of striped nanorods. *Journal of the American Chemical Society*, 126(41):13424–13431, 10 2004.

[30] Yang Wang, Rose M. Hernandez, David J. Bartlett, Julia M. Bingham, Timothy R. Kline, Ayusman Sen, and Thomas E. Mallouk. Bipolar electrochemical mechanism for the propulsion of catalytic nanomotors in hydrogen peroxide solutions. *Langmuir*, 22(25):10451–10456, 2006.

[31] Jérémie Palacci, Cécile Cottin-Bizonne, Christophe Ybert, and Lydéric Bocquet. Sedimentation and effective temperature of active colloidal suspensions. *Phys. Rev. Lett.*, 105:088304, Aug 2010.

[32] F. Ginot, I. Theurkauff, F. Detcheverry, C. Ybert, and C. Cottin-Bizonne. Aggregation-fragmentation and individual dynamics of active clusters. *Nature Communications*, 9(1):696, 2018.

[33] Hong-Ren Jiang, Natsuhiko Yoshinaga, and Masaki Sano. Active motion of a janus particle by self-thermophoresis in a defocused laser beam. *Phys. Rev. Lett.*, 105:268302, Dec 2010.

[34] Jeremie Palacci, Stefano Sacanna, Asher Preska Steinberg, David J. Pine, and Paul M. Chaikin. Living crystals of light-activated colloidal surfers. *Science*, 339(6122):936–940, 2013.

[35] Juan Ruben Gomez-Solano, Sela Samin, Celia Lozano, Pablo Ruedas-Batuecas, René van Roij, and Clemens Bechinger. Tuning the motility and directionality of self-propelled colloids. *Scientific Reports*, 7(1):14891, 2017.

[36] Celia Lozano, Juan Ruben Gomez-Solano, and Clemens Bechinger. Run-and-tumble-like motion of active colloids in viscoelastic media. *New Journal of Physics*, 20(1):015008, jan 2018.

[37] Celia Lozano and Clemens Bechinger. Diffusing wave paradox of phototactic particles in traveling light pulses. *Nature Communications*, 10(1):2495, 2019.

[38] Daiki Nishiguchi, Junichiro Iwasawa, Hong-Ren Jiang, and Masaki Sano. Flagellar dynamics of chains of active janus particles fueled by an AC electric field. *New Journal of Physics*, 20(1):015002, jan 2018.

[39] Tomoyuki Mano, Jean-Baptiste Delfau, Junichiro Iwasawa, and Masaki Sano. Optimal run-and-tumble–based transportation of a janus particle with active steering. *Proceedings of the National Academy of Sciences*, 114(13):E2580–E2589, 2017.

[40] Colin D. Bain, Graham D. Burnett-Hall, and Richard R. Montgomerie. Rapid motion of liquid drops. *Nature*, 372(6505):414–415, 1994.

[41] Yutaka Sumino, Hiroyuki Kitahata, Kenichi Yoshikawa, Masaharu Nagayama, Shinichiro M. Nomura, Nobuyuki Magome, and Yoshihito Mori. Chemosensitive running droplet. *Phys. Rev. E*, 72:041603, Oct 2005.

[42] Hiroyuki Kitahata, Natsuhiko Yoshinaga, Ken H. Nagai, and Yutaka Sumino. Spontaneous motion of a droplet coupled with a chemical wave. *Phys. Rev. E*, 84:015101, Jul 2011.

[43] Shashi Thutupalli, Ralf Seemann, and Stephan Herminghaus. Swarming behavior of simple model squirmers. *New Journal of Physics*, 13(7):073021, jul 2011.

[44] Shinpei Tanaka, Yoshimi Sogabe, and Satoshi Nakata. Spontaneous change in trajectory patterns of a self-propelled oil droplet at the air-surfactant solution interface. *Phys. Rev. E*, 91:032406, Mar 2015.

[45] Takaki Yamamoto and Masaki Sano. Chirality-induced helical self-propulsion of cholesteric liquid crystal droplets. *Soft Matter*, 13:3328–3333, 2017.

[46] Mariko Suga, Saori Suda, Masatoshi Ichikawa, and Yasuyuki Kimura. Self-propelled motion switching in nematic liquid crystal droplets in aqueous surfactant solutions. *Phys. Rev. E*, 97:062703, Jun 2018.

[47] Antoine Bricard, Jean-Baptiste Caussin, Debasish Das, Charles Savoie, Vijayakumar Chikkadi, Kyohei Shitara, Oleksandr Chepizhko, Fernando Peruani, David Saintillan, and Denis Bartolo. Emergent vortices in populations of colloidal rollers. *Nature Communications*, 6(1):7470, 2015.

[48] F. Peters, L. Lobry, A. Khayari, and E. Lemaire. Size effect in quincke rotation: A numerical study. *The Journal of Chemical Physics*, 130(19):194905, 2009.

[49] Gerardo E. Pradillo, Hamid Karani, and Petia M. Vlahovska. Quincke rotor dynamics in confinement: rolling and hovering. *Soft Matter*, 15:6564–6570, 2019.

[50] Hamid Karani, Gerardo E. Pradillo, and Petia M. Vlahovska. Tuning the random walk of active colloids: From individual run-and-tumble to dynamic clustering. *Phys. Rev. Lett.*, 123:208002, Nov 2019.

[51] Mitsusuke Tarama and Takao Ohta. Oscillatory motions of an active deformable particle. *Phys. Rev. E*, 87:062912, Jun 2013.

[52] Tetsuya Hiraiwa, Kyohei Shitara, and Takao Ohta. Dynamics of a deformable self-propelled particle in three dimensions. *Soft Matter*, 7:3083–3086, 2011.

[53] Mitsusuke Tarama and Takao Ohta. Dynamics of a deformable self-propelled particle with internal rotational force. *Progress of Theoretical and Experimental Physics*, 2013(1), 01 2013. 013A01.

[54] Tong Gao and Zhaorui Li. Self-driven droplet powered by active nematics. *Phys. Rev. Lett.*, 119:108002, Sep 2017.

[55] R. Suzuki, H. R. Jiang, and M. Sano. Validity of fluctuation theorem on self-propelling particles. 2011.

[56] G. Quincke. Ueber rotationen im constanten electrischen felde. *Annu. Phys. Chem.*, 59:417–486, 1896.

[57] N. Pannacci, L. Lobry, and E. Lemaire. How insulating particles increase the conductivity of a suspension. *Physical Review Letters*, 99(9):2–5, 2007.

[58] T. B. Jones. Quincke rotation of spheres. *IEEE Transactions on Industry Applications*, IA-20(4):845–849, July 1984.

[59] E Lemaire and L Lobry. Chaotic behavior in electro-rotation. *Physica A: Statistical Mechanics and its Applications*, 314(1):663 – 671, 2002. Horizons in Complex Systems.

[60] Yu Dolinsky and T. Elperin. Dipole interaction of the Quincke rotating particles. *Physical Review E - Statistical, Nonlinear, and Soft Matter Physics*, 85(2):1–8, 2012.

[61] Debasish Das and David Saintillan. Electrohydrodynamic interaction of spherical particles under quincke rotation. *Phys. Rev. E*, 87:043014, Apr 2013.

[62] G. Liao, Ivan I. Smalyukh, J. R. Kelly, Oleg D. Lavrentovich, and Antal Jákli. Electrorotation of colloidal particles in liquid crystals. *Physical Review E*, 72(September):1–5, 2005.

[63] Stewartson K. O'Neill, M. On the slow motion of a sphere parallel to a nearby plane wall. *Journal of Fluid Mechanics*, 27(4):705–724, 1967.

[64] J. R. Blake and A. T. Chwang. Fundamental singularities of viscous flow. *Journal of Engineering Mathematics*, 8(1):23–29, Jan 1974.

[65] W. W. Hackborn. Asymmetric stokes flow between parallel planes due to a rotlet. *Journal of Fluid Mechanics*, 218:531–546, 1990.

[66] Shi Qing Lu, Bing Yue Zhang, Zhi Chao Zhang, Yan Shi, and Tian Hui Zhang. Pair aligning improved motility of quincke rollers. *Soft Matter*, 14:5092–5097, 2018.

[67] J R Melcher and G I Taylor. Electrohydrodynamics: A review of the role of interfacial shear stresses. *Annual Review of Fluid Mechanics*, 1(1):111–146, 1969.

[68] I. F. Sbalzarini and P. Koumoutsakos. Feature point tracking and trajectory analysis for video imaging in cell biology. *J. Struct. Biol.*, 151(2):182–195, 2005.